Pergamon

Progress in Surface Science, Vol. 52, No. 4, pp. 193–335, 1996
Copyright © 1996 Elsevier Science Ltd
Printed in Great Britain. All rights reserved.
0079-6816/96 $32.00

PII: S0079-6816(96)00008-1

QUANTITATIVE SURFACE ANALYSIS BY AUGER AND X-RAY PHOTOELECTRON SPECTROSCOPY

I. S. TILININ*, A. JABLONSKI* and W. S. M. WERNER**

*Institute of Physical Chemistry, Polish Academy of Sciences, ul. Kasprzaka 44/52, 01-224 Warsaw Poland
**Institute for Applied and Technical Physics, Vienna University of Technology, Wiedner Hauptstrasse, 8–10, Vienna A-1040, Austria

Abstract

Recent developments in quantitative surface analysis by Auger (AES) and x-ray photoelectron (XPS) spectroscopies are reviewed and problems relating to a more accurate quantitative interpretation of AES/XPS experimental data are discussed. Special attention is paid to consideration of elementary physical processes involved and influence of multiple scattering effects on signal line intensities. In particular, the major features of core-shell ionization by electron impact, Auger transitions and photoionization are considered qualitatively and rigorous approaches used to calculate the respective transition probabilities are analysed. It is shown that, in amorphous and polycrystalline targets, incoherent scattering of primary and signal Auger and photoelectrons can be described by solving analytically a kinetic equation with appropriate boundary conditions. The analytical results for the angular and energy distribution, the mean escape depth, and the escape probability as a function of depth of origin of signal electrons as well as that for the backscattering factor in AES are in good agreement with the corresponding Mote Carlo simulation data. Methods for inelastic background subtraction, surface composition determination and depth-profile reconstructions by angle-resolved AES/XPS are discussed. Examples of novel techniques based on x-ray induced photoemission are considered.

Contents

1. Introduction

2. Physical Background. Elementary Processes

A. Inner-shell ionization by electron impact

B. Auger emission

C. Photoionization

D. Elastic scattering of medium energy electrons by atoms. Elastic scattering and transport cross sections

E. Inelastic intaraction. Inelastic mean free path

3. Multiple Scattering of Signal Electrons in Solids

A. Medium energy electron-solid interaction

B. Transport equation approach

C. Monte Carlo simulation method

D. Basic secondary emission characteristics in AES/XPS

E. Influence of crystallinity on the Auger and photoelectron line intensity

4. Backscattering of Primary Electrons

A. Total reflection coefficient

B. Electron backscattering from targets of complex chemical composition

C. Backscattering factor in AES

5. Application of AES/XPS to Surface Analysis

A. Methods of inelastic background removal

B. Elemental composition determination

C. Depth profiling

D. Synchrotron radiation in XPS analysis

E. Auger photoelectron coincidence spectroscopy

6. Conclusion

Acknowledgements

References

Acronyms

AED	Auger electron diffraction
AES	Auger electron spectroscopy
AL	attenuation length
APECS	Auger photoelectron coincidence spectroscopy
ARAES	angle-resolved Auger electron spectroscopy
ARXPS	angle-resolved x-ray photoelectron spectroscopy
CMA	cylindrical mirror analyser
CWBA	Coulomb-wave Born approximation
DDF	depth distribution function
DWBA	distorted-wave Born approximation
EPMA	electron probe microanalysis
FWHM	full width at half maximum
IMFP	inelastic mean free path
LEED	low-energy electron diffraction
MAXIMUM	multiple-application x-ray imaging undulator microscope
MC	Monte Carlo
PWBA	plane-wave Born approximation
QUEST	quantitation of electron spectroscopy techniques
REELS	reflection electron energy-loss spectroscopy
SEXAFS	surface extended x-ray absorption fine structure
SIMS	secondary-ion mass spectroscopy
SLA	straight-line approximation
SPEM	scanning photoelectron microscope
TA	transport approximation
XPS	x-ray photoelectron spectroscopy
XSW	x-ray standing wave

1. Introduction

Among surface sensitive techniques involving electron spectroscopies, Auger and x-ray photoelectron spectroscopies have become the most widely used during last decades. This is explained to a great extent by both their universal applicability and seemingly simple interpretation of experimental data obtained by AES/XPS. Although the first feature is by no means true the second one relates only to elementary information about a specimen studied. In recent years it has been realized that apart from traditional elemental composition determination and overlayer thickness assessments, Auger and photoelectron spectra carry a good deal of other information characterizing a near surface region of solids. In particular, angular distribution of signal electrons escaping from a crystalline target without a considerable energy loss can be used for determination of not only adsorbate site symmetries and vertical positions, but also substrate interlayer relaxations [1]. Holographic analysis of Auger and photoelectron diffraction patterns is supposed to yield three dimensional atomic images relative to the emitting atom [1–4]. Spin-resolved XPS may become a basic tool for studying local magnetic order while excitation of core-shell photoelectron by polarized x-rays at different orientations of polarization vector with respect to a sample position can be used to extract complementary structural information [5]. Auger photoelectron coincidence spectroscopy has been shown to provide a powerful means for effective decomposition of complicated energy spectra in the vicinity of a characteristic peak [6,7].

This list of prospective applications and those being already in use can be extended. Meanwhile, it is becoming increasingly clear that novel areas of applications of and further improvement in accuracy of quantitative information obtained by AES/XPS stipulate a more sophisticated experimental equipment as well as theoretical description of phenomena involved, so that a gap between a practical user and a "front-runner", if such a term is appropriate, seems to be widening. Various aspects of AES/XPS analysis comprise instrumentation, specific conditions of a given experiment and a theoretical background. A number of excellent reviews and monographs have appeared in literature [1,8–18]. However a broad range of disciplines underlying the foundations of AES/XPS makes it difficult to embrace all the essential issues in one, even sufficiently large, paper or book. The major purpose of this article is to review recent developments in quantitative description of signal Auger and photoelectron spectra. Besides that, a considerable attention is paid to qualitative considerations of basic elementary processes such as core-shell ionization by photons and electron impact, Auger transitions, elastic and inelastic scattering of medium energy electrons. Most recent examples of AES/XPS applications and practical methods to process

experimental data are discussed.

The basic issues of the quantitative analysis by AES/XPS can be seen from the yield equation relating the signal intensity ΔI collected in a narrow solid angle $\Delta\Omega$ and properties of a sample studied. This equation reads

$$\Delta I = TDAY(\Omega)\Delta\Omega \tag{1.1}$$

where T and D are the analyser transmission function and the detector efficiency, correspondingly, A is the analysed area and $Y(\Omega)$ is the differential electron yield, describing the number of signal electrons (*i.e.* those that do not lose their kinetic energy) escaping from a unit area of the target per unit time in the direction specified by a unit vector Ω.

Assuming the transmission function and the detector efficiency to be dimensionless quantities, the signal intensity is proportional to the number of signal electrons entering a detector window per unit time. Usually, the sample properties are believed to be uncorrelated with the instrumental factors T and D. Therefore, all information about the sample is contained in the differential yield $Y(\Omega)$ which is a central quantity to be determined in quantitative analysis. The distribution $Y(\Omega)$ is generally a complicated function of the elemental composition, crystalline structure and in-depth profile of the target, as well as major physical processes involved in signal electron emission. Consider, for instance, the simplest case of a homogeneous amorphous one-element sample. Then, without losing generality, the function Y may be split into the product

$$Y(\Omega) = \mu M F \sigma_{ex} f(\Omega)\lambda. \tag{1.2}$$

Here μ is the cosine of the polar emission angle counted from the surface normal, M is the atomic bulk density, F is the flux of incident particles (electrons in AES or photons in XPS), σ_{ex} is the excitation cross section, $f(\Omega)$ is the normalized angular distribution. The quantity λ is introduced from simple dimension considerations and is termed below as the effective escape depth of signal electrons of a specific energy E. The effective escape depth λ is used here to characterize an analysed volume and should not be confused with the mean escape depth which is a strictly defined quantity [19]. In the case of XPS, the quantity σ_{ex} is equal to the total photoelectric cross section, $\sigma_{ex} = \sigma_{ph}$. If signal electrons are excited by electron impact (AES) the excitation cross section is defined as a product of the ionization cross section $\sigma_{ion}(E_p)$, the Auger electron yield a and the backscattering factor B so that we have $\sigma_{ex} = aB\sigma_{ion}(E_p)$ where E_p is the energy of bombarding electrons. Note that (1.2) is obtained assuming negligible role of x-ray reflection and attenuation in the analysed volume. The latter assumptions are justified due to the condition

$$\lambda_i \ll \Lambda_a \ll \Lambda_{tr} \tag{1.3}$$

being well fulfilled. In expression (1.3) Λ_a and Λ_{tr} are the absorption and the transport mean free paths of photons, while λ_i is the inelastic mean free path of electrons. In addition, refraction of x-rays is usually also disregarded as this phenomenon is significant only for grazing incidence of photons and, therefore, is of little importance for practical XPS analysis.

The main parameter affecting the surface sensitivity of AES/XPS is the effective escape depth λ. This quantity is frequently supposed to be independent of the emission direction Ω and put equal to the inelastic mean free path, $\lambda \sim \lambda_i$. In effect, the escape depth depends noticeably on both elastic and inelastic interactions, and also on the final emission direction of electrons from a target.

From this brief outline, it follows that quantification of experimental data in AES/XPS implies knowledge ofthe main features of elementary processes and multiple scattering of primary and secondary electrons in matter. This prompted the following structure of the paper. Various approaches to calculate probabilities of elementary interactions and the latest developments in describing multiple scattering of Auger and photoelectrons are reviewed in Section 2 and Section 3, respectively. Section 4 is devoted to backscattering of primary electrons and determination of the backscattering factor. Examples of the quantitative analysis by AES/XPS are presented in Section 5.

2. Physical Background. Elementary Processes

A. Inner-shell ionization by electron impact

In Auger electron spectroscopy, signal Auger electrons appear as a result of a rearrangement of vacancies in atomic shells, following ionization of an inner shell by a primary electron. Thus, the intensity of the Auger electron line is a function of the inner-shell ionization cross section. Knowledge of inner-shell ionization cross section values is also important in electron microprobe analysis (EPMA) and electron energy loss spectroscopy. Latest developments in this field were reviewed in several papers by Powell [20–22] with a major emphasis on reliable formulas for cross sections, available at present. Unfortunately the problem of core-shell ionization is far from being solved. The 15-20 % discrepancies between the best analytical fits and experimental data is rather a rule than exception. This necessitates further studies and discussion of physical phenomena accompanying an ionization event.

The tightly bound atomic elelctrons of inner-shells are well localized in space. Their wave

functions and energy levels in a solid as a rule differ only slightly from those of an isolated atom. In this connection, considering major features of ionization of an inner shell for isolated atoms is a good starting point before going to implications of solid state effects. Many efforts have been applied to calculation of ionization cross sections by electron impact [23–35]. However, evaluation of the core-shell ionization probability from first principles even in the case of isolated atoms represents a difficult task. At present, there are two limiting cases where physically based analytical expressions for the ionization cross section can be obtained. Those cases pertain to the high energy regime ($E \gg E_{nl}$) and the near threshold ionization ($E - E_{nl} \ll E_{nl}$), where E and E_{nl} are the incoming electron kinetic energy and the binding energy of the nl atomic shell, respectively.

If the electron kinetic energy E is large compared with the binding energy E_{nl} one can apply the Born approximation [36] to find the ionization cross section. The energy transfer ε from the primary to the atomic electron, defined from the energy conservation law

$$\varepsilon = (\hbar/2m)(k^2 - k'^2), \tag{2.1}$$

is believed to be small compared with the quantity E ($\varepsilon \ll E$). In formula (2.1) $\mathbf{k}$ and $\mathbf{k}'$ are the initial and the final momenta of the incident electron in units of the Planck constant $\hbar$. From (2.1) and the assumption $\varepsilon \ll E$, it follows that the absolute value of the electron momentum k changes insignificantly during a collision event and the energy transfer may be written as $\varepsilon \sim \hbar v(k - k')$. The criterion of validity of the Born approximation can be also presented in the form [33]

$$2\pi Z_{eff} e^2/\hbar \ll v \tag{2.2}$$

where Z_{eff} is the effective charge of the field seen by the bound atomic electron and v is the velocity of the primary electron. The quantity $Z_{eff}e^2/\hbar$ represents the effective velocity of a bound atomic electron. Thus, criterion (2.2) means physically that the incident electron velocity has to be large compared with the typical velocity of the atomic electron.

The double differential ionization cross section $d\sigma_{ion}$ is proportional to the transition matrix element squared $\mid M_{if} \mid^2$ [36]

$$d\sigma_{ion} \sim (4k'/kq^4) Z_{nl} \mid M_{if} \mid^2 d\Omega_1 d\Omega_2 \kappa^2 d\kappa \tag{2.3}$$

Here Z_{nl} is the number of electrons in the nl shell, $q = (k^2 + k'^2 - 2kk' \cos\vartheta)^{1/2}$ is the momentum transfer, ϑ is the polar scattering angle of the incident electron, κ is the momentum of the ejected electron, while $d\Omega_1$ and $d\Omega_2$ are elementary solid angles the scattered (1) and the ejected (2)

electrons move in. Taking into account the explicit expression for the transition matrix element

$$M_{if} = -e^2 \int \psi_f^*(\mathbf{r})\psi^*(\mathbf{r}_a) \mid \mathbf{r} - \mathbf{r}_a \mid^{-1} \psi_i(\mathbf{r})\phi_i(\mathbf{r}_a) d\mathbf{r} d\mathbf{r}_a \tag{2.4}$$

the problem of the ionization cross section evaluation is reduced to finding the wave functions of the incident ($\psi(\mathbf{r})$) and bound ($\phi(\mathbf{r}_a)$) electrons in the initial (subscript "i") and the final ("f") states. The asterisks in the integrand denote complex conjugate values.

The next step is a proper choice of the wave functions. In the simplest plane-wave Born approximation (PWBA) the wave functions of the incident and scattered electrons are put equal to the exponential $\Psi_{i,f}(\mathbf{r}) \sim \exp(-i\mathbf{kr})$. Physically it means that the incoming electron motion is assumed to be rectilinear and undisturbed by the electric fields of the nucleus and other atomic electrons. Substitution of the exponential wave functions for the incident electron into (2.4) makes possible to perform integration over the incident electron variable $\mathbf{r}$ analytically. The resulting integral over the coordinate $\mathbf{r}_a$ of the atomic electron contains in the integrand the product of the wave functions ϕ_i and ϕ_f and $exp(-i\mathbf{qr}_a)$. Observing that the major contribution to the latter integral is supplied by the region of integration $r \sim a_{nl}$, where a_{nl} is the effective radius of the nl shell and that the ionization probability is determined mainly by small-momentum-transfer events ($qa_{nl} \ll 1$) (*cf.* (2.3)) the matrix element M_{if} can be found in the dipole approximation by setting $\exp(-i\mathbf{qr}_a) \sim 1 - i\mathbf{qr}_a$. Coming back to expression (2.3) and integrating over all the ejected electron momenta one obtains the differential ionization cross section with respect to the momentum transfer q

$$d\sigma_{ion} \sim 2\pi(e/\hbar v)^2 \mid (z_a)_{if} \mid^2 dq/q \tag{2.5}$$

Here z_a is the coordinate of the radius vector $\mathbf{r}_a$ along the momentum transfer $\mathbf{q}$. Performing summation over all the final states, including excitation of discrete levels, and integrating the resulting equation over the momentum transfer from the minimum value $q_{min} = E_{nl}/\hbar v$ to the maximum value $q_{max} = 2mv/\hbar$ we obtain from (2.5) the renowned formula of Bethe [23]

$$\sigma_{nl} = (\pi e^4/E)(Z_{nl}b_{nl}/E_{nl})\ln(c_{nl}E/E_{nl}), \tag{2.6}$$

where b_{nl} is the parameter proportional to the average oscillator strength, while the quantity c_{nl} (in the Bethe approach $c_{nl} = 4$) is introduced to account for a more general expression for the maximum momentum transfer $q_{max} = c_{nl}mv/2\hbar$. At this stage it should be stressed that, strictly speaking, expression (2.6) has a limited applicability to the energy range relevant to practical AES analysis. Indeed, bearing in mind criterion (2.2) and assuming that it is fulfilled for the electron velocity being, at least, by the order of magnitude higher than the product $2\pi Z_{eff}e^2/\hbar$ we arrive

at the conclusion that for ionization of core shells of relatively light elements (C – Al) the energy E would be larger than several ten keV. For heavy targets, such as gold, condition (2.2) would even mean that the primary electron energy falls into the relativistic region. This is far away on the energy scale from the conventional energy interval of AES ranging from several hundred to several thousand eV. The aforesaid estimate is in full accordance with the observation of Powell [22]. He found that the Fano plots (the product $\sigma_{nl}E$ versus $\ln E$) showed the asymptotic Bethe dependence with a slope directly related to photoabsorption data, beginning from the energy $E \geq (50 - 200)E_{nl}$, depending on the material.

The main advantage of the Bethe formula is that (2.6) is very convenient to use in practice. Therefore, numerous attempts have been made to adjust expression (2.6) to the energy region of practical importance in AES. This can be done by inserting empirical values for the parameters b_{nl} and c_{nl} [20,37–39] since the Fano plot tends to be also linear for the overvoltage $U_{nl} = E/E_{nl}$ ranging from 4 to about 20 [22]. The empirical expressions for the ionization cross section, obtained in this way, should be used cautiously as there is a risk of the potential conflict with other data [22]. Uncertainties in values of the parameters b_{nl} and c_{nl}, when applying the Bethe equation to the intermediate overvoltage range (so-called region 1, according to the terminology of Powell [22]) stem from the basic deficiencies of the perturbation theory approach: neglect of exchange between the incoming and atomic electrons, the assumption of the small energy transfer and disregard for scattering of the projectile in the screened Coulomb field of an atomic nucleus. Due to the same reason the linear response theory of inelastic scattering of electrons in solids [40–42] can be hardly expected to provide satisfactory results in this energy region.

In recent years much attention has been paid to improvement of the Born approximation results by accounting for elastic scattering of incident and outgoing electrons in the atomic field [33–35,43]. These studies are prompted in a large extent by a possibility of direct experimental measurements of the triple differential cross sections for core-shell ionization. In particular, Lahmam-Bennami et.al. [44] and Stefani et.al. [45] report on the ionization of Ar 2p shell by 8 keV electrons. Avaldi et.al. [46] measured the differential cross section for the ionization of C 1s orbital in the molecule C_2H_2 at the primary-electron energy of about 1.9 keV. The angular distribution of ejected electrons, obtained experimentally, was found to be in a considerable disagreement with the first-order Born approximation model [46].

In the distorted-wave Born approximation (DWBA) the wave functions of the free electrons are approximated by nonrelativistic Coulomb waves (Coulomb-wave Born approximation, CWBA) or obtained from a numerical solution of the Dirac equation with an effective atomic potential [35].

The DWBA results [34,43] compare well with the experimental data for the inner-shell ionization of neon and argon in the nonrelativistic energy region. However, no analytical expression for the total ionization cross section, derived in the DWBA, has been proposed so far.

Some comments are to be made on the behaviour of the ionization probability in the vicinity of the threshold. Wannier [47] suggested that slow electrons depart most probably from a nucleus along a straight line after an ionization event. The nucleus was assumed to be approximately in the middle of the distance separating the electrons. The key idea of Wannier's approach is that ionization can be attained only if the aforesaid configuration of electric charges remain until their potential energy drops below the residual kinetic energy. So the motion of the electron pair occurs in a narrow cone along the straight line. Because of slow variation of the potential energy with distance the motion of departing electrons can be described classically [48]. Solution of classical equations of motion for $E - E_{nl} \ll E_{nl}$ yields the energy dependence of the cross section $\sigma_{nl} \sim (E - E_{nl})^{\alpha}$, with the exponent $\alpha = 1.127$ [47]. Experimental studies performed later for the K-shells of Ar, Ti, Ni, Mn, Cu, Ge and Ag and the L-shells of Xe, Kr and W by x-ray yield measurements indicate that the exponent α is indeed close to unity [49–54]. This conclusion is supported by results of Hink et al. [55] for K-shell ionization of Ne, obtained from Auger electron yield data.

Note that the Bethe equation produces formally a linear energy dependence of the cross section near the threshold. As pointed out by Wannier [47] such a behaviour of the Born approximation result is a corollary of neglecting electron-electron interaction. Later theoretical studies [48,56] based on quantum mechanical treatment of the three-body problem of which the ionization at the threshold represents one of the examples completely confirmed this argument. A detailed analysis of the correlated electron wave functions in hyperspherical coordinates can be found the review paper by Fano [48]. A quasiclassical solution of the problem was found by Peterkop [56]. Since the Wannier exponent 1.127 does not differ too much from unity the Bethe equation can be easily modified to produce empirical formulas [57,58] being in good agreement with experimental data [49,51,52].

From the above considerations it follows that although the Bethe formula is valid only in the high overvoltage limiting case $U_{nl} \geq 10^2$ expression (2.6) remains a useful guide for the energy dependence of the core-ionization cross section in the entire energy range of practical importance for quantitative AES analysis. Some additional insights into this relatively good performance of the Bethe equation in the region where the perturbation theory formally breaks down can be found upon a close inspection of a multipole expansion of the transition matrix element derived

in the DWBA. Botero and Macek [33] found that for intermediate U_{nl}-values the quadrupole-term contribution becomes significant and a dipole approximation is no longer valid. It is interesting, nonetheless, that amplitudes of different multipoles obtained in the CWBA and PWBA are very similar, while their phase shifts are different [33].

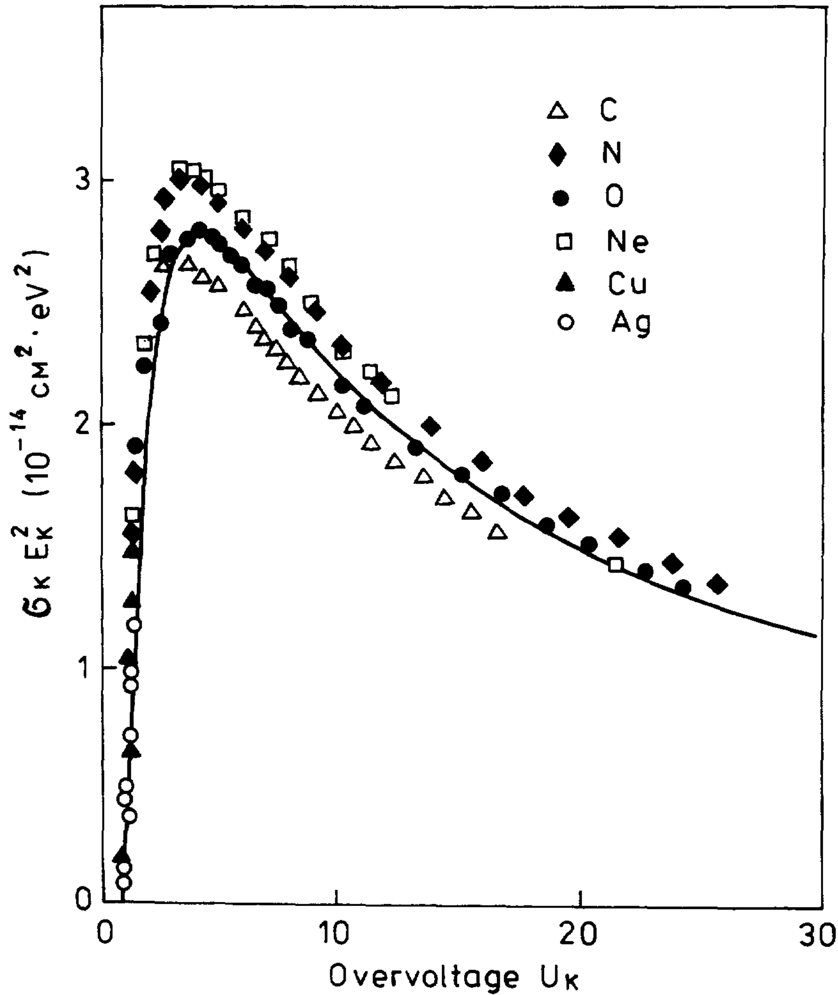

Fig. 1. The overvoltage dependence of the K-shell ionization cross section. The solid curve is the Bethe equation with the parameters b=0.9 and c=0.65 [20]. Experimental data: open triangles - C, black diamonds - N, black circles - O, open squares - Ne [59]; black triangles - Cu, open circles - Ag [52].

In Fig.1 the overvoltage dependence of the K-shell ionization cross section (multiplied, for convenience, by the excitation energy E_K of the K-shell, squared) on the overvoltage is shown as

an example. The solid curve represents the results of calculation by the Bethe equation (2.6) for the parameters $b_K = 0.9$ and $c_K = 0.65$ [20]. Also shown are the experimental data of Glupe and Mehlhorn [59] for C (open triangles), N (black diamonds), O (black circles), Ne (open squares) and of Shima et al. [52] for Cu (black triangles) and Ag (open circles).

Another widely used formula for the ionization cross section that should be mentioned is the result of Gryzinski [24] obtained from a classical description of a collision event:

$$\sigma_{nl} = (\pi e^4/EE_{nl})Z_{nl}g(U_{nl}), \tag{2.7}$$

where the function $g(x)$ is defined by

$$g(x) = [(x-1)/(x+1)]^{3/2}\left\{1 + (2/3)\left[1 - (1/2x)\ln[2.7 + (x-1)^{1/2}]\right]\right\}. \tag{2.8}$$

The Grysinski formula proved to be effective when describing the ionization probability in the intermediate overvoltage range [22]. Expression (2.7) was found under the assumption of a direct Coulomb interaction between the incoming and bound electrons and underestimates the cross section in the vicinity of the threshold ($x - 1 \ll 1$).

The influence of solid state on the inner-shell ionization probability comprises mainly two points. First, the core-energy levels are slightly shifted as compared to those of isolated atoms. Secondly, the structure of unoccupied states in the valence band may be essentially different from the structure of excited levels in an atom. As a result, the contributions to the ionization probability, arising from a collision accompanied by a transition of the core-shell electron to the valence band in a solid and to a weakly bound state in an atom are generally different. Those contributions, however, do not affect significantly the total inner-shell ionization cross section as the latter is dominated by excitation of continuum states [36].

B. Auger effect

A core-shell vacancy in an atom can be filled in different ways. One of them is a radiationless transition, resulting in emission of a characteristic Auger electron [60,61]. In this process, an electron from a higher subshell or shell neutralizes a hole and the excess of energy is transferred to a second electron either from the same or some other shell. If the vacancy is filled by an electron from the same shell the process is referred to as a Coster–Kronig transition [62]. Otherwise the term *Auger transition* is used. In fact, the Coster–Kronig transition is a particular case of the Auger effect [63], though very often these radiationless transitions are treated separately [64]. The

reason is that in order for the first type of the process to take place with a significant probability the energy gap between the two subshells has to be large enough to provide an amount of energy necessary for ionization of a nearest shell (subshell) with a lower binding energy. The latter requirement is not always fulfilled. For example, for elements with the atomic numbers Z such as $50 < Z < 74$ the process $L_1L_3M_{4,5}$ turns out to be impossible due to the energy conservation law [63,65]. Contrary to this, in the case of Auger transition, the released energy is always sufficient to eject a second electron from the atom since the ionization potential decreases rapidly with increasing a principal quantal number of an atomic orbital.

In accordance to these remarks, the Auger yield a^{i}_{X} represents the probability that a vacancy in the ith subshell of a certain shell X is filled by a radiationless transition of an electron coming from a higher shell [64]. The quantity a^{i}_{X} does not include the contribution of Coster–Kronig processes. Similarly, the Coster–Kronig yield f^{ij}_{X} is defined as the probability for an hole of the subshell i to be neutralized by an electron from a higher subshell j of the same shell X [64]. Since the total probability to fill a vacancy is unity we arrive at the relationship

$$\omega^{i}_{X} + a^{i}_{X} + \sum_{j} f^{ij}_{X} = 1 \tag{2.9}$$

where ω^{i}_{X} is the so-called *fluorescence yield* characterizing the probability that a hole is filled through a radiative process [64]. Relationship (2.9) becomes especially simple in the case of K-shell vacancy as Coster–Kronig processes are not possible. Thus, we have $\omega_K + a_K = 1$. Hence, measurement of a number of photons emitted from a sample, per one vacancy filled provides a direct means to determine the Auger transition probability a_K. The situation is much more complicated in the case of higher shells owing to the possibility of Coster–Kronig transitions. In quantitative AES analysis the Auger electron line intensity is proportional to the yields a^{i}_{X} or f^{ij}_{X} [14]. Therefore, evaluating the radiationless transition probablities is a necessary step in processing AES experimental data.

There are two ways of interpreting the physical picture of the Auger effect. In the simplest version, the Auger transition is believed to be due to Coulomb repulsion between two electrons which push each other away so that one electron is ejected from the atom while the other fills the vacancy [63]. A more general explanation is based on a concept of internal conversion. Thus, one electron first drops to the lower shell, neutralizing a hole and emitting a photon. The photon is then absorbed by the second bound electron, supplying the latter by an amount of energy sufficient to escape from the atom. Parilis [63] points out that, in the nonrelativistic treatment, both pictures lead to identical results. However, the full relativistic consideration indicates that

the Auger transition occurs through an internal conversion. Thus, the Auger effect represents an internal conversion process in which two identical particles (electrons) take part [63].

The number ν_A of Auger transitions per unit time can be calculated from *Fermi's golden rule* [64,66]. Consider for simplicity a two-electron process and neglect for a while relativistic corrections. Then the quantity ν_A reads

$$\nu_A = \hbar^{-2} \mid D - E \mid^2, \tag{2.10}$$

where D and E represent the direct and exchange matrix elements. Particularly, the element D is given by

$$D = \int \chi_f(\mathbf{r}_1)\psi_f(\mathbf{r}_2)[e^2/r_{12}]\chi_i(\mathbf{r}_2)\psi_i(\mathbf{r}_2)d\mathbf{r}_1 d\mathbf{r}_2, \tag{2.11}$$

Where $\chi_{i,f}(\mathbf{r}_1)$ and $\psi_{i,f}(\mathbf{r}_2)$ are the initial (i) and final (f) wave functions of electrons 1 and 2, respectively, and $r_{12} =\mid \mathbf{r}_1 - \mathbf{r}_2 \mid$ is the distance between the two electrons. The function χ_f describes the continuum electron and is normalized in such a way that the total flux of Auger electrons crossing a sphere of a large radius R_0, centered at the atom, is equal to unity [64]. The quantities χ_f, ψ_i and ψ_f correspond to wave functions of bound states. The exchange term E differs from D in the interchange of arguments of the final state functions $\mathbf{r}_1 \rightarrow \mathbf{r}_2$ and $\mathbf{r}_2 \rightarrow \mathbf{r}_1$. The physical meaning of the exchange term in (2.11) is schematically illustrated in Fig. 2. To find the total radiationless transition probability for filling a certain vacancy it is necessary to take a properly weighted sum of quantities ν_A pertaining to all possible processes in which energy, parity and angular momentum are conserved [64].

From (2.11) it follows that the Auger transition probability is to a large extent determined by the degree of overlap between the initial and the final wave functions as well as by the momentum of the ejected electron. Generally, the transition rate ν_A can be written as

$$\nu_A = \gamma/\tau_0 \tag{2.12}$$

In the latter expression $\tau_0 = a_0/v_0 = 2.42 \cdot 10^{-17}$ s is the atomic unit of time. The constant γ is typically of the order of 0.01–0.03 for KLL-transitions, and increases slowly with the atomic number Z (*cf.* Fig. 3). The situation is entirely different for LMM Auger electrons. According to calculations of ref. [67] LMM Auger transition rates may vary by several orders of magnitude depending on Z. Thus, for elements ranging from Mg to U the parameter γ augments from about $4 \cdot 10^{-4}$ to 1. Thus, a typical time of KLL-Auger electron emission amounts to $\tau_A \sim 10^{-14} - 10^{-15}$s and is large compared with the atomic time ($\tau_A \gg \tau_0$). Contrary to this, a typical time needed for LMM transitions in heavy atoms is of the order of τ_0 . This behaviour of KLL and LMM

transition rates can be understood qualitatively from the internal conversion picture. Consider, for instance, the KLL-transition case and denote the corresponding transition rate by ν_{KLL}. The quantity $\nu_{KLL} \sim \sigma_{ph}^{L} \nu_{\gamma}^{KL}$, where σ_{ph}^{KL} is the radiative transition rate for a process of filling a vacancy in the K-shell by an electron from the L-shell, while σ_{γ}^{KL} is the photoelectric cross section proportional to the probability of absorbing a photon by another electron of the L-shell. The energy of the photon is about the binding energy of the K-shell electron, *i.e.* $\sim Z^2 e^2 / a_0$. Therefore, the probability of L-shell ionization by such a photon is roughly inverse proportional to Z^4 (*cf.* the assessments of photoelectric cross sections in Section 2C). On the other hand, the quantity $\nu_{\gamma}^{KL} \sim Z^4$ [64]. Thus we obtain that ν_A is nearly constant for large $Z \gg 1$.

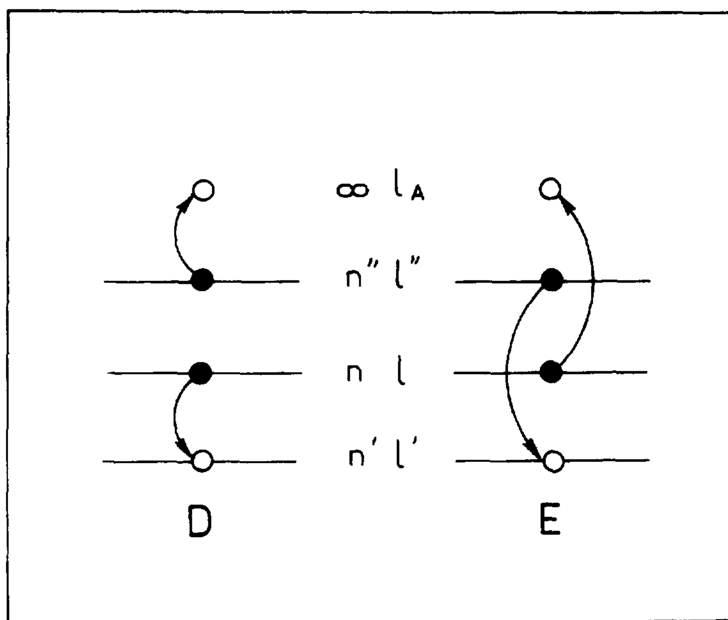

Fig. 2. Schematic illustration of the physical meaning of the exchange interaction contribution to the Auger transition rate (after ref.[64]).

Equation (2.10) is obtained in the framework of a perturbation theory and, is valid under the assumption that the electron-electron interaction is small compared with the absolute value of potential energy of electrons in the screened field of a nucleus. Besides that, the Auger emission time τ_A is assumed to be large compared with the typical interaction time $\tau_{int} \sim a_0/v$ where v is the Auger electron velocity. The inequality $\tau_A \gg \tau_{int}$ allows to use the *sudden* approximation when calculating the wave functions of the initial and the final states.

Until now, the Auger transition rates have been calculated by means of screened hydrogenic

wave functions [68–73] and Hartree–Fock–Slater wave functions for the potential of Herman and Skillman [67,74–78]. The results obtained by different authors for KLL-transitions compare relatively well except for a slight local structure of the KLL-transition rate dependence on the atomic number, found by McGuire [75,76]. Walters and Bhalla [78] ascribe this to approximations adopted in the algorithm of refs. [75,76] to evaluate Hartree–Fock–Slater wave functions.

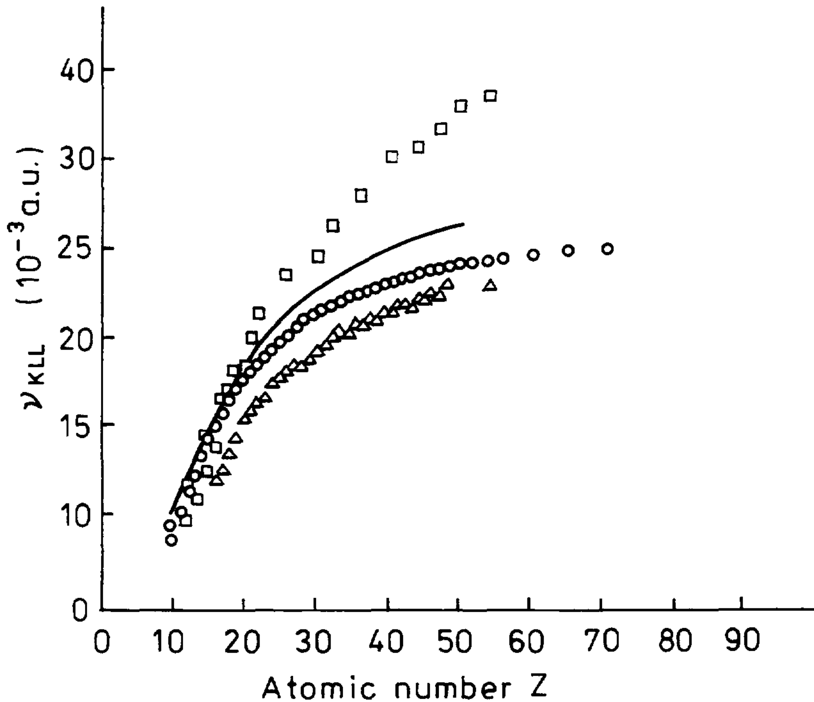

Fig. 3. The theoretical dependence of the KLL-transition rate on the atomic number Z. Solid curve – calculations by Walters and Bhalla [78], open squares, circles and triangles are the results of McGuire [75,76], Kostroun et al. [72] and Callan [64], respectively.

The experimental values of the fluorescence yield ω_K can be used to determine the KLL-Auger yield a_K. In Fig. 4 the quantity a_K obtained from formula (2.9) and the most reliable experimental data [64] is displayed as a function of the atomic number Z. Also shown here are the theoretical results of ref. [72] and the semi-empirical curve calculated from the expression

$$a_K = b(b + Z^{\mu}) \tag{2.13}$$

with the parameters $b = 1.16 \cdot 10^5$ and $m = 3.36$ [79]. Slightly different values $b = 9.5 \cdot 10^5$ and

$m = 4.0$ were proposed in ref. [80].

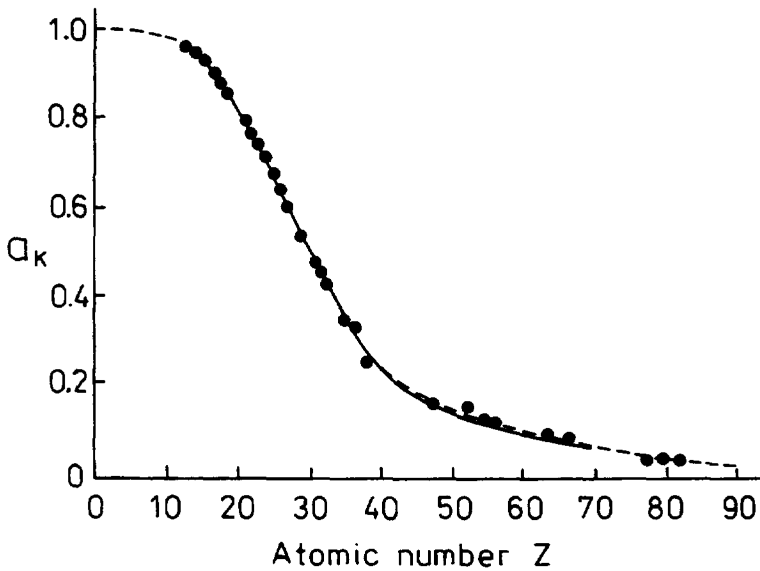

Fig. 4. The KLL-Auger electron yield versus the atomic number. Data points – experiment [64], solid curve – calculations by Kostroun et al. [72], dashed line – semiempirical (formula (2.13)).

Determination of LMM and MNN Auger yields is possible by making use of experimental data for corresponding radiative transitions [64,80]. One should keep in mind, however, that this implies knowledge of relevant Coster–Kronig transition rates whose values are not always available with sufficient accuracy.

Generally, the theory of the Auger effect encounters the same problems as those one faces when describing a photoionization process. Accurate values of Auger electron binding energies and realistic intrinsic energy spectra can be found by applying sophisticated procedures to determine multiple-electron wave functions of the initial and final states. Unfortunately, such detailed calculations are often tedious and difficult. Although intensities of a given Auger electron group can be reliably predicted, calculation of the relative contributions of different subgroups still remains a problem especially when Coster–Kronig transitions and valence electrons are involved [81].

C. Photoionization

The process of photoionization is a hard core of photoelectron spectroscopies. The kinetic energy E of a released photoelectron is, to first approximation, equal to the difference of the photon energy $\hbar\omega$ and the binding energy E_{nl} of the electron in the nl–shell $E = \hbar\omega - E_{nl}$. Since the photon energy is fixed and the binding energy is specific for each shell and element analysis of the energy spectra of photoelectrons provides an effective means to study an elemental composition of a target.

In practice, this picture turns out to be oversimplified. XPS spectra do not reduce to lifetime broadened peaks but represent resolved structures with satellites accompanying a principal line. In metals, for example, a complex shape of a photoelectron line is due to the collective response of conduction-band electrons to the creation of a hole [82]. Thus, in the vicinity of the main peak the so-called *intrinsic* plasmon peaks may occur. The intrinsic plasmons should be distinguished from the extrinsic ones associated with the energy losses of a photoelectron escaping from a sample [11]. The appearance of satellites is due to the so-called *shake up* and *shake off* effects, or more generally, to configuration interaction. Accounting for this kind of interaction stipulates going beyond the single-configuration Hartree–Fock approximation and representing the initial and the final wave functions of a system via linear combinations of different electron configurations. Some terms in these representations may have close values of a ground state energy and comparable contributions to the resulting wave function. For the initial and the final wave functions this leads to the *shake up* and *shake off* satellites, respectively [11]. Following Wertheim [82] we consider a simple example of the final-state effect first identified in XPS analysis of alkali atoms.

In Fig. 5 the XPS spectrum of KF, measured experimentally [82] is shown by data points. The K 3s and F 2s peaks are accompanied by an unusually strong satellite whose intensity is comparable with that of F 2s line. Note that in closed-shell atoms s-photoelectrons give rise to broad single lines. In our case, however, K ion has an empty 3d-subshell. Therefore, in addition to the reaction $3s^2 3p^6 + \gamma \to 3s^1 p^6 + e$ with the final state symmetry ^2S of K^{++} there is also a possibility for the channel $3s^2 3p^6 + \gamma \to 3s^2 3p^4 3d^1 + e$ characterized by the same symmetry of the final configuration. In the latter case a p-electron is promoted to the normally empty d-orbital and a two-hole state is created instead of a single hole in the s-orbital as it is in the first situation. It should be stressed that identity of the final-state symmetries is essential as the two-hole configuration cannot be directly excited by photoelectric interaction [82]. On the other hand, the contribution of the $3s^2 3p^4 4s^1$ state to the final wave function is small due to a weak

overlapping of the third and the fourth shells [83,84]. The state $3s^2 3p^4 4s^1$ corresponds effectively to a higher photoelectron binding energy as compared to the principal configuration $3s^1 3p^6$ (50 eV versus 35 eV) while the shake off-satellite peak intensity is about 25% of main peak. Similar spectra are expected to occur for 3s and 4s electrons of the 3d and 4d group transition metals, respectively, and 4p electrons in the vicinity of rare earths [82].

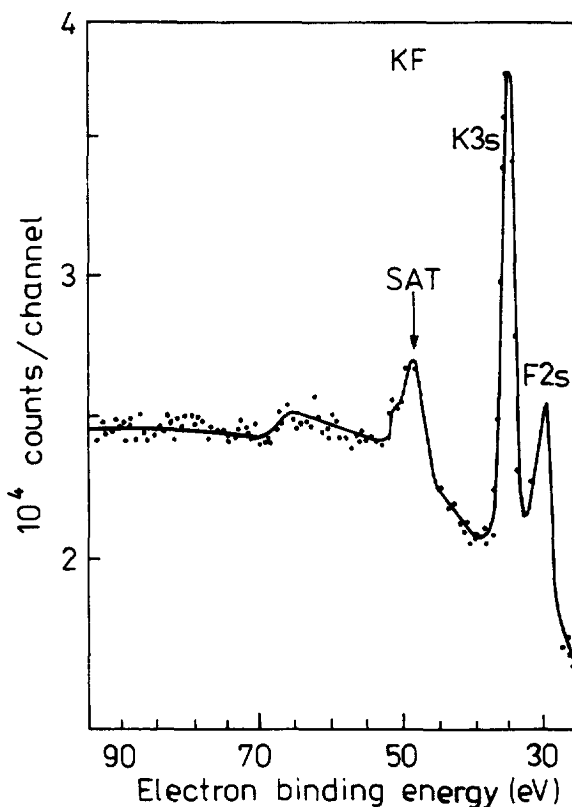

Fig. 5. Final-state configuration satellite of K 3s in KF (after ref.[82]).

The photoelectron line intensity is directly proportional to the probability of photoionization and therefore, methods of calculation of a photoelectric cross section occupy a considerable space in the theory of XPS [84,85]. The differential photoelectric cross section $d\sigma_{ph}$ is equal to the ratio of a number $d\nu$ of electrons emitted from an atom with the momentum (**p**,**p**+**dp**) per unit time to the flux F of incident photons. Thus, we have

$$d\sigma_{ph} = d\nu / F \tag{2.14}$$

The major peculiarities of core-shell photoionization can be discussed in terms of the simplest *one-electron* and *sudden* approximations [11]. The first of them implies that the initial multiple-electron wave function can be split into an antisymmetrized product of the *active* orbital ψ_{nl} and an $(N-1)$-electron remainder, where N is the total number of atomic electrons [11]. The final state is described in a similar way. The sudden approximation assumes that the excitation of the nl-subshell occurs rapidly enough so that the distribution of *passive* electrons does not change significantly. The criterion of validity of this assumption is given by the inequality $\tau/T \ll 1$, where τ and T are the typical interaction and relaxation times of the system. The interaction time τ is about a_0/v, where v is the photoelectron velocity. In the energy range from several hundred eV to several keV the quantity $\tau \sim 10^{-17}$ s. Assuming that relaxation of the $N-1$ electron system occurs through a series of Auger transitions we have $T \sim 10^{-14}$ s [63] and the requirement $\tau \ll T$ is well fulfilled.

Under the aforesaid assumptions the number of electrons leaving an atom with the momentum p in the direction Ω within an elementary solid angle $d\Omega$ per unit time reads [[36]

$$d\nu = (2\pi\hbar^2)^{-2} \mid M_{if} \mid^2 \delta(p^2/2m - \hbar\omega + E_{nl})p^2 dp d\Omega, \tag{2.15}$$

where ω is the frequency of incident photons and the matrix element M_{if} is given by the integral

$$M_{if} = \int \psi_f \hat{H} \psi_i d\mathbf{r}. \tag{2.16}$$

Here $\hat{H}$ is the part of the Hamiltonian describing the interaction of the atomic electron with the incident radiation, ψ_i and ψ_f stand for the initial and the final electron wave functions, respectively. Under the assumptions of a weak electromagnetic wave propagating in a uniform medium the perturbation $\hat{H}$ can be approximated as $\hat{H} = -(e/mc)\mathbf{A}\hat{\mathbf{p}}$ [11,87]. In the latter formula $\hat{\mathbf{p}} = -i\hbar\nabla$ is the momentum operator and $\mathbf{A}$ is the vector potential. The vector potential is calibrated in such a way that its divergence is zero, $\nabla \cdot \mathbf{A} = 0$. The wave length of incident photons λ is usually large compared with the effective radius a_{nl} of a subshell from which emission occurs $(\lambda \gg a_{nl})$. Therefore, variation of the vector potential over the effective region of integration in expression (2.16) can be neglected and the quantity $\mathbf{A}$ may be replaced by $\hat{\mathbf{e}}A_0$ where $\hat{\mathbf{e}}$ is a unit vector in the direction of polarization and A_0 is the amplitude of the vector potential.

Performing integration over the absolute value of the momentum in the right-hand side of expression (2.15) and substituting the result obtained into (2.14) we arrive at the equation

$$d\sigma_{ph} = (2\alpha/\pi)(v/\omega) \mid m_{if} \mid^2 d\Omega, \tag{2.17}$$

where the *fine structure constant* $\alpha = e^2/\hbar c$ and the reduced matrix element

$$m_{if} = \hat{\mathbf{e}} \int \psi_f \nabla \psi_i d\mathbf{r} \tag{2.18}$$

are introduced. When deriving expression (2.17) we took into account the explicit formula for the photon flux $F = < S > /\hbar\omega = \omega_0^2 A/8\pi\hbar c$. Here the notation $< S >$ is used for the average value of the Pointing vector.

At this stage, it is advisable to make some qualitative assessments. In order to do so, the electron wave functions are to be specified. Suppose the final state is described by a plane wave $\psi_f \sim \exp(i\mathbf{kr})$, where $\mathbf{k} = \mathbf{p}/\hbar$ is the electron momentum in units of the Planck constant. Such an assumption is well substantiated for relatively fast photoelectrons when the energy of the incident photon $\hbar\omega$ greatly exceeds the ionization threshold E_{nl} $(\hbar\omega \gg E_{nl})$. Without loss of generality, the initial wave function is assumed to decay very rapidly at distances $r \geq a_{nl}$ and to be normalized to unity. For simplicity, we set

$$\psi_i \sim (\pi a_{nl}^3)^{-1/2} \exp(-r/a_{nl}). \tag{2.19}$$

The wave function defined by formula (2.19) corresponds to a spherically symmetric ground state and for $a_{nl} = a_0/Z$ coincides with that of the K-shell electron. Making use of these simple wave functions we find that the reduced matrix element squared is of the order of $| m_{if} |^2 \sim 16\pi a_{nl}/(ka_{nl})^6$ since the major contribution to integral (2.18) is provided by the region of integration $r \sim k^{-1}$. Substitution of this result into Eq. (2.17) and subsequent integration over the emission angles yields the estimate for the total photoionization cross section

$$\sigma_{ph} \sim 2^7 \pi \alpha a_0^2 (a_0/a_{nl})^{-5} [I_0^{7/2}/\hbar\omega(\hbar\omega - E_{nl})^{5/2}], \qquad (\hbar\omega \gg E_{nl}), \tag{2.20}$$

where $I_0 = e^2/a_0 = 27.2$ eV. From these elementary considerations some important inferences can be made. As seen from (2.20) at high energies $\hbar\omega \gg E_{nl}$ the cross section diminishes quite rapidly with the photon energy. The power law $\sigma_{ph} \sim E^{-\gamma}$, where E is the photoelectron energy, with the parameter $\gamma = 2.5$ is in qualitative agreement with experimental data for Ne 2s subshell ionization $(\gamma \sim 2.0)$ [88]. Another scaling relationship follows for the ratio of K-shell photoionization cross sections of elements 1 and 2 at a fixed photon energy $\hbar\omega$. Since for the K-shell the effective radius $a_{nl} = a_0/Z$ we find from (2.20)

$$\sigma_{ph,1}/\sigma_{ph,2} = (v_2 Z_1/Z_2 v_1)^5, \tag{2.21}$$

where the photoelectron velocities v_1 and v_2 are introduced for convenience. Equation (2.21) may be useful for rough estimates of s-shell photoionization probabilities for elements with close

Z-numbers. For instance, the ratio of cross sections $\sigma_{F1s}/\sigma_{Ne1s}$ for the case of s-electrons excited by Ti Kα radiation is equal to 0.52 as it follows from (2.21). This compares satisfactorily with the value 0.66 obtained from accurate quantum-mechanical calculations [89]. Finally we note that the photoionization cross section reaches its maximum value $\sigma_{ph}^{m} \sim \pi a_{nl}^{2}$ at the photon energy $\hbar\omega \sim E_{nl}$. Since the effective radius of a shell ranges from a_0/Z to about a_0 we conclude that the quantity σ_{ph}^{m} is typically within the interval $(1/Z^2, 1)\cdot 10^2$ Mb. As an example, in Fig. 6 the energy dependence of the photoionization cross section for the 2s shell of Ne, obtained experimentally [88] and theoretically [90].

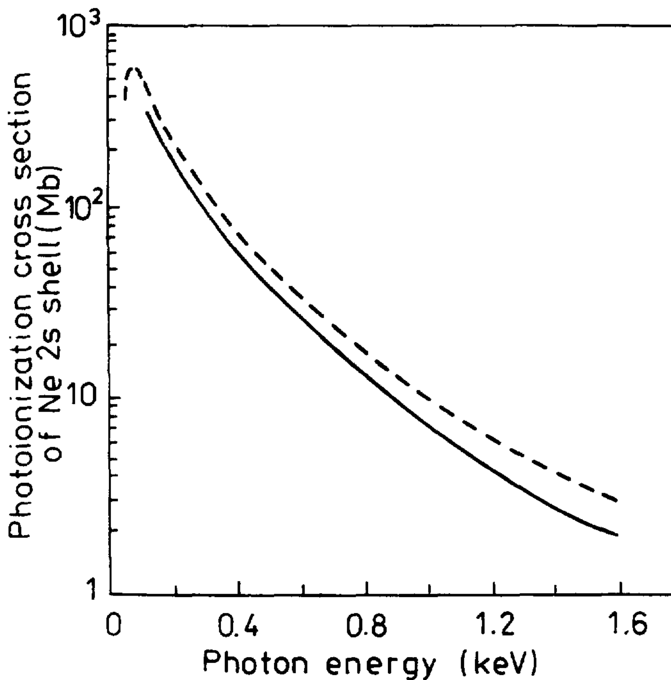

Fig. 6. The energy dependence of the Ne 2s shell photoionization cross section. Solid curve – experimental results [88], dashed line – Hartree–Fock calculations (velocity form) by Kennedy and Manson [90].

At present, a starting point to determine reasonably good wave functions of the initial and final states is the self-consistent-field method of Hartree– Fock [11,91,92]. This approach is based on the assumption that the wave function of an N-electron system can be approximated by a Slater determinant of N orthonormal single-electron spin-orbitals [11]. The optimum wave function is obtained from the condition of minimum of the total energy by applying the variational principle. A weak point of this technique is that some of experimentally observed many-electron

phenomena cannot be explained. To account consistently for correlation effects a number of more sophisticated methods have been proposed. Among them there are the continuum configuration interaction method of Fano [93,94], the close-coupling method [95–97], the R-matrix theory [98,99], the many-body perturbation theory [100–102], the random-phase approximation with exchange [103–109] and a relativistic modification of the latter [110–112].

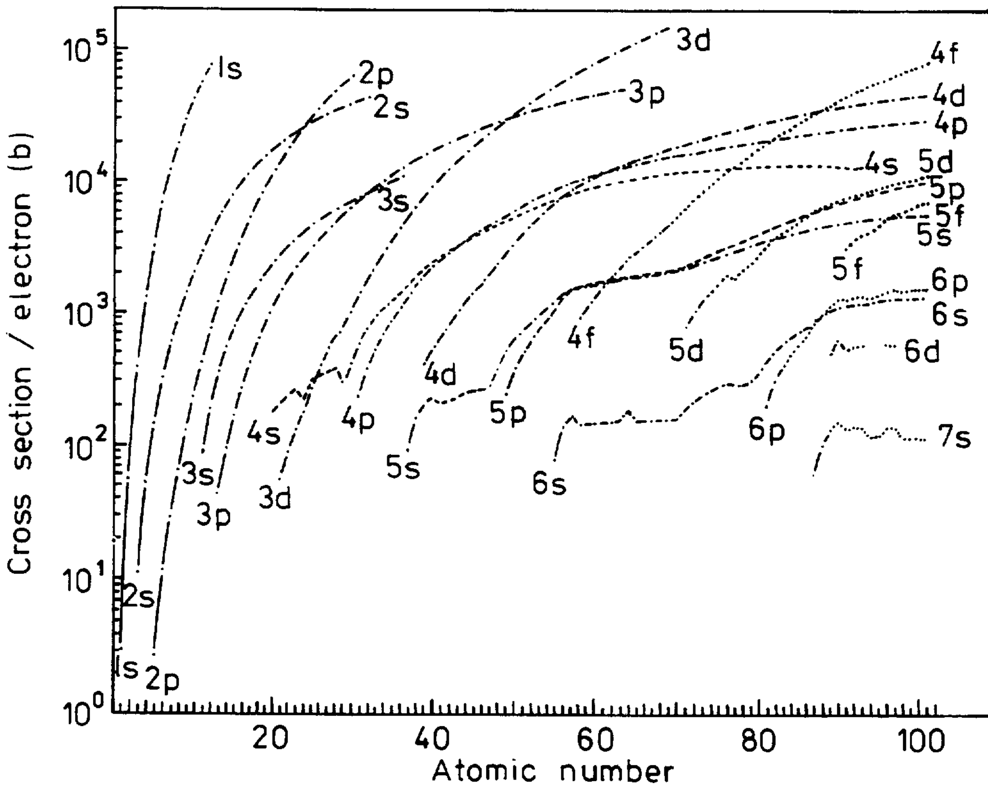

Fig. 7. Photoionization cross sections per electron (barns) for the atomic subshells versus atomic number of the element (after ref. [85])

In the method of Fano [93], the continuum eigenfunction of the exact non- relativistic Hamiltonian $\hat{H}$ are expanded into a series on eigenfunctions of the approximate Hamiltonian $\hat{H}'$. Thus, the solution of the Schroedinger equation for the probe Hamiltonian $\hat{H}'$ allows to generate a set of eigenfunctions in the zeroth order approximation. It is assumed that such a solution can be found accurately enough, therefore selection of the operator $\hat{H}'$ is a crucial point in this approach. The close-coupling formalism stipulates that the wave function of the continuum state be presented by a series on functions $\psi_n F_n$, where ψ_n and F_n are the eigenfunctions of the residual ion and photo-

electron, respectively [86]. The unknown functions F_n can then be found by the Kohn variational principle [113]. The scheme of the many-body perturbation theory implies starting with a certain basis set of eigenfunctions and treating the total Hamiltonian of the system as a perturbation to find an approximate solution. Some classes of perturbation terms can be accounted for to infinite order, in the random-phase approximation [86,103–112]. This is achieved, however, at expense of omitting certain perturbation corrections. A more detailed discussion of various approaches used for accurate calculation of the photoelectric cross section can be found in ref. [86].

Figure 7 shows the theoretical photoionization cross sections per electron in barns [85] compiled by Scofield [114]. The cross sections were calculated by the relativistic Hartree–Fock–Slater wave functions for the excitation energy $\hbar\omega = 1500$ eV. To obtain an actual cross section a data-point from Fig. 7 should be multiplied by the number of electrons in a subshell or a valence band. Thus, for fully occupied core orbitals one has to multiply the intensity by 2 for s–, 4 for $p_{3/2}$–, 6 for $d_{5/2}$ -photoelectrons and so on [85].

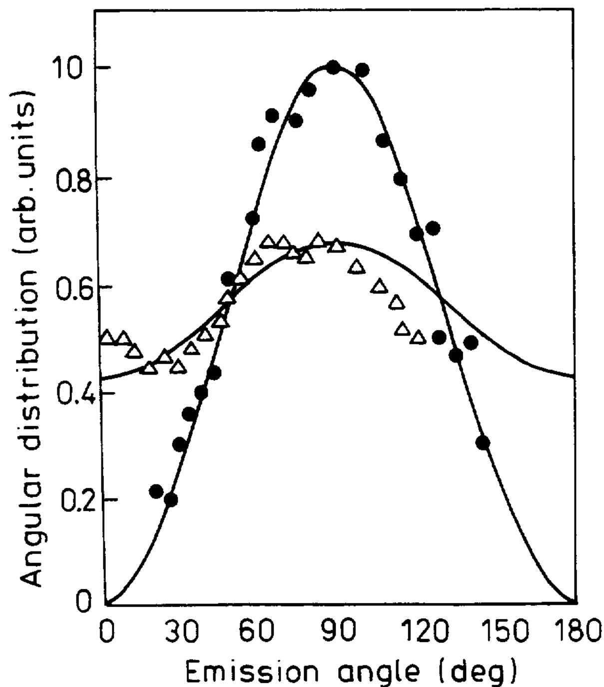

Fig. 8. Angular distributions of 2p and 3s photoelectrons ejected from Ne and Kr atoms, respectively. Experiment: open triangles – Ne [88], black circles – Kr [116]. Solid curves – analytical calculations from (2.22). The 3s-curve is normalized to unity at maximum.

The angular distribution of photoelectrons irrespective of their energy can be found indepen-

dently of dynamics of the ejection process in the dipole approximation [86]. The corresponding differential photoelectric cross section reads

$$d\sigma_{ph}/d\Omega = (\sigma_{ph} = /4\pi)[1 - (\beta/4)(3\cos^2\Theta - 1)] \tag{2.22}$$

where Θ is the angle between the photon propagation direction and the momentum of the photoelectron, while β is the asymmetry parameter. Formula (2.22) is valid for unpolarized or completely circular polarized radiations [115]. In particular, for s-photoelectrons the asymmetry parameter $\beta = 2$ as follows from (2.17)–(2.19). In Fig. 8, the experimental angular distributions for Ne 2p and K 3s photoelectron lines excited by Mg Kα radiation [88,116] are shown by data-points. Also displayed for comparison are the theoretical distributions obtained from formula (2.22) and normalized to unity. Calculations are made for the asymmetry-parameter values $\beta_{3s} = 2.0$ and $\beta_{2p} = 0.70$ [89]. The analytical results are seen to be in good agreement with the experimental data.

Extensive tabulations of photoelectric cross sections for photoelectron lines excited by x-rays emitted by major anodes used in XPS (*cf.* Table 1) can be found in ref. [89].

TABLE 1. Energies and Widths of Basic X-ray Lines Used in XPS [88,117].

X-rays	Energy (eV)	Width (eV)	X-rays	Energy (eV)	Width (eV)
Y Mζ	132.3	0.47	Mg Kα	1253.6	0.7
Zr Mζ	151.4	0.77	Al Kα	1486.6	0.85
Nb Mζ	171.4	1.21	Si Kα	1739.5	1.0
Mo Mζ	192.3	1.53	Y Lα	1922.6	1.5
C Kα	278	6.0	Zr Lα	2042.4	1.7
Ti Lα	395.3	3.0	Ag Lα	2984	
Cr Lα	572.8	3.0	Ti Kα	4511	2.0
Ni Lα	851.5	2.5	Cr Kα	5414	2.1
Cu Lα	929.7	3.8	Cu Kα	8048	2.6

D. Elastic scattering of medium energy electrons on atoms

Elastic scattering influences both signal electron attenuation in AES/XPS and penetration of primary electrons in AES. This kind of interaction is responsible for the electron momentum relaxation and is mainly due to scattering in the Coulomb field of an atomic nucleus. The

strength of the atomic field increases rapidly with decreasing the distance between the nucleus and incoming electron. As a result, the probability of elastic scattering is dominated by small-impact parameter collisions, characterized by impact parameter $b < a_0$. Being negatively charged an electron can penetrate deep into the atomic core region. The electron energies relevant to AES/XPS are of the order of or less than the typical absolute value of the potential energy of electron-atom interaction. As a result, the electron wave length λ becomes comparable with the Thomas-Fermi screening radius $a \sim 0.885 a_0 Z^{-1/3}$, where Z is the nuclear charge. Hence, the quantity λ is of the order of the typical distance over which the atomic potential changes noticeably. Resorting to an optical analogy and treating the atomic core region as a source of secondary electron waves one might expect pronounced diffraction effects in the probability of large angle scattering under the condition $\lambda \sim a$. From the dynamical point of view, in the region of distances $r \sim a$ an electron experiences most probably large-angle scattering and even orbiting [118]. The latter is a purely quantal effect forbidden in a classical picture of motion. It leads to appearance of a *rainbow structure* in the shape of the differential elastic scattering cross section [119].

It should be stressed that small-angle scattering caused by large-impact parameter collsions in the case of an isolated atom may be different from that for an atom imbedded in a solid. However, the influence of small-angle deflection events on the medium energy electron transport is rather weak since small-impact parameter collisions dominate. Hence, the problem of elastic interaction in solids may be reduced to a calculation of the differential elastic cross section for electron-atom scattering. The differential elastic scattering cross section can be evaluated by the R-matrix method [120], the method of polarized orbitals [121,122] and the optical model [123–125] including exchange and polarization effects. Fortunately, exchange and correlation effects in elastic scattering of medium energy electrons on atoms can be usually neglected and a simple optical model with an effective single particle potential can be applied. To show this we note, following [126] that the exchange interaction is of the order of the reciprocal of the mean distance between atomic electrons and is proportional to $\rho^{1/3}$, where ρ is the electron density. Denoting by V the absolute value of the potential interaction energy of an electron in a screened Coulomb field we find that $\rho^{1/3} \sim V^{1/2}$. Since the absolute value of the potential energy $V \sim Z^{4/3}$ in the atomic core region, the exchange interaction is small compared with V ($\rho^{1/3} \ll V$) everywhere except for the outer shell ridge of an atom, *i.e.* at distances $r \sim a_0$ where $V \sim V^{1/2} \sim 1$.

The short-range ($r < a_0$) and the long-range ($r > a_0$) parts of the correlation interaction are to be treated separately. The long-range correlation represents mainly polarization of outer shells

and is roughly proportional to the interaction time $\tau \sim 1/v \ll 1$. The short-range correlation interaction consists primarily of the potential fluctuations and has been shown in ref. [125] to be significantly less than the quantity V. Thus exchange and correlation may affect mainly small-angle scattering of fast electrons. Although elastic scattering takes place against the background of excitation and ionization of atomic shells, inelastic channels have been shown to influence insignificantly the elastic scattering probability [126].

Taking advantage of these estimates we can write the potential energy of interaction as a simple average over the atomic ground state $U(r) =< 0 \mid U \mid 0 >$. In the nonrelativistic case the differential elastic scattering cross section can be expressed via the scattering amplitude $f(\vartheta)$ [118,127]

$$d\sigma(\vartheta) = \mid f(\vartheta) \mid^2 d\Omega. \quad (2.23)$$

The quantity $f(\vartheta)$ can be found then from the quantal theory of scattering [127]

$$f(\vartheta) = -i\hbar/(2mE)^{1/2} \sum (l + 1/2)\{\exp(2i\delta_l) - 1\} P_l(\cos\vartheta), \quad (2.24)$$

where δ_l is the phase shift, $P_l(\cos\vartheta)$ is the Legendre polynomial and the summation is performed over all orbital numbers from $l = 0$ to ∞. The physical meaning of the phase shift δ_l can be easily traced out by noting that in the quasiclassical approximation [128] the product $\hbar\delta_l$ is equal to the difference of the full action of an electron of the momentum l/k, scattered in the central field $U(r)$, and that of a freely moving particle, or to the so-called *compensated classical action* [129]. A rough estimate of the number of terms contributing effectively to sum (2.24) can be obtained from the condition $b_{max} \sim a_0$, where b_{max} is the maximum impact parameter for a collision leading to a noticeable delfection of an electron. Since $b \sim l/k$ we find $l_{max} \sim ka_0$. Thus, at $ka_0 \ll 1$ ($E \ll 10$ eV) only the s-wave contributes significantly to the right-hand side of (2.24) while at the energy $E \sim 1000$ eV the number l_{max} may be about 10 and even higher.

The differential elastic scattering cross sections calculated from (2.23) and (2.24) for different realistic atomic potentials may vary slightly in their shape and especially in the small angle scattering region. Generalization of results (2.23) and (2.24) for the relativistic case can be found elsewhere [130,131]. The differences between relativistic and non- relativistic cross sections, as a rule, are within the limits of variations of the $d\sigma/d\Omega$-shape obtained for different potentials [129,132,133].

Figure 9 shows, as an example, the differential elastic scattering cross section for electron scattering at krypton at the energies of 100 and 500 eV. The dotted line represents the results of relativistic quantum mechanical calculations by the algorithm of Jablonski [134] for the

Thomas–Fermi–Dirac potential [135]. Also presented for comparison are the nonrelativistic quantum mechanical calculations [129] for the parameterized Hartree–Fock potential of Garvey et al. [136]

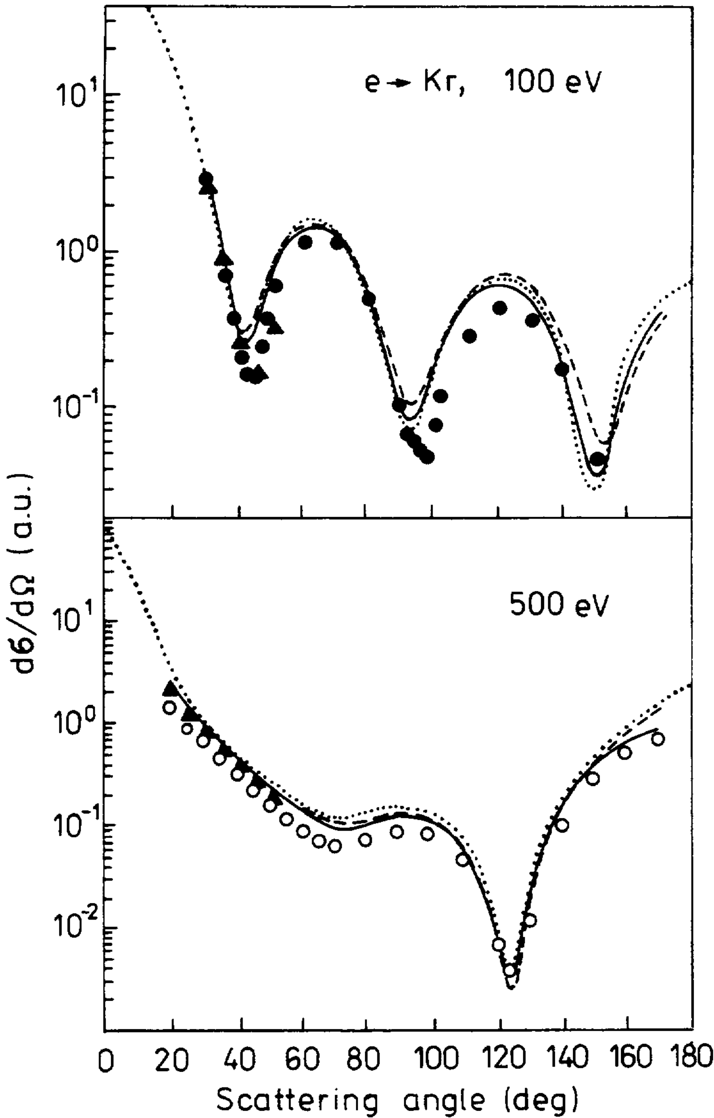

Fig. 9. Differential cross section for electron elastic scattering from Kr at the energies 100 and 500 eV. Solid and dashed curves are nonrelativistic quantum mechanical and semiclassical calculations, respectively [129]. Dotted line is relativistic quantum mechanical calculations by the algorithm of Jablonski [134]. Open circles are the numerical results of ref. [124]. Filled circles and triangles are experimental data from refs. [137,138].

(solid curve), semiclassical results [129] (dashed curve) and experimental data from refs. [137,138] (filled circles and triangles). Additionally shown by open squares are the results of calculations of ref .[124]. The diffraction oscillations of the differential cross section in the region of large scattering angles are seen to become more pronounced as the electron energy decreases from 500 to 100 eV and are well reproduced by the theoretical calculations pertaining to different potentials.

The quantity characterizing the average rate of electron momentum relaxation is the transport mean free path

$$\lambda_{tr} = (M\sigma_{tr})^{-1}, \tag{2.25}$$

where M is the atomic bulk density and σ_{tr} is the momentum transfer (or transport) cross section. The transport cross section is defined by the expression [36]

$$\sigma_{tr} = (4\pi/k^2)\sum_{l=0}^{\infty}(l+1)\sin^2(\delta_{l+1}-\delta_l). \tag{2.26}$$

The quantity σ_{tr} can be also found from direct integration of the differential elastic scattering cross section weighted with the function $(1-\cos\vartheta)$ over all scattering angles

$$\sigma_{tr} = \int_{4\pi} d\Omega(1-\cos\vartheta)d\sigma/d\Omega. \tag{2.27}$$

The difference $1-\cos\vartheta$ represents the relative change of the electron momentum in the initial direction of motion. Therefore, by its physical meaning, the transport cross section is proportional to the average probability of the momentum transfer along the particle velocity. Correspondingly, the transport mean free path is the pathlength to be travelled for the momentum change to be of the order of the initial electron momentum itself. Hence, the particles travelled in the target a pathlength λ_{tr} are expected to be scattered intensively at large angles.

From expression (2.27), it follows that the contribution of small-angle scattering events to the transport cross section is less pronounced, due to the presence of the factor $1-\cos\vartheta$. In other words, the small-impact parameter collisions play a major role in the electron momentum relaxation. This enables to describe elastic electron-atom interaction, when evaluating the quantity σ_{tr} by means of a simple Thomas–Fermi potential [126]. In particular, by applying the quasiclassical approximation. Tilinin [126] found that in the medium energy range the transport cross section is a universal function of the reduced electron energy

$$\varepsilon = Ea/e^2 Z^{4/3} \tag{2.28}$$

and can be presented in the form

$$\sigma_{tr} = \pi a^2 S(\varepsilon), \qquad (Z^{-2/3} < \varepsilon < Z^{2/3}). \tag{2.29}$$

The function $S(\varepsilon)$ is roughly inversely proportional to the reduced energy for $\varepsilon \ll 1$ and increases with ε according to the law $S(\varepsilon) \sim \varepsilon^{-1} \ln \varepsilon$. It is tabulated in ref. [126], where a number of analytical expressions for σ_{tr} are also derived for higher energy regions. An approximate formula for the universal function $S(\varepsilon)$ has been proposed recently [139]. In Fig. 10, the reduced momentum transfer cross section $\sigma_{tr}/\pi a^2$ is displayed as a function of the reduced energy ε. The results of calculations of ref. [126] (the universal function S) and experimental data of refs.[140–142] are shown by the solid curve and the data-points respectively. Also shown are the values of $\sigma_{tr}/\pi a^2$ calculated in refs. [120,146,144] for various elements of the periodic table. From Fig. 10 it is seen that the same curve fits a vast majority of data points. This may be regarded as an indication of the validity of dependence (2.29) in a broad interval of energies. Note that the quasiclassical approximation can be applied not only to evaluation of the quantity σ_{tr} but also to calculation of the differential elastic scattering cross section as shown by Burgdorfer et al. [129] if pseudoclassical path contributions to sum (2.26) are properly accounted for. The quasiclassical differential cross section for e-Kr elastic scattering [129] is shown in Fig. 9 and is in good agreement with both relativistic and nonrelativistic calculations.

The transport mean free path plays an important role in describing elastic scattering effects in AES/XPS [145]. The λ_{tr} -values have been tabulated recently in ref. [146] for the principal photoelectron line excited by Mg Kα and Al Kα radiations in 27 monoatomic targets.

E. Inelastic interaction. Inelastic mean free path

Inelastic interaction of signal electrons with solids is the major phenomenon affecting the surface sensitivity in AES/XPS. This interaction reduces mainly to polarization of matter an electron penetrates through. In contrast to elastic scattering, during an inelastic collision, a signal electron may loose a noticeable amount of energy and thereby not contribute to the characteristic peak intensity. Thus, attenuation of signal electrons in solids is primarily determined by inelastic scattering on their way out of a sample.

Quasi-free and weakly bound solid electrons response quickly to the electric field of a moving charged particle. On the other hand, the space positions of atomic nuclei remain almost unaffected due to a large ratio of the nucleon to electron masses. As a result, the equilibrium between positive (nuclei) and negative (quasi-free electrons) charges in a target turns out to be disturbed [147]. The displacement of negative charges leads to appearance of an additional electric field which tends to slow down the probe electron. Generally, the larger the period of time during which the

polarization takes place is, the more effectively the probe electron loses its energy. This, however, is true if there is a mechanism responsible for an irreversible energy transfer from the electron to numerous degrees of freedom of the solid. When the electron energy exceeds several ten eV,

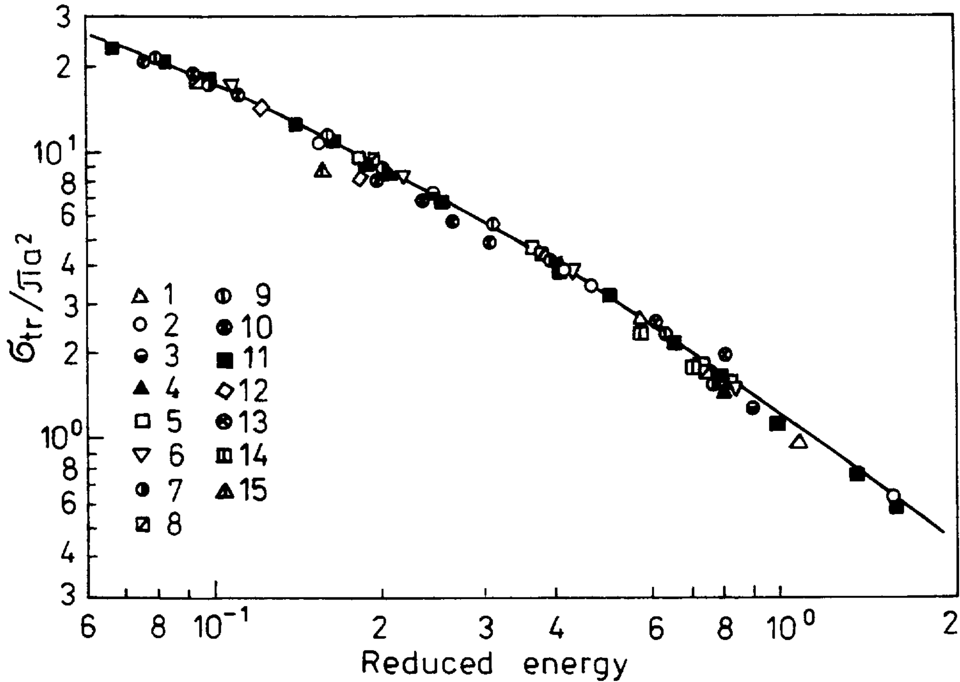

Fig. 10. The universal dependence of the reduced transport cross section for elastic scattering of electrons by complex atoms on the reduced energy ε. The solid curve represents calculations by formula (2.29) [126]. 1. Ti, 2. Cu, 3. Mo, 4. Ag, 5. Sn, 6. Ta, 7. Au, 8. Pb, 9. U – results of numerical calculations of ref. [143] for the energy range $E = 1.0$–8.0 keV; 10. Ne – R-matrix method, 50–200 eV [120]; 11. Xe – calculations based on generalized experimental and theoretical data, 0.3–10.0 keV [144]; 12. N – experimental data, 50, 75 eV [140]; 13. O, 14. Ar – experimental data, 0.3–1.0 keV [141]; 15. Ne – experiment, 100 eV [142].

then the energy is most probably transfered to the collective excitations of the quasi-free electron gas of the target (the so-called excitons and plasmons), or to individual conduction electrons undergoing interband or intraband transitions [148]. It should be emphasized that the idea of treating the ensemble of weakly bound solid electrons as a gas of non-interacting free particles first introduced by Zommerfeld (*cf.* [149]), *ab initio* suggests a quasi-particle representation. Each quasiparticle, in this picture, may be characterized as a separate oscillator with its effective mass, bond strength and damping coefficient [150]. Damping of the collective oscillation of the electron gas is eventually caused by electron-electron and electron-phonon scattering. The criterion of

validity of collective description requires that the mean time τ_c of collisions disrupting the collective motion be large compared with the typical period of oscillations [151], $\tau_c \gg 2\pi/\omega_p$, ω_p – the plasma frequency. This requirement is usually well satisfied for the most important electron-electron interactions of conduction electrons in a metal. Those are due to short-range screened Coulomb forces and, for an almost degenerate electron gas, characterized by a collision time much larger than $2\pi/\omega_p$ [151,152]. Note that, on the other hand, long range Coulomb forces are believed to be responsible for the organized behaviour of the electron gas [152]. As regards electron-phonon scattering, its typical collision time is even much greater than that of electron-electron collision and is about 10^{-12} s [151].

The response of the ensemble of solid electrons to the motion of the probe charged particle is described by a macroscopic electric field. In fact, as far as the energy losses of the probe electron are concerned, only the difference between the electric field $\mathbf{E}(\mathbf{r}, t)$ in the target and the electric field $\mathbf{E}_0(\mathbf{r}, t)$ created by the moving electron in vacuum matters. It is assumed that the difference between $\mathbf{E}$ and $\mathbf{E}_0$ is, to the first approximation, linearly proportional to the electric field of the projectile $\mathbf{E}_0$. The linear response theory was originally developed by Bohm and Pines in a series of papers [151–154] and by Lindhard [149] in the early fifties. Later different modifications of this theory have been used by many researches to describe inelastic scattering of medium energy electrons in solids [148,155–170]. The principal ideas of this approach are briefly considered below. Following ref. [147] we obtain for the energy losses of the probe electron per unit pathlength the equation

$$dE/ds = (e\mathbf{v}/v)[\mathbf{E}(\mathbf{v}t, t) - \mathbf{E}_0[(\mathbf{v}t, t)], \tag{2.30}$$

where the slowing down is assumed to be small so that the first derivative of the radius vector $\partial \mathbf{r}_0(t)/\partial t$ of the electron can be replaced by its velocity $\mathbf{v}$. Since a motion of a free charge in vacuum is not affected by its own field the second term in the right-hand side of Eq.(2.30) can be omitted and the energy losses read

$$dE/ds = (e\mathbf{v}/v)\mathrm{Re}\int d\mathbf{q}\int d\omega \mathbf{E}(\mathbf{q}, \omega)\exp[i(\omega - \mathbf{q}\mathbf{v})t]. \tag{2.31}$$

Here we introduced the Fourier transform of the electric field amplitude $\mathbf{E}(\mathbf{q}, \omega)$ of a point charge moving at the constant velocity $\mathbf{v}$ in a polarized medium. From the Maxwell equations, it follows that in the nonrelativistic case $v \ll c$ (where c is the velocity of light) the amplitude $\mathbf{E}(\mathbf{q}, \omega)$ is given by the expression

$$\mathbf{E}(\mathbf{q}, \omega) = -(ie/2\pi^2)\mathbf{q}[\delta(\omega - \mathbf{q}\mathbf{v})/q^2\varepsilon(\mathbf{q}, \omega)], \tag{2.32}$$

where $\varepsilon(\mathbf{q},\omega)$ is the dielectric function depending on the wave vector $\mathbf{q}$ and the frequency ω of the disturbance. Substituting the explicit expression for the amplitude $\mathbf{E}(\mathbf{q},\omega)$ into (2.31) and performing integration over the component of the vector $\mathbf{q}$ parallel to the velocity $\mathbf{v}$ by means of the δ-function we find

$$dE/dS = (2e^2/\pi v^2)\int_0^{+\infty} d\omega \int_{q^-}^{q^+} dq \mathrm{Re}[i\omega/q\varepsilon(q,\omega)]. \tag{2.33}$$

When deriving the latter expression, the variable $q = [(\mathbf{q}-\omega\mathbf{v}/v^2) + (w/v)^2]^{1/2}$ was introduced and the integration over the azimuthal angle of the vector $\mathbf{q}$ in the plane perpendicular to the velocity $\mathbf{v}$ was performed. Besides that we took into account that the dielectric function can be presented as $\varepsilon = \varepsilon' + i\varepsilon''$, where its real part ε' is an even function of ω, while the imaginary part ε'' is an odd function of frequency. Hence, Re $i\omega/(\varepsilon'+\varepsilon'') = \omega\varepsilon''/[(\varepsilon')^2+(\varepsilon'')^2]$ is an even function of the frequency ω and the integral over the frequency from $-\infty$ to $+\infty$ is equal to the integral from 0 to $+\infty$, multiplied by the factor of two. The upper and the lower limits of integration in (2.33) over the momentum transfer q are determined from the energy conservation law and read

$$q^{\pm} = [(2mE)^{1/2} \pm (2m(E-\hbar\omega))^{1/2}]/\hbar. \tag{2.34}$$

Expressions (2.33) and (2.34) allow to assess the typical distance at which inelastic interaction accompanied by plasmon excitation takes place. This distance is about $r \sim q^{-1} \sim v/\omega_p$. Substituting into the latter relationship the plasmon frequency $\omega_p \sim e^2/a_0\hbar$ we find $r \sim a_0 v/v_0$, where a_0 and v_0 are the Bohr radius and velocity, respectively. Hence, for electrons of the energy range from 100 to 2000 eV, the excitation of plasmon oscillations occurs in a volume of space with the linear dimension of 0.1–0.7 nm. This distance is of the order or large compared to the atomic size and is consistent with the idea of long-range Coulomb forces being responsible for collective oscillations of the electron gas.

The energy losses per unit pathlength, defined by (2.33) comprises the losses in scattering events accompanied by all possible energy ($\hbar\omega$) and momentum (q) transfers. Hence the integral over the momentum transfer q is proportional to the differential probability for the probe electron to loose a certain amount of energy in an inelastic collision. This probability is often referred to as the differential inverse inelastic mean free path, or alternatively, as the macroscopic differential inelastic scattering cross section $w(E \mid \hbar\omega)$. By rewriting (2.33) in terms of the function $w(E \mid \omega)$

$$dE/ds = \int d(\hbar\omega)\hbar\omega w(E \mid \hbar\omega), \tag{2.35}$$

we obtain

$$w(E \mid \hbar\omega) = (2e^2/\pi\hbar^2 v^2)\int_{q^-}^{q^+} dq q^{-1} Im[\varepsilon(q,\omega)]. \tag{2.36}$$

The total probability to loose any amount of energy when travelling a unit pathlength can be found by integration of the function $w(E \mid \hbar\omega)$ over all energy transfers. The quantity being equal to the inverse total probability to be scattered inelastically per unit pathlength is called the *inelastic mean free path* (IMFP)

$$\lambda_i = \left[\int d\varepsilon w(E \mid \varepsilon)\right]^{-1}, \tag{2.37}$$

where ε denotes the energy transfer.

As follows from (2.38) and (2.39), the key role in evaluation of the IMFP is played by the dielectric function $\varepsilon(\mathbf{q},\omega)$. Finding a general accurate formula for this function from physically based arguments is usually difficult as the quantity $\varepsilon(\mathbf{q},\omega)$ depends on a specific behaviour of weakly bound states and is affected by exchange and correlation effects being either neglected or approximately accounted for in the linear response approach. Thus we encounter here the same problems as in the Bethe theory of inner-shell ionization (*cf.* Section 2A). One of the ways to overcome this difficulty is to use an empirical dielectric function. In particular, in the algorithm of Tanuma et al. [171] and that of Ashley [172], the experimental optical absorption data are employed to evaluate the quantity $\varepsilon(\mathbf{q},\omega)$ and to obtain numerical IMFP values. The procedure used in ref. [171] is based on the semiempirical model of Penn [165]. Penn's suggestions comprise the following basic points:

(a) It is assumed that $Im[\varepsilon(0,\omega)]^{-1} = Im[\varepsilon(\omega)]^{-1}$, where $\varepsilon(\omega)$ is the optically measured dielectric function

(b) The imaginary part of the inverse dielectric function for an arbitrary value of the momentum transfer $\mathbf{q}$ is equal to the corresponding quantity of the Lindhard dielectric function averaged over a Wigner–Seitz cell with a fictitious electron density.

Thus, the fictitious electron density is related by condition (a) to the experimentally determined $\varepsilon(\omega)$, yet not uniquely, leaving thereby much space for arbitrariness. Nonetheless, assumption (b) makes possible to: 1) account for spatial variation of the electron density in the statistic approximation [164], and 2) find the explicit dependence of the quantity ε on the momentum transfer since the analytical expression for the Lindhard dielectric function is available [149]. Making further use of the single-pole approximation for the imaginary part of the reverse Lindhard dielectric function allows to reduce the formula for the IMPF at energies higher than 200 eV to a single-integral expression [171]. In addition to points (a) and (b), the constructed dielectric function is forced to meet the sum rules [173–175]

$$\int_0^\infty Im[1/\varepsilon(0,\omega)]d\omega/\omega = -\pi/2, \tag{2.38}$$

and

$$\int_0^\infty Im[1/\varepsilon(0,\omega)]\omega d\omega = -\pi\omega_p^2/2. \quad (2.39)$$

Tanuma et al. extended their calculations of the IMFP for 27 elements [176], 15 inorganic [177] and 14 organic compounds [178] over 50–2000 eV range. Their results are in good agreement with the numerical values of IMFP obtained by other authors [172,179] at relatively high energies (> 1000 eV). However, in the energy range between 50 and 200 eV the differences among IMFP values obtained in refs. [172], [176] and [179] may reach up to 50%. Selected results of IMFP calculations from refs. [176–178] are presented in Table 2. It is seen that typical IMFP values are of the order of several nm. At $E > 200$ eV the IMFP increases with energy approximately as $\lambda_i \sim E^\alpha$, where $\alpha = 0.7 - 0.8$. This is in agreement with earlier findings reported in refs. [153,154,180–183]. It should be emphasized that although the atomic serial number dependence of λ_i is weakly pronounced the IMFP is material dependent and cannot be described by a single universal curve as a function of energy.

TABLE 2. The Inelastic Mean Free Path Values for Selected Elements [30].

E, eV	C	Al	Si	Ti	Ni	Cu	Mo	Pd	Ta	W	Au	Bi
50	5.9	3.2	4.1	4.5	4.9	5.0	5.1	4.8	4.8	5.0	6.7	4.9
100	6.4	4.2	5.3	5.1	4.6	5.0	4.5	4.1	4.5	4.1	4.8	5.5
150	7.5	5.3	6.5	6.2	5.1	5.6	5.0	5.4	5.0	4.5	4.8	6.3
200	8.8	6.3	7.8	7.3	5.7	6.2	5.6	6.2	5.5	5.0	5.1	7.2
400	13.7	10.0	12.5	11.6	8.1	9.0	8.5	9.4	8.0	7.3	7.1	10.6
600	18.4	13.3	16.6	15.6	10.4	11.4	11.3	12.5	10.4	9.4	9.1	14.0
800	22.8	16.5	20.6	19.5	12.7	13.9	14.0	15.4	12.7	11.4	11.1	17.2
1000	27.0	19.6	24.4	23.2	14.9	16.3	16.5	18.2	14.8	13.4	12.9	20.2
1200	31.1	22.6	28.2	26.8	17.0	18.7	18.9	20.9	16.9	15.2	14.8	23.2
1400	35.2	25.5	31.8	30.2	19.2	21.0	21.2	23.5	19.0	17.1	16.5	26.1
1600	39.1	28.4	35.4	33.6	21.2	23.3	23.5	26.0	21.0	18.9	18.3	28.9
1800	43.0	31.3	39.0	36.9	23.3	25.5	25.8	28.4	22.9	20.6	20.0	31.6
2000	46.8	34.1	42.5	40.2	25.3	27.7	28.0	30.9	24.9	22.4	21.6	34.4

In order to facilitate evaluation of inelastic mean free path values Tanuma et al. [176] proposed an analytical expression for λ_i , which was prompted by the Bethe equation for the ionization cross section, since the behaviour of inelastic scattering probability in solids is supposed to be approximately the same as for isolated atoms [184]. These authors modified the Bethe equation by including two additional terms in an attempt to account for exchange effects as suggested by Ashley [172] and Inokuti [185]. The resulting expression contains four parameters which may be related in an empirical way to principal quantities characterizing the electron gas in solids, *i.e.*, the Fermi and plasmon energies, atomic bulk density and number of quasifree (valence) electrons per atom. The result of Tanuma et al. reads

$$\lambda_i = E/\{E_p^2[\beta \ln(\gamma E) - (C/E) + (D/E^2)], \tag{2.40}$$

where $E = 28.8(N_\nu \rho/M)^{1/2}$ is the free-electron plasmon energy (in eV), ρ is the bulk density (in g/cm^3), N_ν is the number of valence electrons per atom or molecule and M is the atomic or molecular mass. The parameters β, γ, C and D are tabulated for 27 elements and expected to be constant over the range of energies from 50 to 2000 eV [176]. The authors of ref. [176] also proposed approximate analytical expressions for the parameters β, γ, C and D. These analytical expressions together with (2.40) constitute the so-called *predictive formula* TTP-2. In the limiting case of high energies formula (2.40) reduces to the corresponding result of the first Born approximation. In Fig. 11, the dependence of the IMFP on the energy is shown by the solid curve for a silver target. The solid curve is obtained by interpolating the results of calculations by Tanuma et al. [176] for the energy interval 10–2000 eV and making use of the modified Bethe equation [176] for the energies from 2.0 to 3.0 keV.

Experimental determination of the IMFP encounters some difficulties due to a noticeable background of elastic scattering which contributes to the overall attenuation of a signal electron current [186]. Therefore, in order to measure the quantity λ_i it is necessary to account correctly for the influence of elastic collisions (*cf.* Section 3). Here, we would like to mention recent results obtained from measuring the probability of elastic backscattering [187–197]. The elastic reflection coefficient depends on the exact shape of the differential elastic scattering cross section and the inelastic mean free path [189,198]. Jablonski [189] found from MC simulation data that the elastic backscattering probability in a large solid angle is roughly proportional to the inelastic mean free path. This provides a simple means to determine IMFP values from a routine analysis of the energy distribution of backscattered electrons in the vicinity of the elastic peak (elastic peak electron spectroscopy). Especially attractive looks the idea to employ relative elastic peak

intensities [192]. It stipulates, however, that the IMFP for some particular material (standard) be known. Lesiak et al. [192] used this method to measure the IMFP for carbon (graphite and glassy form), nickel and platinum at electron energies from 270 to 2350 eV with Al as a reference sample. The results obtained in ref. [192] for graphite are shown in Fig. 12. Here, also displayed are the experimental data [199–201] for the so-called *attenuation length* (AL) and the dependence of the IMFP on energy as predicted by Tanuma et al. [171]. The AL is expected to be very close to the corresponding IMFP in this case due to weak scattering properties of carbon (for discussion of the difference between IMFP and AL see below). Nonetheless, the Al values are seen to be less than the respective IMFPs by 20% on the average.

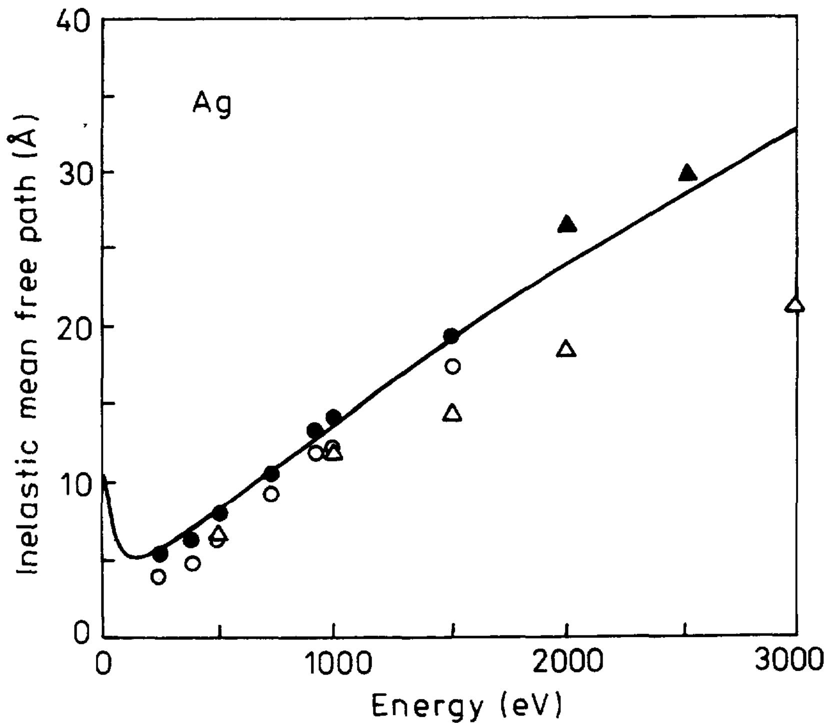

Fig. 11. The energy dependence of the inelastic mean free path for silver. Solid line – calculations from the algorithm and the modified Bethe equation of Tanuma et al. [176] (*cf.* text for details). Experimental data: open triangles [193], open squares [194], black triangles [196], black and open circles – with and without the surface-excitation correction, respectively [197].

The same technique was applied to determine the IMFP in silver [193] in the energy range from 500 to 3000 eV. The energy dependence of the IMFP was found to follow the power law with the coefficient $\alpha = 0.699$. The results found in ref. [193] for the aluminium standard are about 60–70% less than those predicted by the modified Bethe equation and obtained later for the nickel reference sample [196] (*cf.* Fig. 11). The authors of ref. [196] attribute these discrepancies

to surface roughness of the aluminium sample which was sputter-cleaned and to high inelastic background accompanying the elastic peak of Al. The results of ref. [196] as well as those of Dolinski et al. [194]. compare well with the calculations based on the modified Bethe equation [176].

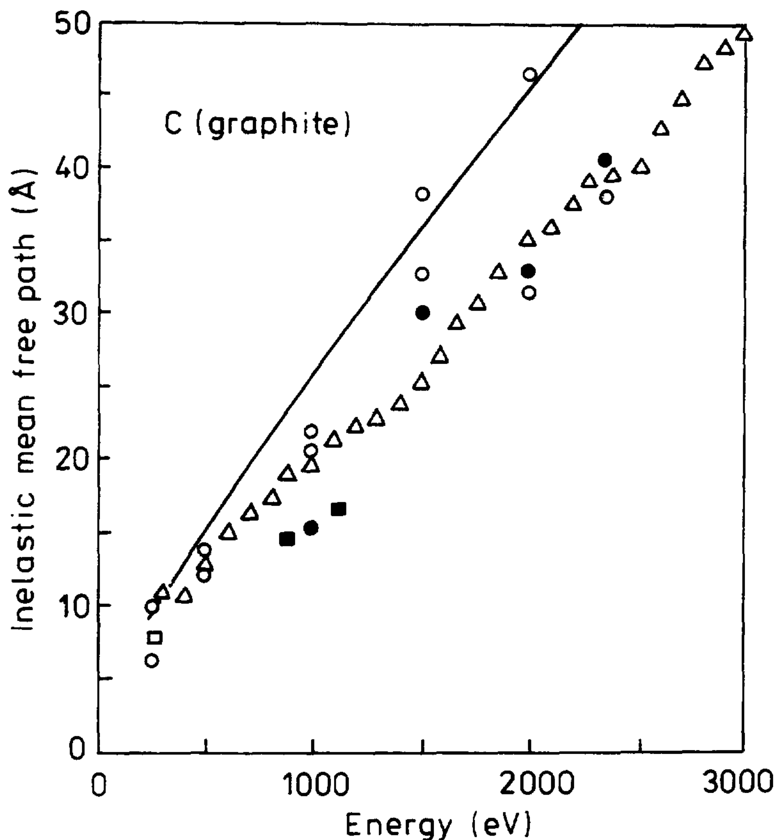

Fig. 12. The energy dependence of the inelastic mean free path for graphite. Open and filled circles are the data of ref. [192] obtained by direct integration of the elastic peak intensity and spectra decomposition, respectively. Open triangles and filled squares are the AL data of refs. [201] and [200], correspondingly. The solid curve – theoretical results of Tanuma et al. [171].

An analytical expression relating the angular distribution of elastically reflected electrons to the IMFP has been obtained recently by solving a transport equation with appropriate boundary conditions [202]. This expression can be used for converting the experimentally measured angular distributions into inelastic mean free path values. Beilschmidt et al. [195] employed the theory developed in ref. [202] to determine the IMFP for Al, Ni, Pt and Au. at the electron energies 250–1500 eV. These authors used three different standards to study the influence of a reference sample on the IMFP measured experimentally and found the IMFP for Ni, Pt and Au to be

systematically lower when the Al standard was used. On the other hand, the IMFP values of gold, obtained for Ni and Pt standards in ref. [195] (*cf.* Fig. 13) compare well with those reported by Dolinski et al. [194].

An alternative option would be to use the Monte Carlo (MC) simulation to evaluate the angular distribution of backscattered electrons for different IMFPs. A value of the quantity λ_i at which a theoretical distribution fits best to the corresponding experimental one is considered as the correct IMFP value [197].

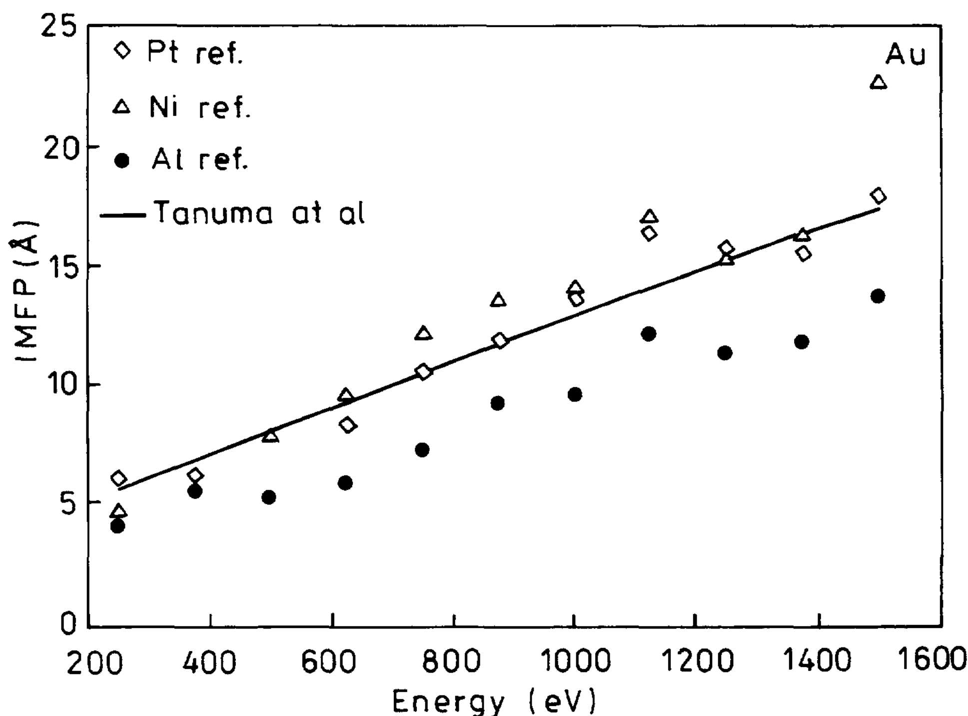

Fig. 13. The energy dependence of the IMFP in gold. The data points are the experimental results [195] evaluated for different standards: filled circles – Al, triangles – Ni and diamonds – Pt. The values of the IMFP by Tanuma et al. [171] are also shown by a solid line for comparison (after ref. [195]).

The theory of inelastic scattering presented above is valid for an infinite solid. Meanwhile, recorded signal Auger and photoelectrons, at least once, travel in the vicinity of the surface (when crossing the boundary between vacuum and a target). The polarization of a medium in the near surface region is different from that in the bulk and so is the process of inelastic energy losses. The surface effect is important at distances from the surface comparable with the electric field relaxation length, *i.e.*, at $r \sim \omega/v$ and amounting to about few Å. Recent

theoretical studies [166,167,203,204] point out the influence of the semiinfiniteness of a medium on the energy spectra of quasielastically backscattered electrons. The surface charge density induced by a moving electron creates an additional electric field, which affects the electron motion both inside and outside the target, so that the particle experience energy losses not only in the bulk, but also above the surface. Chen [197] included the surface-effect correction into the algorithm of evaluating the IMFP from experimental REELS data and found that accounting for the surface excitations decreased IMFP values. His results obtained from processing experimental data of Dolinski et al. [191] for a silver target, with and without incorporating the surface excitations are shown in Fig.11.

Concluding this section, we would like to stress that the inelastic mean free path should not be confused with the *attenuation length* (AL). The term AL was used in the past to account for a combined effect of elastic and inelastic collisions on the Auger and photoelectron line intensity and is essentially based on the idea of the exponentially decaying escape probability. The attenuation length coincides with the inelastic mean free path only in the case when elastic scattering is negligible. Generally, the escape probability of signal electrons is not described by a simple exponential law [203] and thereby the term AL becomes questionable. Nonetheless, in earlier studies, this quantity was a subject of extensive compilations [205] primarily due to numerous data available from overlayer experiments. A meaningful quantification of experimental results of overlayer measurements implies knowledge of the depth distribution function (DDF) [205] for an overlayer-substrate target. The analytical expression for this function has been found only recently [205] (*cf.* Section 3). In addition, surface-excitations effect in the case of overlayer-substrate target may be even more important than for a uniform sample.

3. Multiple Scattering of Signal Electrons in Solids

A. Medium energy electron-solid interaction

In practical AES/XPS analysis electrons of medium energies are commonly used. The corresponding energy range strictly speaking is defined by the inequalities

$$e^2/a_0 \ll E \leq (Ze^2)/a_0. \tag{3.1}$$

Energy range (3.1) is remarkable for the most effective excitation of characteristic x-rays and Auger electrons under electron bombardment [21,208] and the highest values of inelastic reflection

coefficients of electrons from solids [209]. From (3.1), it follows that the electron kinetic energy E is assumed to be large compared with the binding energies of outer shell or valence atomic electrons. On the other hand the right-hand side condition (3.1) implies that the quantity E is less or of the same order of magnitude as the absolute value of the binding energy of the most tightly bound K-shell electrons. In average this energy interval extends from few hundreds eV to several tens of keV depending on the atomic Z-number.

A medium energy electron moving in a solid suffers intensive multiple scattering. If the medium is amorphous the interaction with scattering centers is incoherent and splits into elastic and inelastic scattering. Scattering events leading to excitation of target electrons are called inelastic. They result from atom excitation and ionization by electron impact or interaction with a gas of conduction band electrons. Correspondingly, processes that are not accompanied by electron excitation are referred to as elastic ones. The elastic processes in random solids are due to elastic collisions of electrons with individual atoms.

In crystalline targets a periodic arrangement of atoms gives rise to diffraction effects. These effects are called coherent scattering or dynamical diffraction. In real crystals coherent scattering of electrons always takes place against the background of incoherent effects owing to thermal displacements of atoms from their equilibrium positions, lattice defects and energy dissipation in collisions with quasifree conduction electrons.

The interaction of a probe electron with a solid is caused, primarily by Coulomb forces and is described by the potential [210]

$$U(r) = -\sum_a Ze^2 \mid \mathbf{r} - \mathbf{R}_a - \mathbf{u}_a \mid^{-1} + \sum_{a,b} e^2 \mid \mathbf{r} - \mathbf{R}_a - \mathbf{u}_a - \rho_{a,b} \mid^{-1} + \sum_c e^2 \mid \mathbf{r} - \rho_c \mid^{-1} \qquad (3.2)$$

containing the three terms. In (3.2), $\mathbf{R}_a$ is the equilibrium position of the atom and $\mathbf{u}_a$ is its thermal displacement. In the first term the summation is performed over all atoms. The second and the third terms describe the interaction with bound atomic and conduction band electrons, respectively. Here $\rho_{a,b}$ is the radius-vector of electron b belonging to atom a in the system associated with the instantaneous position of atom a, while ρ_c describes the position of a quasifree electron. In insulators and semiconductors, the last term in (3.2) is usually negligible. It should be emphasized that potential (3.2) is, in fact, a multiple-particle potential and the electron positions $\rho_{a,b}$ and ρ_c , generally speaking, depend on the coordinates of a probe electron r.

It is advisable to start with the general case of a crystalline target since an amorphous sample may be treated as a limiting case of large thermal displacements of atoms from their equilibrium positions. Let us introduce the average potential value over the thermal displacements $< U(\mathbf{r}) >$,

assuming also that the quantity $< U(\mathbf{r}) >$ pertains to a figurative situation, when the states of target electrons are not affected by the presence of a probe particle. In other words, when calculating the average potential it is believed that the polarization of the medium and excitation of electrons by the incoming electron can be neglected. Then, in an ideal crystalline system without energy dissipation and with zero thermal displacements, the potential $U(\mathbf{r})$ coincides with its average value $U(\mathbf{r}) =< U(\mathbf{r}) >$. The average potential $< U(\mathbf{r}) >$ is periodic and leads only to Bragg diffraction. It does not cause any incoherent scattering. The motion of electrons in the potential $< U(\mathbf{r}) >$ is described by Bloch type wave functions while coherent states are represented by the Bloch waves propagating in the directions determined by reciprocal lattice vectors.

In reality, thermal motion of atoms exists even at zero temperature and there is always a response of solid electrons to the presence of a charged particle. Therefore, the real potential U deviates from its average value by the quantity $\delta U = U(\mathbf{r}) - < U(\mathbf{r}) >$. As a result, in crystalline targets incoherent scattering occurs. For instance, in the case of an amorphous material the average value $< U(\mathbf{r}) >= 0$ and the potential deviation, δU, equals the potential itself, $\delta U = U$.

Incoherent scattering comprises deflection of electrons at arbitrary angles and dissipation of their kinetic energy. The elastic scattering is mainly responsible for changing the direction of the electron motion or momentum relaxation. The reason is that the absolute value of the amplitude for scattering at angle $\vartheta \sim 1$ in a screened Coulomb field of a nucleus of the charge $Z \gg 1$ is much greater then the corresponding absolute value of the sum of amplitudes due to collisions with atomic electrons [36]. In addition, deflections in elastic collisions are characterized, as a rule, by much larger scattering angle values. Indeed, making use of simple classical assessments, we find that the typical scattering angle in an elastic collision is

$$\vartheta \sim \Delta p_{\perp}/p \sim U(a)/E \geq Z^{-1/3}, \tag{3.3}$$

where p and $\Delta p_{\perp}$ are the electron momentum and the momentum change in the direction perpendicular to the electron motion, correspondingly, $U(a)$ is the absolute value of electron-atom potential energy of interaction at a distance being equal to the Thomas–Fermi screening radius $a \sim a_0 Z^{-1/3}$. Employing similar considerations one can show that in an inelastic scattering event

$$\vartheta \sim (e^2/a_0)/E \ll 1 \tag{3.4}$$

and, thereby, is usually small compared with the typical scattering angle in an elastic collision. Thus, the momentum relaxation process is governed mainly by multiple elastic scattering.

Contrary to this, the energy dissipation is determined primarily by inelastic interaction. Estimating the typical energy loss in elastic collisions it is easy to show that it is proportional to the ratio of the electron (m) and the atom (M) masses

$$\Delta E \sim (m/M)e^2/a_0. \tag{3.5}$$

Since $m/M \sim 10^{-3} - 10^{-4}$ the right-hand side of (3.5) is almost negligible as compared with the energy loss in inelastic scattering event. The latter quantity can be put of the order of a binding energy of weakly bound outer shell electrons in insulators and semiconductors or the Fermi energy in metals, so that we have

$$\Delta E \sim e^2/a_0. \tag{3.6}$$

Note that the energy loss in an individual inelastic collision still remains small compared to the electron kinetic energy E. From these assessments it follows that the incoherent interaction of medium energy electrons with solids is accompanied by intensive elastic scattering and slow energy dissipation in inelastic collisions.

Coming back to the case of crystalline target we conclude that the physical picture of medium energy electron-solid interaction is rather complicated. Incoherent scattering decreases the Bloch-wave intensities and eventually randomizes the electron distribution in space, which is a typical relaxation process being irreversible in time. The probe electron may be regarded as an open system in continuous contact with its surroundings, exchanging energy, momentum, polarization and so forth [211]. Being initially in the nonequilibrium state, the electron will at some time later go over into an equilibrium state determined by the external conditions, such as, solid scattering properties, temperature and others. The most general way to describe the evolution of the electron-solid system in space and time consists in finding the density operator [210,211]

$$\hat{\rho} = \sum_{n,m} W_{n,m} \mid \psi_n >< \psi_m \mid, \tag{3.7}$$

where the sum extends over all states present, $\mid \psi_n >$ is a column vector corresponding to a certain wave function j of the system, while $< \psi_m \mid$ is the adjoint row vector. The coefficient W_{nn} represent the probability to find our system in the nth state. The density matrix of the electron-solid system contains enormous amount of information which, in practice, is not necessary. Besides that a task of calculating the total density matrix would be hopeless owing to the huge number of degrees of freedom of the system. Meanwhile, a researcher is interested in obtaining the reduced density matrix $\rho_e(t) = \mathrm{Tr}_s \rho(t)$ pertaining to the probe electron and depending only on the electron coordinates (here the sign Tr_s means taking the trace or summing over all the variables of the

solid). Fortunately, it is possible to derive a kinetic equation governing the behaviour of the electron density matrix, by making use of the Fano assumptions and the Liouville equation for the quantity ρ [211]. The first of the Fano assumptions implies that the solid has so many degrees of freedom that the effects of interaction with the electron dissipates away quickly and do not react back on to the particle to any significant extent. Thus the correlation between the electron and the solid, induced by the interaction, is assumed to be small and may be treated on the basis of a perturbation approach. The second assumption stipulates that the electron lose its memory of the past events and the derivative of the density matrix $\partial\rho_e/\partial t$ depends only on the function $\rho(t)$ itself at time t. The latter approximation is of fundamental importance since it allows to go over from quantum mechanical equations reversible in time to a an entirely new type of equation – a quantum kinetic equation describing irreversible processes of momentum and energy relaxation.

During the last decade the quantum kinetic equation formalism has been successfully applied to a number of problems involving diffraction of relatively fast ($E \sim Ze^2/a_0$) electrons in crystals [212–218]. In particular, a solution to the kinetic equation for the spectral density matrix was used for quantitative evaluation of the inelastically-scattered-electron contribution to the diffraction pattern in the transmission geometry [213–216]. Dudarev et al [217] studied dynamical electron diffraction from partially disordered growing surfaces. A theory of electron backscattering from crystalline targets has been proposed in ref. [218].

However, as regards the medium energy range some questions still remain to be solved. For example, an analytical theory of Auger and photoelectron diffraction, enabling to describe signal electron emission from crystals in terms of simple physical parameters is still to be developed. In the special case of a random solid the quantum kinetic equation is shown to reduce to a transport equation [210]. The major advantage of the transport equation is that it involves only the single particle distribution function representing the diagonal elements of the reduced matrix ρ_e. This decreases greatly the number of physical quantities to be determined when describing electron-solid interaction. Such a simplification is achieved at the price of losing information of a purely quantal character. Nonetheless, an analytical solution to the linearized Boltzmann equation allows to obtain many important characteristics of Auger and photoelectron emission. In the next section this approach is considered in detail.

B. Transport equation approach

The transport equation represents by definition a linearized Boltzmann kinetic equation writ-

ten in terms of a single particle distribution function [219]. From a quantal point of view the single particle distribution function is equal to the corresponding diagonal element of the density matrix. This function may be obtained classically from a multiple particle distribution for a system of a large number of particles upon integration over the coordinates of all the particles but the one under consideration. Both the density matrix and the multiple particle distribution function obey the equations describing reversible processes. Those are the quantal equations of Schrödinger and Liouville and classical Newton equations of motion, respectively. In order to employ these quantities for describing relaxation phenomena a number of assumptions have to be made. In the literature, the criteria of applicability of the transport equation are not always paid sufficient attention to. Therefore, this question is considered in more detail below to identify clearly a class of problems to which the transport equation may be applied.

The possibility of derivation of the transport equation from the classical equations of motion for the multiple particle distribution function is based on the *correlation relaxation principle* formulated by Bogolubov [220]. The principle states that correlations can be neglected if the correlation radius r_c is small compared to the total mean free path of a particle in matter λ_t. The quantity r_c is defined as a typical distance between any of two particles of the system at which the correlation among their positions and velocities still takes place. In random solids the correlation radius is of the order of the maximum value of the particle wave length λ and the effective radius of interaction r_0. Hence, we come to the inequality [211]

$$\lambda_t \gg \max\{\lambda, r_0\}. \tag{3.8}$$

In the case of medium energy electrons the effective radius of elastic scattering, r_{0e}, is about the Thomas–Fermi screening radius $a \sim a_0 Z^{-1/3}$. The corresponding quantity for the inelastic interaction is of the order $r_{0i} \sim a_0 v_0/v$, where v and v_0 are the electron and the Bohr velocities, respectively. The latter estimate is obtained assuming the direct Coulomb interaction between the incoming and weakly bound electrons. The total mean free path is typically of the order of several nm while the electron wave length and the effective radii of elastic and inelastic interaction do not exceed, as a rule, the Bohr radius $a_0 \sim 0.05$ nm. Hence, condition (3.8) is well fulfilled in the energy range relevant for AES/XPS, which in turn allows to apply the concept of a single-particle distribution function, when describing medium energy electron transport in solids.

Accounting for elastic scattering in the transport equation very often implies making use of the binary encounter approximation, which stipulates that triple and higher-order collisions of the probe electron with atoms are neglected. The binary encounter approximation is satisfied

under the condition

$$d \gg \max\{\lambda, r_0\}, \tag{3.9}$$

which means physically that the volume occupied by a single atom in a solid exceeds greatly the volumes characterizing the electron interaction and its localization in space. In this connection one should mention that resonance processes characterized by a large absolute value of interaction amplitude f are usually excluded from consideration. Indeed, the wave function of the electron may change significantly in a volume of the order of f^3. If this volume is large enough to contain several atoms or other scattering centers the assumption of the binary encounter approximation is no longer valid. So, the necessary requirement is that the quantity f^3 be small compared with a typical volume occupied by a single atom. As a result, we arrive at the additional condition

$$\lambda_t \gg f \tag{3.10}$$

implying that the total mean free path exceeds greatly the scattering amplitude.

Taking into account the main features of medium energy electron interaction with solids (*cf.* Section 3A), we write the steady-state transport equation in the form [219]

$$\begin{aligned}\mu \partial N/\partial z &= -(N/\lambda_t) + (1/4\pi\lambda_e)\int I(\Omega, \Omega', E) N(z, \Omega', E)\, d\Omega' \\ &\quad + (1/\lambda_i)\int w(E+\varepsilon \mid \varepsilon) N(z, \Omega, E+\varepsilon)\, d\varepsilon + S(z, \Omega, E),\end{aligned} \tag{3.11}$$

where $\mu = \cos\vartheta$ is the cosine of the polar angle counted from the z-axis directed towards the bulk of the target, λ_e and $\lambda_t = \lambda_e\lambda_i(\lambda_e+\lambda_i)^{-1}$ are the elastic and the total mean free paths, Ω is the unit vector along the electron velocity, $N(z, \Omega, E)$ is the flux density of electrons moving at the depth z in the direction Ω with the energy E and equals the product of the electron velocity and the single particle distribution function, $I(\Omega, \Omega', E)$ is the scattering function or the differential elastic scattering cross section normalized to unity, the function $w(E \mid \varepsilon)$ is the normalized differential inverse inelastic mean free path and describes the probability for an electron of the energy E to lose the energy ε in an individual inelastic scattering event. The source function $S(z, \Omega, E)$ in the right-hand side of (3.11) is proportional to the number of electrons produced in a unit volume of the target per unit time at the depth z, and moving in the direction Ω with the energy E.

Note that the energy losses in elastic and angular deflections in inelastic collisions are neglected when deriving (3.11), in accordance with inequalities (3.4) and (3.5). Equation (3.11) should be supplemented by the boundary condition implying that no secondaries enter the target

$$N(z, \Omega, E) = 0, \quad \text{for} \quad \mu = (\mathbf{n}_z \cdot \Omega) > 0, \tag{3.12}$$

$\mathbf{n}_z$ being the unit vector along the z-axis and it is assumed that the target occupies the right half-space so that the sample surface coincides with the xy-plane.

Equation (3.11) with boundary condition (3.12) still remains complicated to apply any of existing methods of analytical solutions. One of the major obstacles is the energy dependence of the mean free paths. The secondary electrons may escape from different depths and change significantly their kinetic energy as they move towards the surface. Another problem which frequently arises is the necessity to satisfy the exact boundary condition. If the energy dependence of the differential scattering cross sections can be disregarded one comes to the one-speed boundary value problem. The latter can be, in principle, solved by employing Case's method of eigenfunctions [219,221–223]. However, even in this case the procedure of finding the exact solution to the transport equation is rather cumbersome. It consists of expanding the differential elastic scattering into a series on Legendre polynomials, solving the characteristic equation to find eigenvalues and constructing a fundamental set of the transport equation solutions [3]. To overcome these difficulties it is often necessary to resort to some additional simplifying assumptions.

In AES/XPS quantitative analysis usually only a narrow part of the energy spectrum in the vicinity of the characteristic peak is of interest. This part of the energy distribution corresponds to the so-called *quasi-elastically scattered* electrons whose energy loss $\Delta E \sim (e^2/a_0)$ remains small compared with the initial kinetic energy E. This makes possible to ignore the energy dependence of coefficients entering the transport equation or to account for this dependence in an approximate way [208]. Thus, one may put

$$I(\Omega, \Omega', E) \sim I(\Omega, \Omega', E_0); \quad w(E + \varepsilon \mid \varepsilon) \sim w(E_0 \mid \varepsilon), \tag{3.13}$$

where E_0 is the initial kinetic energy of signal electrons.

It turns out that the boundary value problem may be simplified furthermore, by making use of the generalized radiative field similarity principle [208], which states that the exact differential elastic scattering cross section in the kinetic equation may be replaced by an approximate one if, a number of conditions are fulfilled, *viz.*, [208,224]:

(a) The typical angular distribution of particles in matter is a smooth function of the angular variable so that $N \sim \mid \nabla_\Omega N \mid$, where ∇_Ω denotes the gradient operator with respect to the Ω-variable,

(b) In the limiting case of weak scattering ($\lambda_i \ll \lambda_{tr}$) an approximate solution is required to reduce to the result found in the straight line approximation,

(c) In the opposite limiting case of strong scattering and weak absorption ($\lambda_i \gg \lambda_{tr}$) the similarity

relationship

$$\lambda_t \nu_0 = \lambda_t' \nu_0' \tag{3.14}$$

is supposed to be satisfied. In (3.14), ν_0 and ν_0' are the largest eigenvalues of the exact and approximate transport equations, respectively, while λ_t and λ_t' represent the exact and approximate total mean free paths. The eigenvalues of the transport equation can be obtained from the solution of the characteristic continued fraction equation [225]

$$1 - \omega = \cfrac{k}{3 - \omega b_1 - \cfrac{k}{5 - \omega b_2 - \cfrac{k}{7 - \omega b_3 - \dots}}}, \qquad k = \nu^{-2} \tag{3.15}$$

ω being the single scattering albedo

$$\omega = \lambda_i (\lambda_i + \lambda_e)^{-1} \tag{3.16}$$

and b_n is the n-th coefficient in the Legendre polynomial expansion of the scattering function.

Assumption (a) implies that specific features of small-angle multiple scattering do not influence significantly the electron transport in a solid as the angular distribution is too broad for these effects to be noticeable. It should be noted that, if the transport mean free path is small compared with the inelastic one, $\lambda_{tr} \ll \lambda_i$, quick randomization of particles over directions of motion takes place before a considerable fraction of electrons suffers the first inelastic scattering event. Therefore, in the case of weak absorption, the first requirement may be removed. The third condition of the similarity principle is prompted by the fact in the diffusion-like regime of motion at large distances from a source ($r \gg \lambda_t$) the exact and approximate solutions of the kinetic equation decay exponentially according to the law [219,225] $N(z,\Omega) \sim \exp(-z/\lambda_t \nu_0) M(\Omega), N'(z,\Omega) \sim \exp(-z/\lambda_t' \nu_0') M'(\Omega)$. The functions $M(\Omega)$ and $M'(\Omega)$ depend very weakly of the actual properties of the corresponding differential elastic scattering cross sections. Consequently, condition (c) provides a similarity of the exact and approximate solutions at least at large distances from a source in the case of intensive scattering. On the other hand, combination of points (b) and (c) stipulates that this similarity holds true also in the opposite limiting case of strong absorption.

The similarity of different solutions satisfying relationship (3.14) in the nearly conservative scattering medium has been known in the radiative transfer theory for a long time. The generalized radiative field similarity principle implies much more powerful statement: the similarity is possible also in the intermediate case of scattering parameter $\chi = \lambda_i / \lambda_{tr} \sim 1$. In the present form, the generalized similarity principle is a certain kind of hypothesis. The accuracy of its predictions is not so easy to assess *a priori* for an arbitrary relationship between the transport

and inelastic mean free paths. At this stage it is worth stressing that an infinite number of approximate differential scattering cross sections meet the requirements imposed by the principle. A verification of the similarity principle predictions may be performed by a direct comparison of an approximate solution with an exact one. This programme has not been fulfilled so far, due to mathematical difficulties mentioned above. An alternative way is to compare analytical results with those found by a Monte Carlo simulation method employing basically the same physical assumptions as the classical radiative transfer theory. For this purpose especially valuable would be a relatively simple approximate differential elastic scattering cross section which allows to solve the boundary value problem analytically. It can be proved that one of the effective cross sections of this kind is the transport cross section. It means mathematically that the scattering function $I(\Omega, \Omega')$ is changed to unity while the elastic mean free path is replaced by the transport mean free path. The latter procedure constitutes the so-called *transport approximation* (TA) [145,208]. The transport approximation as applied to the electron scattering in solids implies far-reaching physical consequences. Before discussing them we would like to present in brief the corresponding mathematical formulation of the secondary emission problem.

The most general way to solve a boundary value problem is to express the solution via the relevant Green's function. The Green's function satisfies the transport equation with a non-uniform term describing a unidirectional point source emitting electrons of a fixed energy. Thus, the source distribution in this case becomes proportional to a product of δ-functions with respect to all variables involved. Taking into account assumption (3.13), we find the kinetic equation for the Green's function written in the transport approximation:

$$\mu \partial G/\partial z = -G/\lambda_t^* + (1/4\pi\lambda_{tr}) \int G(z, \Omega', E) d\Omega' + \delta(\Omega - \Omega_0)\delta(z - z_0)\delta(E - E_0), \qquad (3.17)$$

where $\lambda_t^* = \lambda_i \lambda_{tr} (\lambda_i + \lambda_{tr})^{-1}$ is the total mean free path in the TA. The Green's function $G = G(z, \Omega, E \mid z_0, \Omega_0, E_0)$ is assumed to meet the same boundary condition as the flux density N. Therefore, a solution to the kinetic equation for any arbitrary source function can be presented by

$$N(z, \Omega, E) = \int G(z, \Omega, E \mid z_0, \Omega_0, E_0) S(z_0, \Omega_0, E_0)\, dz_0\, d\Omega_0\, dE_0. \qquad (3.18)$$

Equation (3.17) differs from (3.11) by a simpler form of the elastic-collision integral, *i.e.*, the second term in the right-hand side. The other point to be stressed is attenuation of electrons is now determined by the effective total mean free path λ^* rather than by the usual mean free path λ_t.

Note also that in the medium energy range the contribution of small scattering angles $\vartheta \sim$

$(dk)^{-1} \ll 1$ to the transport cross section is negligible (here d is the average interatomic distance and $k = p/\hbar$ is the electron momentum in units of the Planck constant $\hbar$). Hence the influence of the behaviour of the electron-single atom potential at distances $r \sim d$ becomes insignificant. Since in solids the electron-atom potential at large distances is known poorly the latter conclusion is of practical importance. It allows to use in analytical as well as Monte Carlo calculations the atomic potentials evaluated for single atoms and the corresponding differential elastic scattering cross sections [226].

C. Monte Carlo simulation method

The linear transport theory discussed in the previous section is aimed at finding the probability for a particle being initially at a certain point of phase space to go to some other point in a certain period of time. It is worth emphasizing that nothing specific can be said about the trajectory of the particle. Although a considerable progress has been made in the analytical description of the electron transport in the last decade analytic solutions are not always available in situations with complex boundary conditions, *i.e.*, layered or pattern structures, and an arbitrary dependence of the differential scattering cross sections on energy and scattering angle. This difficulty may be overcome by a numerical solution of the kinetic equation. An alternative way to determine the transition probability is to use a MC technique [227] which became so popular in modelling particle transport in random and polycrystalline solids.

As in each other method, the MC simulation technique has its advantages and weak points. The MC approach is especially effective when handling with complex boundary conditions and multiple-speed transport problems. On the other hand, it is difficult to draw general conclusions about the influence of certain physical parameters on the emission characteristics obtained by MC simulation. In the present connection of particle transport in matter, the MC method consists in generating a large set of particle trajectories obeying physical laws which govern particle-solid interaction. A physically meaningful quantity is then obtained as its average value over this large set of realistic trajectories. Each separate trajectory is thereby of no physical significance and, in essence, the MC technique is very close to the main idea of the transport equation. In a broad sense, however, the MC method represents a very general approach being applied to various fields of science. Mathematically speaking, this technique may be conceived as a method to evaluate multi-dimensional integrals. If it is not known in advance which region of integration provides the main contribution to the outcome then statistical sampling of the integrand may prove quite

effective.

Another drawback of the MC approach as applied to particle transport is the necessity to generate a considerable number of trajectories in order to accumulate a required statistical accuracy of results. This is a problem, in particular, when calculating the angular distribution of photoelectrons for geometries without azimuthal symmetry. In the latter case, the opening angle of a model analyser is to be chosen sufficiently small to obtain meaningful data, which, in turn, leads sometimes to excessively great computational efforts. Therefore, it is important to identify regions in the generated set of trajectories that provide the main gain to the outcome and to restrict, if possible, the calculation to such a subset of trajectories.

The earliest applications of MC simulations to electron-solid interaction were in the field of EPMA. Electron backscattering, x-ray production by fast electrons and emission of true secondary electrons were studied by several authors [228–230]. Due to limited computer capabilities of that period, these investigations combined elements of multiple scattering theory and the MC simulation. As faster computing facilities became available the direct simulation code was proposed by Reimer [231,232], in which individual elastic collisions were modelled. This author also showed that employing The Mott differential elastic scattering cross section [127] provided a much more realistic description of medium energy electron transport as compared to the screened Rutherford cross section used earlier. As regards the inelastic interaction the starting points were the Bethe expression for the stopping power [233] and the continuous slowing down approximation. In recent years, the approach based on the dielectric function [234–237] is more often used as it allows one to study details of characteristic energy losses in the range down to several ten eV. At present a routine MC simulation programme comprises modules for calculating (i) a Mott differential elastic scattering cross section, (ii) an energy-loss function from the linear response theory and (iii) an inner shell ionization cross section by means of formulas proposed in ref. [24,37–39]. Points (i) and (ii) allow one to describe accurately small and large energy losses, respectively In the last decade, apart from applications to signal electron transport, such kind of programs were used to study electron reflection [238] and a backscattering factor in AES [239].

The hard core of a MC program is a module to generate random numbers which then are used to obtain stochastic values of steplengths between successive collisions, deflection angles and energy losses. Once the latter quantities are known the particle position and velocity can be updated, and by repeating this procedure, an entire trajectory can be modelled. Let us denote by Q a stochastic value of a given parameter q and suppose that a probability to find a system in the infinitesimally small interval $(q, q + dq)$ is equal to $G(q)dq$, where $G(q)$ is the probability

density, normalized to unity

$$\int_{q_1}^{q_2} G(q)dq = 1, \tag{3.19}$$

q_1 and q_2 being the lower and upper limits of variation of the quantity q. Thus, the function

$$\Gamma(Q) = \int_{q_1}^{Q} G(q)dq \tag{3.20}$$

represent the probability to find a system with the parameter q between q_1 and Q. Since Q is a random variable the values of the function $\Gamma(Q)$ are randomly distributed in the range [0,1] under the condition that q-values obey the distribution $G(q)$. Therefore, a value Q can be generated by inversion of the relationship $S = \Gamma(Q)$, where S is a stochastic variable from the interval [0,1], *i.e.*, $Q = \Gamma^{-1}(S)$. Consider a simple example when the parameter q is a steplength between two collisions. Assuming that the steplength R follows the Poisson stochastic process we find $G(R) = \exp(-R/\lambda)$ and $R = -\lambda \ln S$, λ being the mean free path. Generation of the deflection angles and energy losses is performed numerically for corresponding cross sections for elastic and inelastic interactions.

Most of the programming languages (*e.g.* Pascal, FORTRAN) provide routines to generate uniformly distributed random numbers. The usual algorithm is based on the simple formula

$$Q_{i+1} = aQ_i + b - mc, \qquad (0 \leq Q_{i+1} < c). \tag{3.21}$$

Here Q_i is a random number, while a, b and c are suitably selected constants. Note that m is an integer such that the quantity $Q_{i+1} < c$. By making use of the notation from the theory of numbers (3.21) can be rewritten as

$$Q_{i+1} = aQ_i + b(\operatorname{mod} m). \tag{3.22}$$

The sequence of numbers Q_1 has a period not exceeding m. In addition, there may be sequential correlations, *i.e.*, a dependence of a probability for a given number Q_i to appear on the sequence of numbers generated earlier. These problems can be avoided by mixing (shuffling) the generated sequence of pseudo-random numbers. Press et al. [240] recommend several subroutines for this purpose. Finally, one should also avoid using low-order (least-significant) decimals of the generated numbers.

The major achievements of the MC method in AES/XPS are confined basically to realistic estimates of elastic scattering of signal electrons and various emission characteristics, which are strongly influenced by this effect and are not readily assessable from simple considerations. Among

those characteristics there are the angular and energy distribution in the vicinity of the peak [241,242], the depth distribution function [243,244], the mean escape depth [245] and so on.

Recently, a number of methods have been proposed to increase significantly the efficiency of MC calculations. We note here the *trajectory reversal algorithm* by Gries and Werner [246–248], which was later combined with the statistical weights method by Cumpson [249] and the trajectory transformation approach developed by Alkemade [250,251]. The algorithm proposed in ref. [246–248] differs from the usual direct simulation method in considering an inverse problem. In the conventional method, a trajectory is modelled in the order the relevant physical processes happen: first random values of the generation depth and electron emission direction from atom are obtained. The fate of a particle is then traced until the electron leaves a solid or its pathlength becomes so large that a negligible contribution to a recorded signal is expected. It is clear in advance that a huge number of trajectories are generated in vain, *i.e.*, those pertaining to electrons either absorbed in the target or escaping in wrong directions with respect to the acceptance solid angle of an analyser. This difficulty is overcome by applying the reciprocity theorem [219]. The reciprocity theorem follows from the symmetry properties of the one-speed transport equation and thereby suits perfectly to solving a quasielastic scattering problem. The reciprocity relationships [219] establish a link between the different Green's functions of the kinetic equation in particular, between the Green's functions for the albedo and true secondary emission problems. Consider, for instance, a source at the depth τ_0 emitting electrons in the direction μ_0 , where μ_0 is the cosine of the polar emission angle. Suppose further that the probability for an electron to reach the surface and escape from the target is equal to $G(\tau = 0, -\mu \mid \tau_0, \mu_0)$. Then reciprocity theorem states that

$$G(\tau_0, \mu_0 \mid \tau = 0, \mu) = G(\tau = 0, -\mu \mid \tau_0, \mu_0)/ \mid m \mid, \tag{3.23}$$

where $G(\tau_0, \mu_0 \mid \tau = 0, \mu)$ is the transition probability for an electron emitted by a surface source in the direction μ to come to the point τ_0 in the direction μ_0. Obviously, the Green's function $G(\tau_0, \mu_0 \mid \tau = 0, \mu)$ corresponds to the albedo problem and therefore instead of describing a true secondary emission process it is sufficient to consider penetration of a beam of incident electrons through matter (*cf.* Fig. 14). As applied to the Monte Carlo procedure that means that an electron trajectory is generated in the reverse order: an electron starts at the surface with the momentum directed towards the bulk of the target as though it were emitted from the analyser. The particle is subsequently traced to a certain point inside the solid and all the trajectories ending at this point are recorded as contributing to the signal line intensity. This consideration is true under the assumption that the MC simulation is equivalent, in statistical sense, to solution

of the transport equation with an appropriate boundary condition. The question whether it is possible to prove an analogon of the reciprocity theorem in the MC procedure without resorting to kinetic equation properties still remains open. Werner et al. [252] compared the angular distributions of signal electrons emitted from different materials, obtained by direct and reverse simulation methods, and found no disagreement between the conventional and trajectory reversal algorithms. Some comments should be made on the term trajectory reversal. In fact, this term is not correct from a physical point of view since both the transport equation and the MC method describe irreversible processes of energy and momentum relaxation and, thereby, a trajectory cannot be meaningfully reversed. It is only the value of a physical quantity averaged over a large number of trajectories which matters eventually. On the other hand, the term trajectory reversal may be sometimes convenient as it is indicates how actually the calculations are carried out.

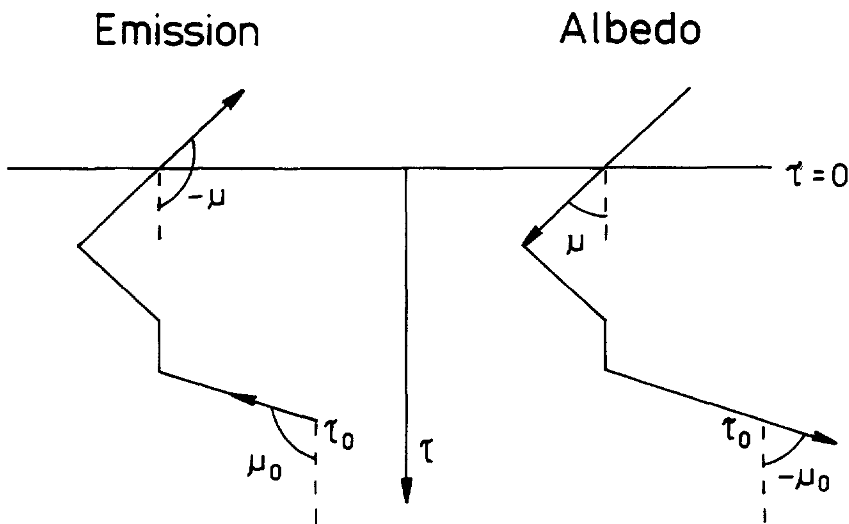

Fig. 14. Illustration of the reciprocity theorem for one-speed electron transport applied to the emission problem (see text) after ref. [252]).

The method of statistical weights was first applied by Jablonski [253]. Instead of explicitly modelling energy losses a weight factor p_0 is assigned to the trajectory contributing to signal intensity. For an electron travelled in the solid a pathlength R without suffering an inelastic collision this factor is $p_0 = \exp(-R/\lambda_i)$. Similarly, the probability that an electron is scattered n times inelastically along the pathlength R obeys the Poisson distribution

$$p_n = (R/\lambda_i)^n \exp(-R/\lambda_i)/n!. \tag{3.24}$$

Thus, the amount of particles suffered n inelastic scattering events can be calculated. Equation (3.24) is valid for an energy-independent inelastic mean free path. Meanwhile, in reality, the quantity λ_i depends noticeably on energy, $\lambda_i \sim E^{0.7}$. Therefore, one must be cautious when applying (3.24) to multiple-speed problems. The method of statistical weights was employed to account for asymmetry of photoelectron emission [244] and to study a depth dependent emission characteristics [249].

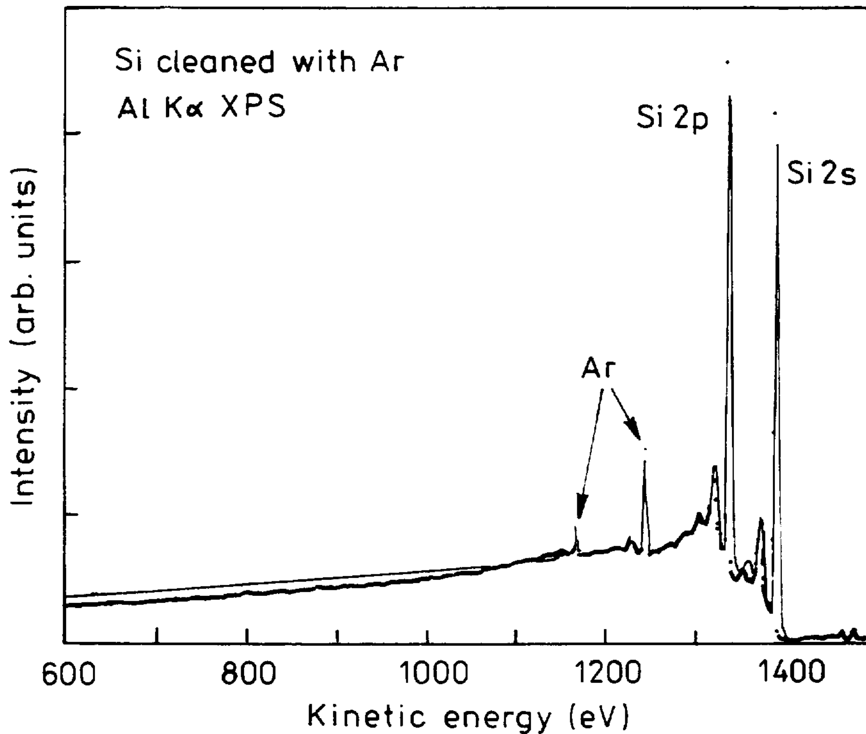

Fig. 15. Experimental XPS spectrum of an Ar sputter-cleaned Si target [261] irradiated by Al $K\alpha$ x-rays (data-points) compared with the results of MC calculations by the algorithm described in the text.

In the trajectory transformation method [250,251], each trajectory starts initially at the point of origin and a solid is assumed to be infinite. For all scattering events the electron positions and energies are stored in an array. The basic idea of the method consists in shifting the simulated trajectory at a certain distance to obtain quickly a new trajectory and, thereby, to save considerable computational time. Similarly, orthogonal transformations (rotations and reflections) of trajectories are also used to rapidly generate new sets of data. In the next step, a fictitious

plane representing a boundary is introduced and all electrons crossing this plane are considered as leaving the sample. It should be stressed, however, that a set of trajectories generated in an infinite medium is not identical to that for a semi-infinite target. The method of trajectory transformation seems to be justified for the case of relatively weak elastic scattering when multiple crossing of the fictitious plane by signal electrons are highly improbable.

As an example of implementation of a high-speed MC algorithm one can mention the software packet QUEST (Quantitation of Electron Spectroscopic Techniques) developed by Werner [254]. This algorithm employs the subprogram of Yates [255] to calculate a Mott differential elastic scattering cross section and Penn's approach [234,256] to evaluate a differential inverse inelastic mean free path. In the latter procedure, a quadratic dispersion relation is assumed and the optical data needed are taken from refs. [257,258]. The IMFP obtained in this way matches the values of Tanuma et al. [171] within few percent. The data on photoionization cross sections and asymmetry parameters employed in QUEST are those from ref. [259] and [260], respectively.

In Fig. 15, a comparison of an experimental XPS spectrum of Si excited by Al $K\alpha$-radiation [261] with that obtained by QUEST program is presented. The Si target was sputter-cleaned by Ar ion bombardment. Therefore, a small amount of Ar atoms was assumed to be present in a solid when simulating the energy spectrum. The Ar content as well as the FWHM of the Lorentzian intrinsic spectrum was varied in calculations to fit the experimental curve. The energy dependence of the inelastic mean free path was accounted for approximately to cover the energy-loss region exceeding significantly the usual quasielastic regime. The QUEST program is seen to reproduce quite well the basic features of the energy spectrum in the vicinity of the characteristic peaks of Si 2s and 2p photoelectrons. In particular, the multiple plasmon excitations are unambiguously identified. On the other hand, deficiencies of the algorithm which are common for such kind of programs are also clearly visible. First of all, there is no possibility to calculate the intrinsic energy distribution from first principles. The initial spectrum shape is to be chosen in advance. This is done, as a rule, by adopting a simplified Lorentz-type distribution. As a result, any peculiarities of shake-up and shake-off processes are virtually lost. Second, the energy dependence of the inelastic scattering cross section is accounted for approximately. One can see that model spectrum has a higher inelastic background than that obtained experimentally for energy losses larger than 200 eV. This is in disagreement with similar calculations performed by Alkemade et al. [250] who report on a theoretically obtained background being smaller than the experimental one. Nonetheless, the QUEST represents a necessary step forward in developping reliable software for quantitative surface analysis by AES/XPS.

D. Basic secondary emission characteristics in AES/XPS

(i) Total Auger and photoelectron yields. Until recently the issue of total signal Auger and photoelectron yields has attracted little attention from researchers since in practical AES/XPS analysis relative intensities have been routinely used. Meanwhile, a progress in development of a new generation of cylindrical mirror analyzers capable of obtaining an absolute yield of signal Auger and other secondary electrons [262–265] makes it possible to use an additional means in quantification: absolute intensities and total yields.

There are few papers in literature devoted to theoretical studies of total yields of signal electrons. Tilinin and Werner [145] found an analytical solution of the Auger-electron emission problem and presented an expression for the total yield of Auger electrons, *i.e.*, electrons collected in the 2p-solid angle. Later, Tilinin et al. [266,267] considered a more general problem of anisotropic emission of photoelectrons with the major emphasis on the total escape probability y for an electron to leave a sample without being scattered inelastically. In particular, the result found in ref. [266] in the transport approximation reads

$$y = y_0 \lambda_{tr} \omega [(\nu_0 - 1 + \chi_0)/\omega - (\beta/64)(3\mu_\gamma - 1)], \tag{3.25}$$

where $y_0 = MF\sigma_{ex}$ is the generation rate of signal electrons and μ_γ is the cosine of the x-ray angle of incidence, the single scattering albedo ω is defined by (3.16), except for the elastic mean free path λ_e is replaced by the transport mean free path λ_{tr}. The function χ_0 increases almost proportionally to the single scattering albedo ω, according to the law $\chi_0 \sim \omega/4$, and is small compared to unity. The quantity ν_0 is the positive root of the characteristic equation

$$1 = (\omega \nu_0/2) \ln[(\nu_0 + 1)/(\nu_0 - 1)]. \tag{3.26}$$

In (3.25), we omitted a small integral term in the right-hand side, whose contribution does not exceed a few percent [266]. In the case of Auger electrons the initial angular distribution is isotropic and the asymmetry parameter $\beta = 0$. Note that the quantity y represents the total number of signal electrons crossing a unit area of the surface per unit time and, thereby, has a dimension [electron/cm$^2\cdot$ s].

As it is seen from (3.25) the total yield, apart from the electron excitation rate y_0 , depends on the characteristics of inelastic and elastic scattering. In the limiting case of strong absorption ($\lambda_i \ll \lambda_{tr}$), when elastic scattering is negligible, formula (3.25) reduces to the result of the straight line approximation (SLA) $y = (y_0\lambda_i/4)[1 - (\beta/16)(3\mu_\gamma^2 - 1)]$. In the opposite limiting case of intensive elastic scattering ($\lambda \gg \lambda_{tr}$) the positive root of the characteristic equation

becomes large compared to unity $\nu_0 \gg 1$. This means physically that the major contribution to the yield is provided by diffusely scattered electrons. Those electrons are to a large extent randomized and, as a result, the quantity y becomes almost independent of the x-ray angle of incidence, $y \sim (\lambda_i \lambda_{tr})^{1/2}$. In the medium energy range, however, the ratio $\lambda_i/\lambda_{tr} \sim 1$ and the expression in the right-hand side of (3.25) is usually evaluated numerically. In this connection, a simple approximate formula for the root ν_0 is worth mentioning, namely, $\nu_0 = 1 + 2\exp(-2/\omega)$, which provides a good assessment of ν_0 for the single scattering albedo $\omega \leq 0.4$ [145].

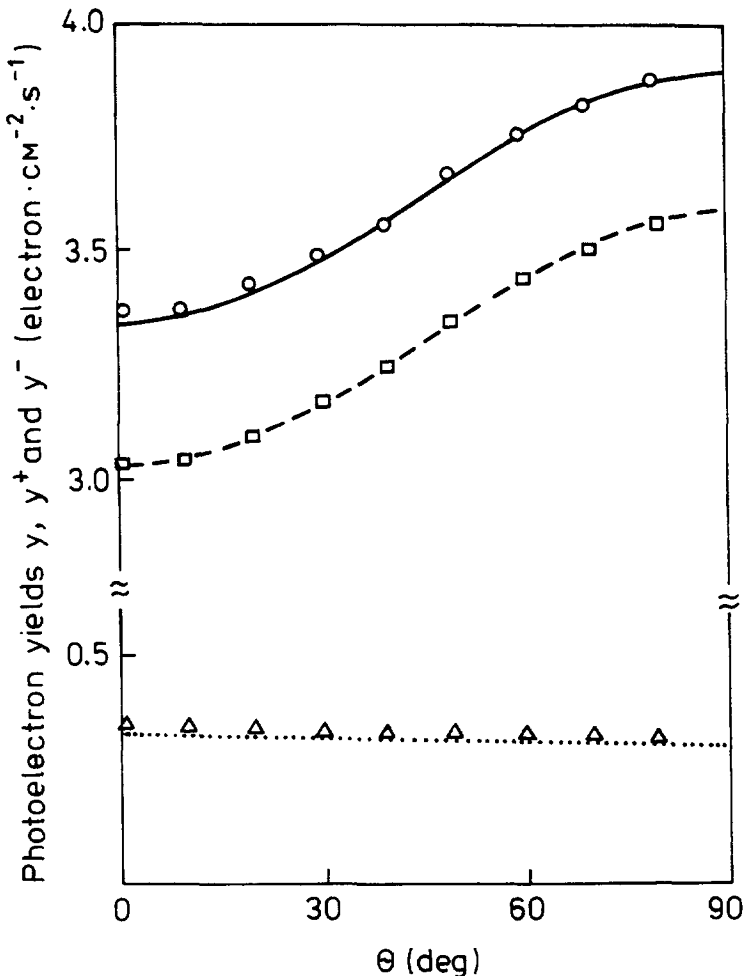

Fig. 16. The dependence of the total and partial yields of photoelectrons emitted from a silver target on the x-ray angle of incidence θ. It is assumed that a small amount of Au atoms is embedded in the Ag sample. Calculations are made for the Au 4f line (the photoelectron energy 1180 eV and the asymmetry parameter $\beta = 1.08$). The analytical and Monte Carlo results are compared on an absolute scale for a model source of photoelectrons, pertaining to the number of simulated trajectories. The solid, dashed and dotted curves are the analytical results, while the open circles, squares and triangles are the MC data for the yields y, y^+ and y^-, respectively (after ref. [267]).

The approach developed in ref. [266,267] was also used to evaluate the contributions of signal electrons emitted initially towards the bulk (y^-) and towards the surface of the sample (y^+), so that the total yield $y = y^- + y^+$. It should be stressed that in the SLA the quantity y^- is identically zero as electrons with the momenta directed towards the bulk cannot change the direction of motion in absence of elastic scattering (angular deflections in inelastic collision events are assumed to be negligible). It was found that, although the yield y^- is small, $y^-/y^+ \sim 0.1$ the electrons emitted towards the bulk make a noticeable contribution to the quantity y.

In Fig. 16, the total yield y as a function of the x-ray angle of incidence θ counted from the surface normal is shown for an Ag target and 1180 eV electrons. The analytical results obtained in the transport approximation are displayed by a solid curve while those found by MC technique are shown by open circles. The yields y^- and y^+ are presented by dashed and dotted curves and open squares and triangles, correspondingly. The analytical results are seen to agree perfectly with the MC simulation data. Especially remarkable are satisfactory predictions of the transport approximation for the partial yield y^- with respect to values found by MC procedure.

Generally, elastic scattering tends to decrease the escape probability as attenuation of electrons moving towards the surface augments with "switching on" elastic interaction. This effect is partially compensated by the increasing role of signal electrons backscattered from the bulk of the sample.

(ii) Angular and energy distribution of signal electrons in near peak region. The angular and energy distribution of signal photoelectrons can be found most effectively in the transport approximation (*cf.* Section 3B). Tilinin and Werner [145] found the explicit expression for the angular distribution of Auger electrons leaving a solid without being scattered inelastically. Later, their result was generalized for the case of anisotropic photoemission by Jablonski and Tilinin [146] and Werner et al. [252]. Denote by $Y(\Omega)d\Omega$ the number of signal electrons escaping from the target in the infinitesimally small solid angle $d\Omega$ along the unit vector $\Omega = \Omega(\alpha, \phi)$ and retaining their initial kinetic energy. Here α and ϕ are the polar and azimuthal angles counted from the surface normal and the x-ray plane of incidence, respectively. Then the quantity $Y(\Omega)$ reads [146]

$$\begin{aligned} Y(\alpha, \phi) &= (y_0 \omega \lambda_{tr} \cos\alpha / 4\pi) \Big\{ (1-\omega)^{1/2} H(\cos\alpha, \omega) - (\beta/4)(3\cos^2\Theta - 1) \\ &+ (\omega\beta/16)(3\cos^2\theta - 1) \int_0^1 x H(x,\omega) H(\cos\alpha, \omega)(x + \cos\alpha)^{-1}(3x^2 - 1)dx \Big\} \end{aligned} \quad (3.27)$$

Θ being the angle between the x-ray propagation direction and the electron emission direction from the target. Expression (3.27) reduces formally to the case of Auger electron emission for the asymmetry parameter $\beta = 0$ [145]. As it follows from (3.27) the photoelectron angular distribution reproduces partially the major features for the angular dependence of the differential photoelectric cross section. However, distribution (3.27) is much smoother than the initial angular distribution of photoelectrons ejected from atoms. For instance, the relative number of signal electrons emerging from the solid in the directions of minima of the initial angular distribution is increased. This is clearly seen in the case of s-photoelectrons, when anisotropy of photoemission is characterized by the asymmetry parameter $\beta = 2$. Indeed, in the dipole approximation, no s-photoelectrons are moving initially in the directions parallel or antiparallel to that of x-ray propagation. However, due to elastic collisions some of the electrons can change their momenta and escape from the target in the directions forbidden by the dipole transition rules. Suppose, for example, that x-rays are incident and photoelectrons are collected along the surface normal ($\alpha = \theta = 0$). Then we obtain by expanding (3.27) on powers of the ratio λ/λ_{tr} and retaining only the first term that for $\beta = 2$ the distribution $Y(0, \phi) \sim y_0(\lambda_i^2/\lambda_{tr})$. Similar analysis reveals that the relative number of electrons leaving the sample in the directions corresponding to maxima of the initial angular distribution is decreased due to elastic collisions. Thus, the elastic scattering effect tends to redistribute signal electrons over the emission directions from a solid and leads to overall decrease in intensity as compared to the result of the SLA, when elastic collisions are neglected. The latter situation corresponds to the limiting case of weak scattering $\lambda_{tr} \gg \lambda_i$. Under this condition the H-function is close to unity, $H \sim 1$, while the single scattering albedo is small, $\omega \ll 1$, so that the right-hand side of (3.27) becomes proportional to the differential photoelectric cross section. A detailed comparison of the MC simulation data and predictions based on (3.27) was performed elsewhere [146].

Figure 17 shows the angular distributions of $2p_{3/2}$ photoelectrons escaping from a copper target as a function of the x-ray angle of incidence for different polar emission angles α. Calculations are made in the plane of incidence of x-rays. For convenience, the negative values of the angle θ pertain to the emission direction $\phi = 180°$, so that the analyser and the x-ray beam are to the same side from the surface normal, while positive θ correspond to the geometry with the analyser being at the opposite side from the surface normal with respect to the beam. The analytical results found from (3.27) are shown by solid curves. They are in good agreement with the MC data points shown by open circles. Contrary to this, the distributions obtained in the straight line approximation over- and underestimate the intensity depending on the emission geometry.

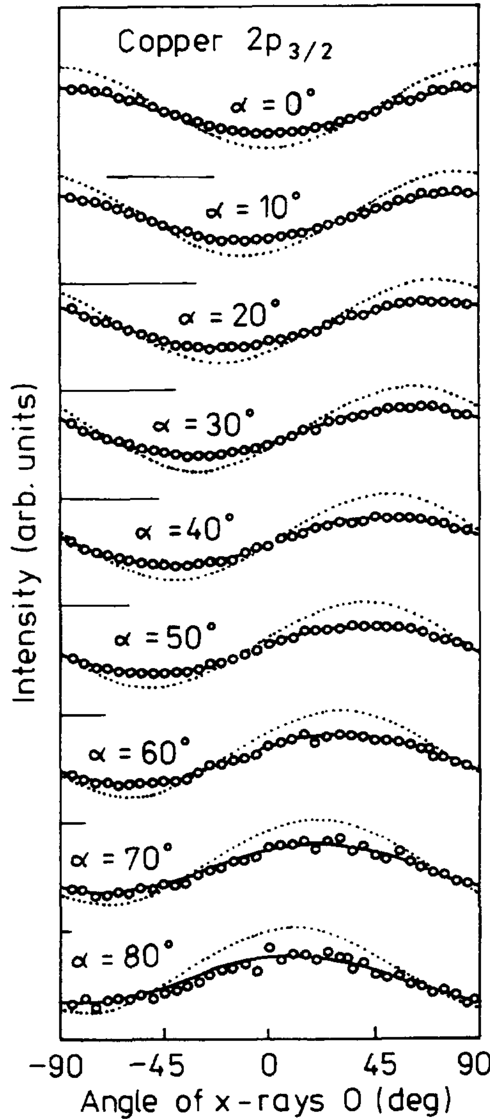

Fig. 17. Dependence of the Cu 2p photoelectron line intensity on the x-ray angle of incidence θ for various polar emission angles α. Solid curves – calculations by formula (3.27) open circles – Monte Carlo data, dotted curves: straight line approximation results (after ref. [146]).

The discrepancies between results found by accounting for and neglecting elastic scattering may reach up to 30%.

The function $Y(\Omega)$ actually describes the integrated peak intensity under the tacit assumption of inelastic background being properly removed so that only electrons not scattered inelastically

are registered. In practice, however, a user obtains an energy spectrum with a peak accompanied by a quite extended tail comprising electrons with different energy losses. Since the initial (intrinsic) spectrum of Auger or photoelectrons is far from being of a δ-function shape the problem arises how to subtract accurately the background of inelastically scattered electrons. The energy-loss spectrum of signal electrons in the vicinity of a characteristic peak is to a large extent determined by the differential inelastic scattering cross section $\omega(E_0 \mid \varepsilon)$. Hence the issue splits into two parts: (1) determination of the function $\omega(E_0 \mid \varepsilon)$ and (2) derivation an appropriate deconvolution formula relating the measured energy distribution and the intrinsic one. The last point is known in the literature as an *inelastic background subtraction.* After the intrinsic spectrum is obtained it can be integrated to get an excitation rate of signal electrons.

Unfortunately, it is not so easy to derive the energy-loss function from first principles for a specific sample. Therefore, considerable efforts have been made during the last decade [167,203,269, 270] to obtain the function $\omega(E_0 \mid \varepsilon)$ experimentally. Tougaard and Kraaer [203] calculated the differential inelastic scattering cross section from measured energy spectra obtained in REELS experiments. They assumed that electrons were travelling in a semi-infinite medium and used the dielectric-function formalism to evaluate the quantity. A good agreement was found between the theory and experiment at large energies of incident electrons ($E \sim$ several keV). Yubero and Tougaard [167] proposed a theoretical model to describe REELS spectra. In this model, an electron is supposed to move along the surface normal before and after an elastic scattering event and a physical picture of the backscattering process is rather simplified. In addition, an integral equation relating the measured energy spectrum and an unknown energy-loss function, employed in refs. [167,203] is based on the results found in P_1-approximation [271,272]. This approximation is known to be inadequate when describing electron transport in the case of highly anisotropic angular distributions relevant to REELS [241]. Despite these simplifications the authors of refs. [10,11] were able to get a realistic estimate of the normalized inverse differential inelastic mean free path $\lambda_i w(E_0 \mid \varepsilon)$ on an absolute scale for several materials and primary electron energies. In particular, it was found experimentally that the differential inelastic scattering cross section for aluminium comprises mainly a strongly pronounced plasmon peak at the energy loss about 15 eV and a small background whose contribution to the total probability of inelastic scattering is almost negligible for energy losses less than 50 eV [272]. Figure 18 displays some of the results by Tougaard and Kraaer [203] for the normalized energy loss function of a Cu target.

Yoshikawa et al. [273,274] resorted to a MC technique to account in a more realistic way for elastic collisions when deriving a deconvolution formula. Application of this corrected deconvo-

lution procedure to processing REELS spectra of a gold target and 1 keV electrons enabled them to determine a differential inelastic scattering cross section, which turned out to be substantially different from the optical energy-loss function [274]. Their result is shown in Fig. 19. It is seen that the differential inverse inelastic mean free path derived from REELS spectra diminishes much more rapidly at large energy losses. On the other hand, the optical energy-loss function is smaller by almost a factor of two than that obtained from REELS in the energy-loss range from 0 to about 25 eV. Yoshikawa et al. found further the intrinsic energy spectrum of Au 4f photoelectrons to be characterized by a much shorter tail than that reported by Tougaard [275]. The shape of the differential inelastic scattering cross section of a gold target obtained in ref. [274] agrees only qualitatively with that of Tougaard and Kraaer [203].

A simple formula for the energy spectrum of Auger electrons leaving a sample with small energy losses was found in ref. [241] in the transport approximation, *viz.*

$$Y(\mu, \Delta \mid E_0) = \mu \lambda_{tr} y_0 P_0(\mu)(4\pi i)^{-1} \int_{c-i\infty}^{c+i\infty} [1 - k(\mu)\tilde{w}(p)] \exp(p\Delta) dp, \tag{3.28}$$

where $P_0(\mu) = \omega H(\omega, \mu)/(1-\omega)^{1/2}$ is the probability for an electron to escape from the sample without being scattered inelastically,

$$k(\mu) = 1 - (\omega/2)/\{1 + \mu[3(1-\omega)]^{1/2}\} \tag{3.29}$$

and $\tilde{w}(p)$ is the Laplace transform of the differential inverse inelastic mean free path with respect to the relative energy loss $\Delta = (E_0 - E)/E_0$. Expression (3.28) is derived for an infinitesimally narrow intrinsic energy spectrum and is similar to that found by Tofterup [276], yet differs from the latter by containing the angle-dependent function $k(\mu)$. Besides that, the angular distribution described by (3.28) depends on the ratio λ_i/λ_{tr}, while the shape of the angular distribution derived in ref. [276] in the P_1-approximation does not depend on any elastic scattering characteristics. The accuracy of (3.28) was checked against the MC simulation data and comparison was performed in the absolute scale. In Fig. 20, the energy distributions of electrons emitted from a silver target along the surface normal in the case of a Lorentzian true spectrum ($E = 1000$ eV) with a FWHM of 1 eV is shown for illustration. The theoretical curve was calculated for a model energy-loss function of Tougaard [277]. The analytical results are seen to compare well with the MC data shown by open circles.

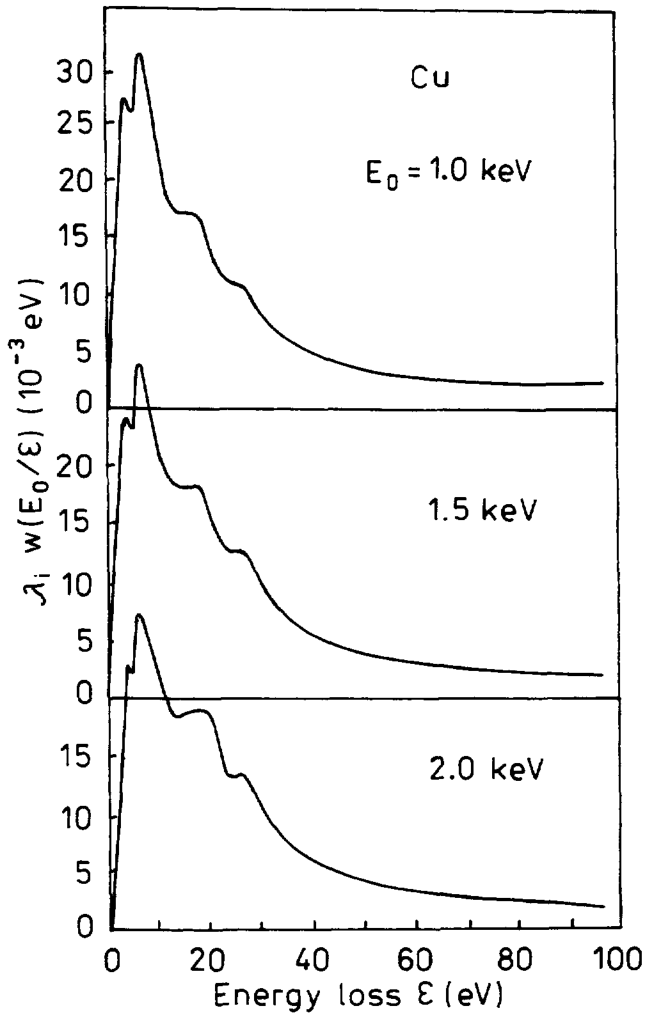

Fig. 18. The dependence of the normalized differential inverse inelastic mean free path on the energy loss for a Cu target. Solid curves represent experimental results of ref. [203].

Once the differential inverse inelastic mean free path is known the energy distribution of emitted signal electrons can be calculated via a convolution of the pathlength distribution and the energy-loss function of Landau [278]. The pathlength distribution $Q(R,\Omega)$ describes the probability for an electron to leave a sample after travelling a certain pathlength R in the direction Ω.

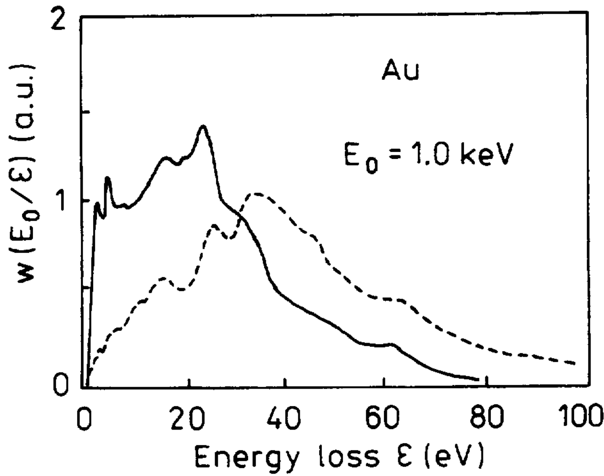

Fig. 19. The differential inelastic scattering cross section of a gold target versus the energy loss. Solid curve – experimental results from REELS spectra, the angle of incidence and the take-off angles are equal to 45°, dashed curve – the optical energy-loss function (after ref. [274]).

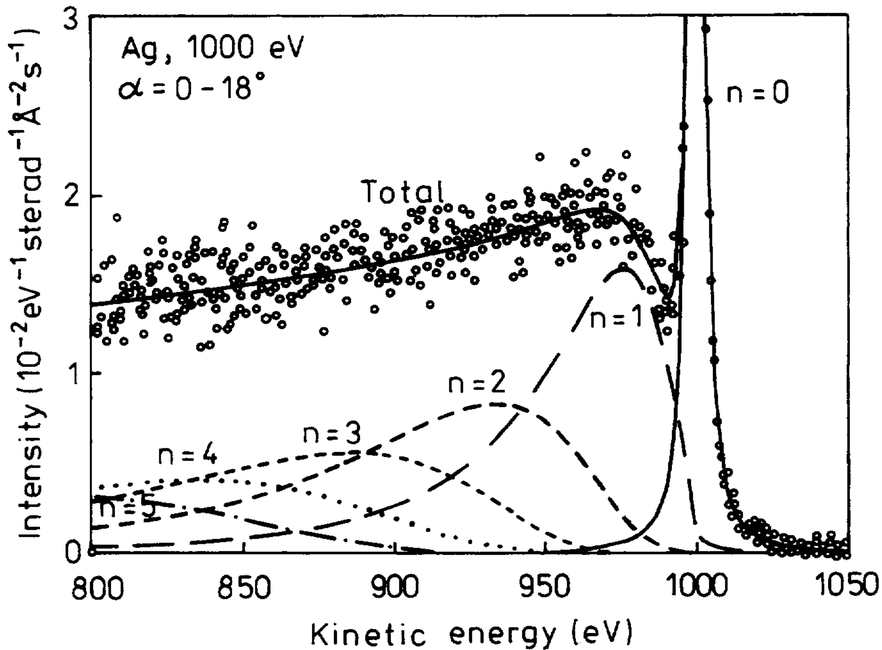

Fig. 20. Model energy distributions of 1000 eV Auger electrons escaping from a silver target. Solid curve – analytical calculations (TA), data points – MC simulation results (after ref. [241]). Dashed lines are the contributions of electrons scattered n times inelastically before leaving the target. The polar emission angle range $\alpha = 0 - 18°$ (after ref. [241]).

If elastic scattering is disregarded the pathlength distribution does not depend on the travelled pathlength, which means that all electrons with the initial momenta directed towards the surface escape from the target sooner or later. Elastic collisions modify the pathlength distribution in such a way that it becomes strongly dependent on the emission geometry and the initial angular distribution. Indeed, due to a possibility of a momentum change in an elastic collision event, an electron which moves initially towards the bulk of the target may be scattered at a large angle and, as a result, escapes from the solid. The function $Q(R, \Omega)$ was calculated by Tofterup [276,279] in the P_1- or diffusion approximation. Deficiencies of the diffusion approximation result in a number of unphysical predictions concerning the behaviour of the function Q. One of them is the angular dependence of the escape probability for electrons travelled a zero pathlength. It is clear in advance that all electrons leaving a solid in any direction after travelling an infinitesimally small pathlength should be characterized by the same value of the pathlength distribution [241]. Another problem is independence of the shape of the pathlength distribution on the emission direction.

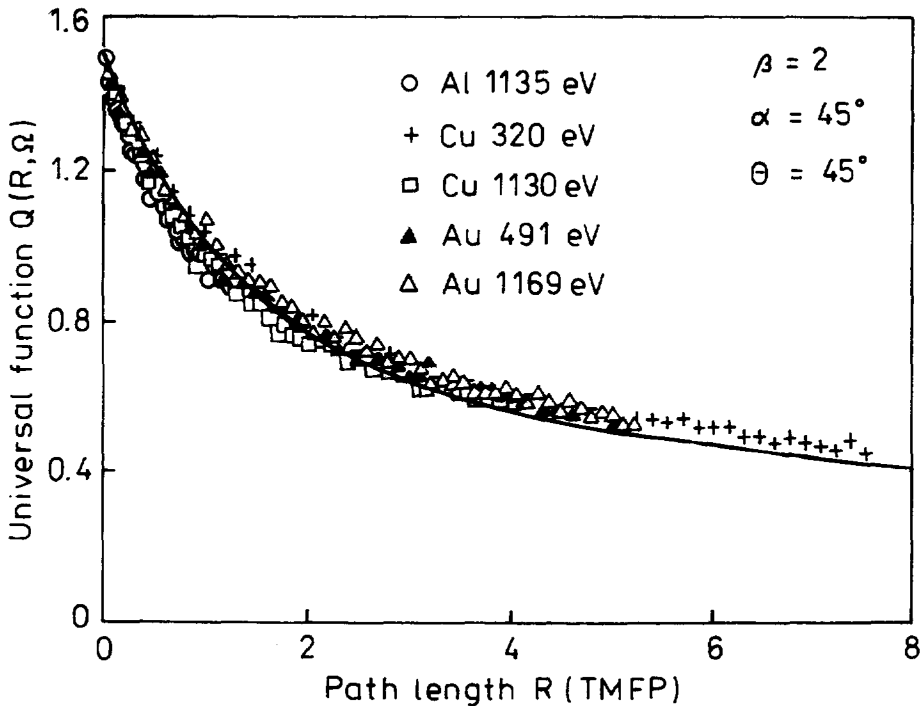

Fig. 21. Comparison of the universal pathlength distribution function $Q(R, \Omega)$ with the results of the Monte Carlo calculations. The XPS configuration is defined by $\alpha = \theta = 45°$. Note that the travelled pathlength is expressed in units of the transport mean free path (after ref. [242]).

The distribution over the travelled pathlengths, accounting correctly for elastic collisions was found in the TA for isotropic emission by Tilinin and Werner [241]. Their result was generalized

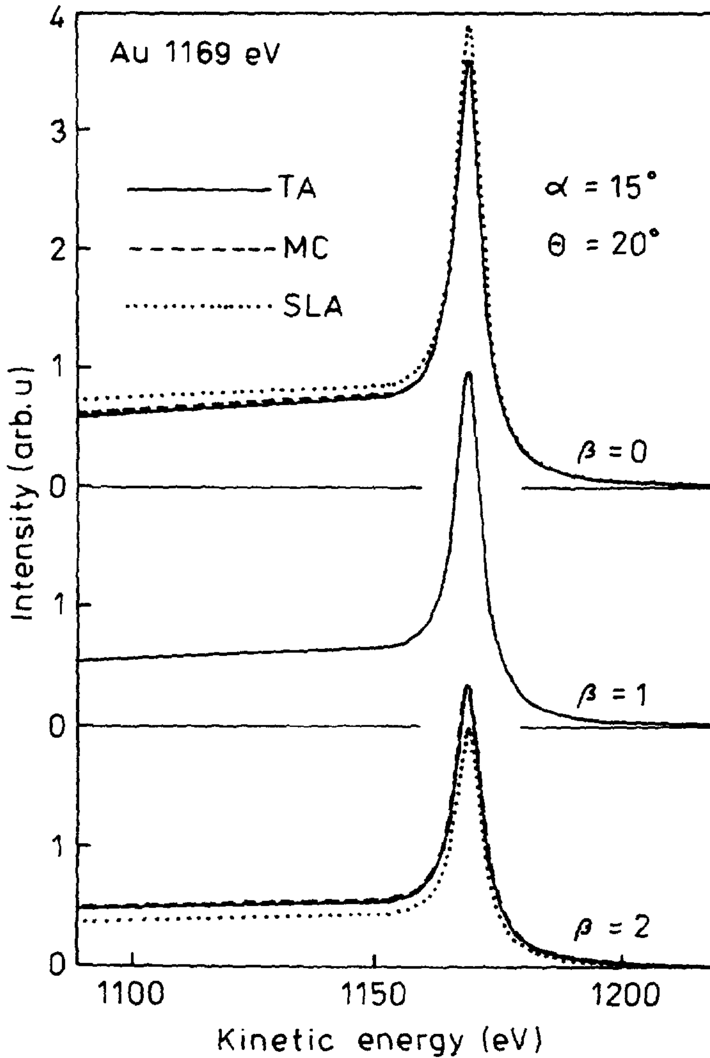

Fig. 22. The energy spectra calculated by a convolution of the pathlength distribution and the energy-loss function of Landau [278] for a model differential inverse inelastic mean free path of Tougaard [277]. Solid and dashed lines correspond to the pathlength distribution functions found in the transport approximation and by MC simulation, respectively. Dotted line: straight line approximation, elastic scattering is neglected. XPS configuration is defined by $\alpha = 15°$ and $\alpha = 20°$ (after ref. [242]).

later for the case of anisotropic photoemission in ref. [242]. The analytically derived distribution Q was tested by comparison with MC simulation data for different geometries, Auger and photoelectron lines and the asymmetry parameter values [241,242]. It was found that the path-

length distribution is, within 10% accuracy, a universal function of the ratio R/λ_{tr}, where R is the travelled pathlength. As an example, in Fig. 21 the universal function $Q(R, \Omega)$ is shown by the solid curve for the asymmetry parameter $\beta = 2$ and the emission geometry $\alpha = \theta = 45°$. The results of MC simulation are displayed by data-points. The influence of elastic collisions on the peak height and the background shape is illustrated in Fig. 22, where model energy spectra of photoelectrons emitted from a gold target are shown for the XPS configuration $\alpha = 15°$ and $\theta = 20°$ and different asymmetry parameter values. It is seen that elastic collisions may increase or decrease the peak height and background intensity by 15–20%.

(iii) Escape probability as a function of depth of origin. Escape probability of signal electrons from solids is a complicated function of target scattering properties, initial angular distribution and depth of origin. Knowledge of this quantity is important for both determination of sensitivity factors of standard uniform samples and depth profiling of inhomogeneous specimens by angle resolved AES/XPS. In the past, the escape probability was believed to be exponentially decaying with depth. Such an assumption is justified under the condition of a negligible role of elastic scattering. However, MC simulation studies based on realistic Mott differential elastic scattering cross section [205,244,247,248,280,281] and an analytical approach employing a transport equation [145,282,283] indicate that it is not the case.

The escape probability as function of generation depth is described by the so-called *depth distribution function* (DDF) introduced by Jablonski and Ebel [1]. The DDF describes the probability for an electron generated at a certain depth z to leave a solid in the direction Ω. This function is frequently denoted by $\Phi(z, \Omega)$. Tilinin and Werner [145] related the depth distribution function with the outgoing flux of signal electrons at the surface. By making use of the transport approximation to solve a boundary-value problem they found an analytical expression for the DDF in the case of isotropic emission. The analytical DDF [145] turned out to be a universal function of the reduced depth $\tau = z(\lambda_i + \lambda_{tr})/\lambda_i\lambda_{tr}$ and comprises three terms which have a clear physical meaning. The first term is zero at the surface. It increases at shallow depths, reaches a maximum and then begin to decrease at large depth $\tau \gg 1$ proportionally to $E_1(\tau) \sim \exp(-\tau)/\tau$, where $E_1(\tau)$ is the integral exponential function, which describes the electrons emitted initially towards the bulk and scattered at arbitrary angles. The second term corresponds to particles emerging from the target without undergoing any elastic scattering at all. The signal intensity of those electrons is governed by the exponential function $\exp(-\tau/\mu)$. In the TA this group of particles includes electrons having suffered multiple small-angle scattering after travelling a path-

length being less or of the order of the transport mean free path. Finally, the third term depends on the product of two functions. One of them is only a function of the angular variable while the other depends on depth. The depth dependent part of the third term decreases exponentially with τ. However, the slope of the exponent in the latter case is determined by the diffusion length $\lambda_d = \nu_0\lambda_i\lambda_{tr}/(\lambda_i + \lambda_{tr})$, where ν_0 is the root of characteristic equation (3.26). Thus, the third term describes the escape probability of the randomized fraction of electrons.

The depth distribution function for 250 eV Auger electrons in a Co target [145] is shown in Fig. 23 for different emission directions. Open circles are the MC simulation results for a realistic Mott differential elastic scattering cross section. Filled triangles correspond to the solution of the kinetic equation in the transport approximation. Also displayed for comparison by solid curves is the empirical DDF proposed in ref. [248].

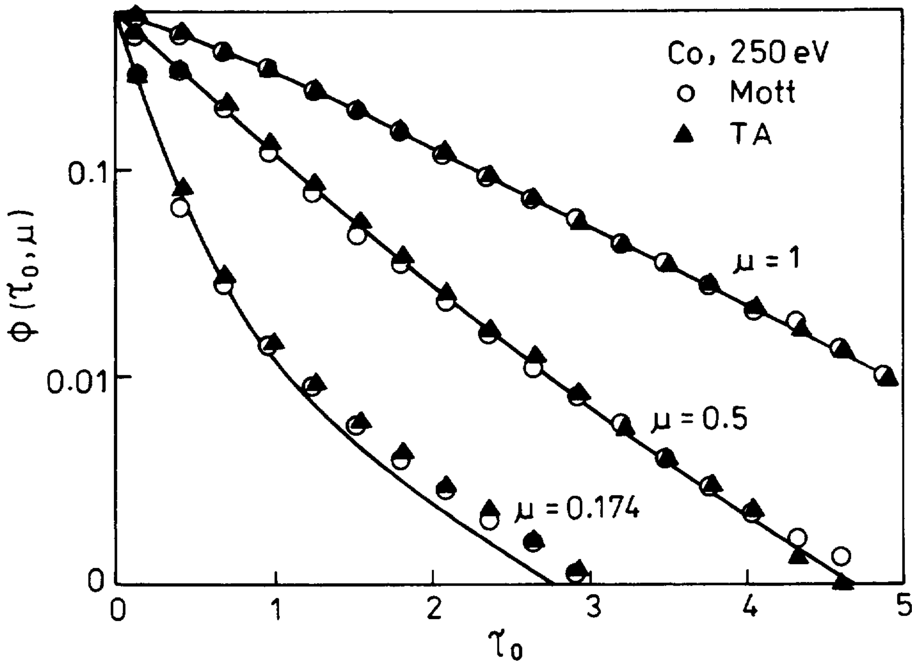

Fig. 23. The escape probability of signal Auger electrons from a Co target as a function of the reduced depth of origin τ. The emission direction is characterized by the cosine of the polar angle μ so that the values $\mu = 1.0, 0.5$ and 0.174 correspond to $\alpha = 0, 60°$ and $80°$. Open circles – MC simulation data, filled triangles – analytical solution (TA), solid curves – empirical DDF of ref. [248].

The influence of anisotropy of photoemission on the shape of the DDF was investigated in refs. [207,244,280,281]. It was found the DDF exhibits a nonmonotonic behaviour as a function

of generation depth of s-photoelectrons in Al and Au for the asymmetry parameter values 2.0 and 1.8, respectively, and emission directions close to that of x-ray propagation. Under these conditions, the escape probability reaches a maximum at the depth being approximately by a factor of two smaller than the IMFP value. In ref. [207] the DDF was studied experimentally, analytically in the TA and by the MC technique. The analytical expression for the DDF derived in ref. [207] depends strongly on the initial angular distribution of excited photoelectrons. In the

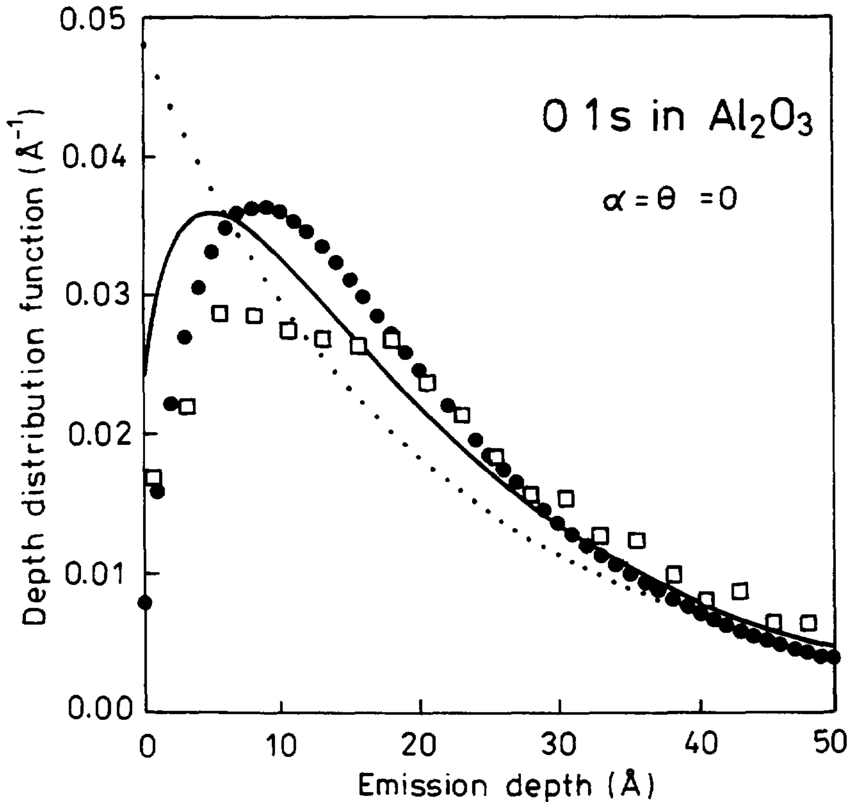

Fig. 24. The depth distribution function of O 1s photoelectrons in aluminium oxide for the XPS configuration $\alpha = 0, \theta = 180°$. Filled circles – experiment, open squares – MC simulation results, solid curve – analytical DDF obtained in the TA, dotted curve – exponential DDF disregarding the elastic scattering effect (after ref. [207]).

directions of minima of the photoelectric cross section this function is no longer exponential. On the contrary, it may be essentially nonmonotonic in the vicinity of the surface. In particular, the DDF may reach a maximum at the depth comparable with the inelastic mean free path (*cf.* Fig. 24). It isinteresting that for s-photoelectrons, whose angular distribution is characterized by the asymmetry parameter $\beta \sim 2$, this maximum is quite well pronounced and may exceed the

corresponding value of the DDF at the surface by 50% [207] for all elements of the periodic table.

Experimental determination of the DDF represents a difficult task. Such measurements would imply preparation of a sample with a thin signal layer (marker) placed at a certain depth beneath the surface. Bearing in mind that considerable problems arise in connection with growing a well defined monolayer in a nanoscale sample it comes as no surprise that no experimental data have been available in the literature until recently. A new method to find the DDF experimentally has been proposed in ref. [207]. It turned out that instead of employing a sample with a marker it is possible to obtain the escape probability from overlayer experiments provided the ratios of the inelastic to transport mean free paths of the overlayer and the substrate are identical. Then the DDF in an overlayer material can be found by differentiating the overlayer signal with respect to the overlayer thickness. For this purpose, thin Al_2O_3 overlayers were deposited on an aluminium substrate and the O 1s photoelectron line intensity was measured as a function of the Al_2O_3 overlayer thickness. Experimental data of ref. [207] are shown in Fig. 24 by filled circles for the XPS configuration $\alpha = 0, \theta = 180°$ (x-rays are incident from the opposite side of the target). Solid line is the analytical DDF found in the transport approximation, open squares are the corresponding MC data. Also displayed for comparison by the dotted line the exponential DDF proportional to $\exp(-z/\lambda_i)$. All the DDFs shown in Fig. 24 are normalized to unity. The photoelectrons are collected in a narrow solid angle with a half-cone of acceptance 4.1°, along the normal. Both the experimental data and the theoretical results accounting for elastic scattering point out the existence of a maximum of the escape probability at the depth of the order of $(0.3 - 0.5)\lambda_i$.

(iv) Mean escape depth. The mean escape depth of signal electrons is one of the basic quantities characterizing the surface sensitivity of AES/XPS. Unlike the attenuation length, the average escape depth is a well defined quantity that can be found from

$$D = \int z\Phi(z,\Omega)dz \left(\int \Phi(z,\Omega)dz\right)^{-1}, \tag{3.30}$$

where $\Phi(z,\Omega)$ is the depth distribution function. As follows from definition (3.30), in the absence of elastic scattering, the mean escape depth becomes equal to the product of the inelastic mean free path and the cosine of the emission angle, $D = \mu\lambda_i$. The latter result is obtained immediately from the assumption of an exponentially decaying escape probability. However, elastic collisions of signal electrons cause significant deviations of the quantity D from a simple estimate $\mu\lambda_i$. As pointed out by Jablonski and Zemek [281] the mean escape depth of s-photoelectrons in the directions of minima of the photoelectric cross section can be considerably larger than $\mu\lambda_i$. Based

on the results of MC calculations they found that for Al 2s photoelectrons leaving a solid at the angle $\Theta = 5°$ with respect to the surface normal and the direction of x-ray propagation $D = 31.7$Å. Meanwhile, the product $\mu\lambda_i = 25$ Å, which agrees completely with the nonmonotonic behaviour of the DDF discussed in the previous section.

The analytical expression for the mean escape depth was first derived by Tilinin et al. [284] in the transport approximation for unpolarized radiation. and later was generalized for the case of polarized x-rays [285]. The result found in ref. [284] reads

$$D = \lambda_i \lambda_{tr}(\lambda_i + \lambda_{tr})(\cos\alpha + W) \tag{3.31}$$

where the function W depends on the geometrical configuration and scattering properties of the target (the quantity W is approximately proportional to the ratio of the single scattering albedo $\omega = \lambda_i/(\lambda_i + \lambda_{tr})$ to the angular distribution of electrons leaving a sample, (3.27)). In the limiting case of weak scattering ($\lambda_{tr} \gg \lambda_i$) all the terms in the right-hand side of (3.31) proportional to the ratio λ_i/λ_{tr} can be omitted and (3.31) reduces to the familiar expression: $D = \lambda_i \cos\alpha$. In the opposite limiting case of intensive scattering ($\lambda_{tr} \ll \lambda_i$) the mean escape depth becomes proportional to the diffusion length, $D \sim (\lambda_i \lambda_{tr})^{1/2}$ irrespective to the emission direction [284,285].

From (3.31), it follows that the average escape depth of signal photoelectrons is anisotropic even for amorphous materials. The origin of this anisotropy can be traced out by considering a more general case of polarized radiation. Analysis shows that, if the initial wave-function symmetry is not too sophisticated, then photoelectrons are ejected from atoms most probably in the directions parallel or antiparallel to that of the electric-field-vector oscillations. Such a situation corresponds to positive values of the asymmetry parameter $\beta > 0$ for vast majority of s, p, d and f -photoelectrons. Suppose the analyser collects the photoelectrons in the direction where the initial angular distribution becomes zero. Then, in order to leave a target in this direction a photoelecton has to change its momentum. which can be done in an elastic collision after travelling a certain pathlength. Therefore, such electrons, on the average, travel larger pathlengths and escape from larger depths. Exactly the opposite is true for photoelectrons registered in the directions pertaining to maxima of the differential photoelectric cross section.

It should be stressed that multiple scattering sets an ultimate limitation on the probe volume of the near surface region studied by AES/XPS, as is clearly seen from (3.31). Indeed, due to the presence of the term W in the right-hand side of (3.31) the mean escape depth D cannot be made infinitesimally small by decreasing the cosine of the emission angle α, *i.e.* by applying a grazing emission geometry.

The dependence of the mean escape depth on the XPS configuration may be conveniently studied by analysing the ratio $d = D/\lambda_i \cos\alpha$. Note that the average reduced depth d is always unity in the usual formalism of AES/XPS. In Fig. 25 the correlation between the initial angular distribution and the mean escape depth of Au 4s photoelectrons is shown for a fixed value of the polar emission angle $\alpha = 60°$. The reduced mean escape depth is seen to be minimal in those x-ray propagation directions where the differential photoelectric cross section reaches its maxima and vice versa.

Zemek el al. [286] seem to be the first to obtain the mean escape depth of signal photoelectrons in aluminium oxide directly from overlayer experiments. Their method is substantiated for overlayer/substrate combinations with close values of the scattering parameter $\chi = \lambda_i/\lambda_{tr}$ of the overlayer and substrate materials. The system Al_2O_3/Al perfectly meets this requirement. The authors of ref. [286] found experimentally that the reduced mean escape depth d depends on the XPS geometry. In particular, the reduced depth is larger than unity for emission directions close to that of x-ray propagation and less than unity at emission angles $\sim 60°$ with respect to the x-ray direction of incidence. The results of ref. [286] are in good agreement with both MC simulation data and predictions of (3.31).

(v) **Partial escape probability**. The angular and energy distribution of secondary electrons comprises contributions of particles scattered $n = 0, 1, 2, \ldots$ times inelastically. Hence, without loosing generality, this distribution can be presented by a series each term of which corresponds to the probability for an electron to escape from a sample after undergoing a certain number of inelastic collisions. This probability is referred conveniently to as a partial escape probability. Such a representation has a clear physical meaning and allows, for example, to trace easily multiple plasmon energy losses. Generally, a partial escape probability $P_n(\Omega, E)$ is a complicated function of the energy loss and the emission direction due to the pronounced energy dependence of elastic and inelastic scattering cross sections. However, in the vicinity of the peak region pertaining to small energy losses the energy dependence of the aforesaid cross sections can be neglected. As a result, the processes of elastic and inelastic scattering may be viewed as occurring independently and the partial escape probability splits into a simple product of two functions. One of these functions depends only on energy and the other on emission angle. Thus, we have for the angular and energy distribution the expression [241]

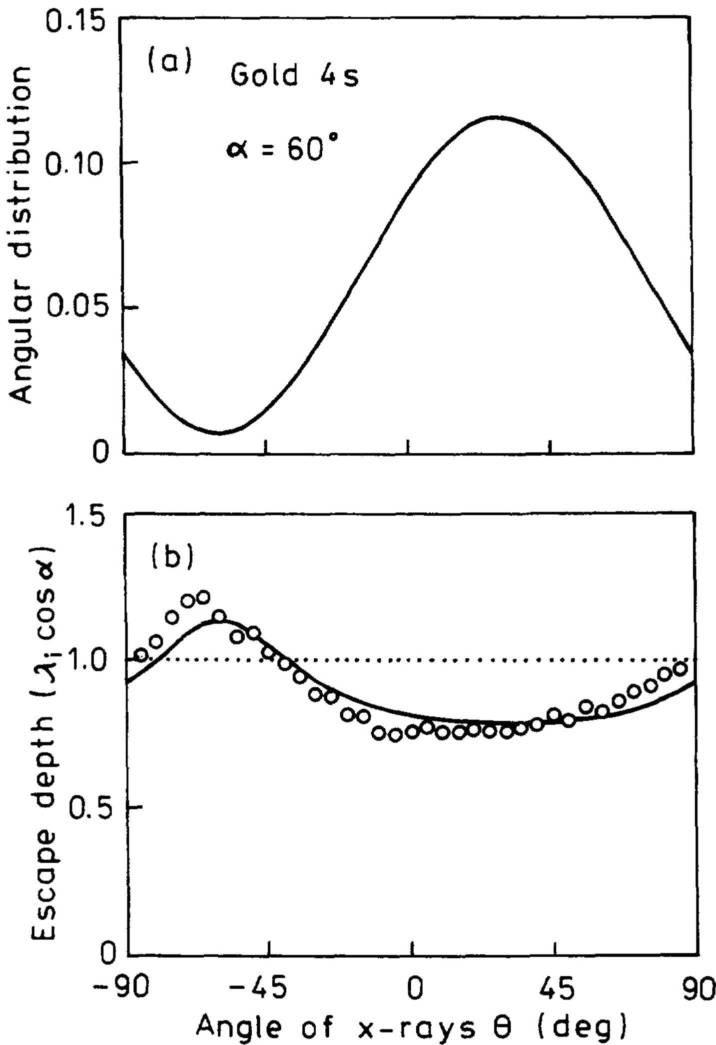

Fig. 25. Correlation between the initial angular distribution (a) and the mean escape depth (b) of Au 4s photoelectrons leaving a gold target in the plane of incidence of x-rays at the polar emission angle $\alpha = 60°$. Solid curve in (b) represents the analytical theory (TA), open circles are the results of the MC simulation and dotted line is the usual XPS formalism prediction. Negative values of the x-ray angle of incidence correspond to the azimuthal emission angle $\phi = 180°$ (after ref. [284]).

$$Y(\Omega, E) = \cos\alpha \, Y_0 \sum_{n=0}^{\infty} P_n(\Omega) F_n(E), \tag{3.32}$$

where Y_0 is the normalization constant proportional to the source power of signal electrons and the function $F_n(E)$ is defined by the n-fold convolution of the intrinsic spectrum $F(E)$ and the

differential inverse inelastic mean free path

$$F_0(E) = F(E), \tag{3.33}$$

$$F_n(E) = \int_0^E F_{n-1}(E')\, w\,(E - E')\, dE', \tag{3.34}$$

Equation (3.32) has another advantage. Convolutions of type (3.34) can be rapidly carried out numerically. Consequently, there is no need to evaluate the quantity $P_n(\Omega, E)$ stochastically. It is sufficient to calculate the probability $P(\Omega)$ irrespective to the energy loss, for instance, by the statistical weights method and then obtain the full distribution by means of (3.32) and (3.34).

In the case of Auger electrons, the quantity $P_n(\Omega)$ is independent of the azimuthal angle by virtue of azimuthal symmetry. The polar emission angle dependence of $P_n(\Omega)$ is pronounced rather weakly due to the fact that Auger electrons are to a large extent randomized. Nonetheless, the function $P_n(\Omega)$ decreases with augmenting the emission angle, which indicates that the probability to escape along the surface normal is larger than in any other direction. Besides that, the quantity $P_n(\Omega)$ diminishes with increasing the number of inelastic collisions n. In particular, for large $n \gg 1$ the probability to escape after being scattered inelastically n times is proportional to inverse square root of the number n, $P_n \sim n^{-1/2}$ [241]. Such behaviour of P_n is explained by the influence of a boundary between vacuum and a solid. Indeed, larger n numbers correspond to larger pathlengths travelled by electrons and to higher probability of those electrons to leave a sample. Consequently, for a steady-state source, the relative amount of particles suffered the $(n+1)$th inelastic collision in the target will be smaller than the number of electrons scattered inelastically n times.

For photoelectrons whose initial angular distribution is anisotropic, the function $P_n(\Omega)$ reproduces approximately the shape of the differential photoelectric cross section for a few first n numbers $n = 0, 1, 2$. As the number n increases, the angular distribution of electrons scattered inelastically n times becomes more and more randomized and the function P_n resembles that of Auger electrons.

The partial contributions of 1000 eV Auger elelctrons escaping from a silver target are shown in Fig. 20 by dashed lines for near normal emission direction. Note, that the background over the energy losses less than 100 eV is almost entirely made up of (0–3) times inelastically scattered electrons.

E. Influence of crystallinity of the Auger and photoelectron line intensity

In Sections 3B-3D, the distribution of atoms in a target has been assumed to be random and multiple elastic and inelastic scattering were supposed to be caused by incoherent interaction on scattering centers subject to stochastic displacements from their equilibrium positions. Meanwhile, in practice, a sample studied by AES/XPS would be rather polycrystalline or crystalline than amorphous. In those cases, an Auger or x-ray photoelectron line intensity is noticeably influenced by periodic arrangement of atoms and coherent scattering (*cf.* Section 3A). In particular, an Auger or photoelectron line intensity as a function of the emission angle is modulated. The degree of modulation, observed experimentally may be as high as $(I_{max} - I_{min})/I_{max} \sim 0.5 - 0.7$ [17] even for an initially isotropic emission. Effects of coherent interaction taking place against the background of multiple incoherent scattering are frequently called *x-ray photoelectron diffraction* (XPD) and *Auger electron diffraction* (AED). XPD and AED have developed as efficient quantitative surface structure probes [1] and the number of researchers making use of them is growing [1,287–298].

The phenomenon of Auger and photoelectron diffraction as applied to surface analysis has been reviewed recently in several papers by Fadley [1,17,287] and Fadley et al. [296]. Our aim is to briefly discuss basic physical assumptions and models used to describe diffraction effects. Since emission of signal Auger and photoelectrons from different atoms is uncorrelated individual emitters located at lattice sites of a crystalline sample are incoherent. Thus to study the angular distribution of intensity it is sufficient to consider a final wave function of an electron ejected from a single atom, accounting properly for the influence of neighbouring atoms. There are basically two approaches used up till now to tackle this problem: the so-called *Kikuchi-band picture* and the *cluster model*. Physically, they may be characterized as long-range and short-range theories, respectively [17]. In the long-range approach, the Hamiltonian for a signal electron excited in a crystalline target is presented in the form $H = H_0 + H_{er} + H_{ev} + H_{ee}$, where H_0 includes the operator of the electron kinetic energy and interaction with external radiation, H_{er} is the average crystalline potential, being periodic according to a lattice symmetry, H_{ev} is the fluctuating part of the crystalline potential caused by thermal vibrations of atoms and, finally, H_{ee} denotes electron-electron interaction responsible for the energy dissipation and comprising mostly inelastic scattering on quasifree or weakly bound outer shell electrons. Scattering on the periodic potential can be shown to lead to Bragg reflections, while the potential fluctuations are responsible for thermal or diffuse scattering.

In the cluster model, no assumption about existence of a periodic potential is made *a priori*. Multiple scattering of signal electrons is treated as scattering of secondary waves propagating in an absorbing medium. However, it is assumed that scattering centers are located in lattice sites. Attenuation of secondary waves is accounted for phenomenologically by means of the attenuation length. The cluster model is a good starting point to understand physics of electron-crystal interaction and in the limiting case of weak attenuation is expected to reproduce the results of the Kikuchi-band picture.

Consider for simplicity, s-photoelectron emission from a point of origin and suppose the outgoing wave function is ψ_0 in the absence of other atoms of the lattice. Then, to the first approximation with respect to scattering on the regular part of the potential, the signal electron wave function reads [1,17,299,300]

$$\psi(\mathbf{r},\mathbf{k}) = \psi_0 + \sum_i \psi_i, \tag{3.35}$$

where the summation is performed over all lattice sites except for that of the emitting atom. Far away from the sample ($r \to \infty$), the functions ψ_0 and ψ_j approach spherical waves and we have

$$\psi_0 \sim (\mathbf{e}\cdot\mathbf{k})\exp(ikr)/r, \tag{3.36}$$

$$\psi_j \sim (\mathbf{e}\cdot\mathbf{r}_j/r_j)f_j(\theta_j)\exp[ikr(1-\cos\theta_j)]/r, \tag{3.37}$$

where $\mathbf{k}$ is the signal electron momentum, $\mathbf{e}$ is a unit vector characterizing the polarization direction, $\mathbf{r}_i$ is the radius vector of the jth atom, θ is the scattering angle counted from the direction along the vector $\mathbf{r}_j$ and $f(\theta_j)$ is the scattering amplitude. Allowing further for electron wave attenuation in a phenomenological way and averaging over thermal displacements of atoms we arrive at the expression for the photoelectron angular distribution in the single-scattering-cluster model [17]

$$Y(\mathbf{k}) \sim \mid F_0 + \sum_j F_j W_j \exp(-i\mathbf{k}\cdot\mathbf{r}) \mid^2 + \sum_j \mid F_j \mid^2 (1 - W_j^2), \tag{3.38}$$

where

$$F_0 = (\mathbf{e}\cdot\mathbf{k})\exp(-R_0/2\lambda_a), \tag{3.39}$$

$$F_j = (\mathbf{e}\cdot\mathbf{r}_j/r_j)f(\theta_j)\exp(ikr_j - R_j/2\lambda_a). \tag{3.40}$$

In (3.39) and (3.40), R_0 and R_j are the pathlengths travelled by the respective waves below the surface, λ_a is the attenuation length and W_j is the *Debye–Waller factor* [297,301]

$$W_j = \exp[-2k^2(1-\cos\theta_j) < u_j^2 >]. \tag{3.41}$$

In the latter expression, $< u_j^2 >$ is a mean thermal displacement squared of atom j. In the high temperature isotropic approximation the mean displacement squared reads $< u_j^2 >= 3\hbar T/mk\Theta_D^2$, where m is the electron mass, T and Θ_D are the absolute and the Debye temperature, respectively [297].

Formula (3.38) is very useful when studying diffraction effects and performing holographic analyses. From (3.38) it follows that the intensity consists of two terms. The first of them contains a sum on interference terms depending on a particular symmetry of a lattice and, thereby, carrying structural information about a sample. The second sum in the right-hand side describes diffuse scattering [17,297]. Note, that in the limiting case of large thermal displacements the Debye–Waller factor is small compared to unity, $W_j \ll 1$, and all interference terms in (3.39) can be neglected, so that the intensity $I(\mathbf{k})$ reduces to the result for a system of randomly distributed scatterers.

Ideally, all atomic positions in a lattice are strongly correlated. However, as it is clearly seen from (3.38) there are a number of factors reducing the influence of remote neighbours on the final wave function of a signal electron. Those factors are: (1) inelastic scattering of electrons and (2) thermal displacements of atoms from their equilibrium positions. Both of these effects are accounted for in (3.38) by means of the attenuation length λ_a. In addition, reduction in correlation of atomic positions due to thermal displacements is described by the Debye–Waller factor $W_j < 1$. The attenuation length plays effectively a role of a typical correlation distance between scattering centers whose contribution to a factor F_j is still noticeable. Since λ_a is usually several interatomic spacings d [302] the main features of the diffraction pattern are associated with a geometrical configuration of $\lambda_a/d \sim 3-5$ neighbouring atoms along a chain although sometimes correlation in positions of atoms separated by more than 20 Å is also important [17,303,304]. As a result, the measured intensity represents a probe of short-range order. Consequently,in model calculations it suffices to account for about $(\lambda_a/d)^3 \sim 30 - 100$ atoms in a cluster to obtain satisfactory results [305]. Though expression (3.38) is formally derived in the single-scattering approximation, generalization to include multiple scattering can be carried out a straightforward manner. In the latter case, the quantity F_j must be supplemented by contributions of various multiple-scattering pathways that terminate at point $\mathbf{r}_j$ [1].

For illustration, Fig. 26 displays an azimuthal scan of the O 1s line intensity for a saturated NiO sample (1200 Langmuirs), measured experimentally by Saiki et al. [306]. The geometrical configuration regarding the x-ray angle of incidence and the photoelectron polar emission angles schematically shown in the inset. The angular distribution (circles) calculated by means of the

single-scattering cluster model for a 2-monolayer NiO film on a Ni substrate ((001) orientation) is seen to be in a good agreement with the experimental results. In particular, the theory correct-

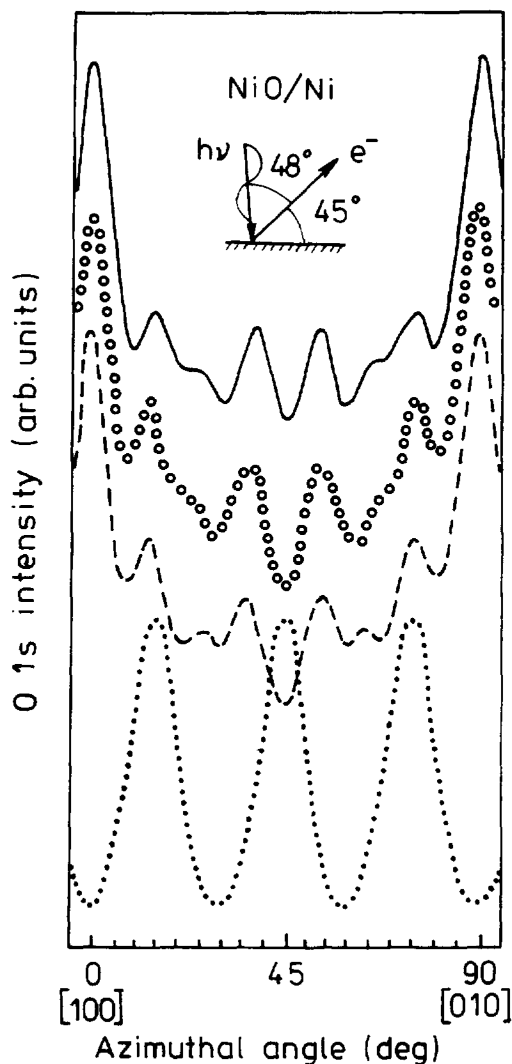

Fig. 26. The azimuthal dependence of the O 1s line intensity from a saturated nickel oxide formed at 1200 L exposure on Ni (001). The spectrum (solid curve) obtained for the x-ray angle of incidence 3° and the photoelectron polar emission angle 45° with the angular resolution of ±1.5°. Circles, dashed and dotted curves represent the results of calculations by the single-scattering cluster model for the structures: 2 ML NiO(001)/Ni(001), 3 ML NiO(001)/Ni(001) and 2 ML NiO(111)/Ni(001) [306].

ly predicts the doublet in the vicinity of the $\phi = 45°$ emission direction and dominant peaks due to forward scattering of photoelectrons along the directions indicated by arrows in Fig. 27.

Also shown for comparison are the results of calculations for an ideal NiO growing in either (001) (dashed curve) or (111) (dotted curve) orientation with 3- and 2-monolayer thickness, respectively. From the LEED data, the structure NiO(111)/Ni(001) is believed to coexist with NiO(001)/Ni(001) [1]. However, the dotted curve being in full disagreement with the experimental results indicates that the dominant orientation is NiO(001).

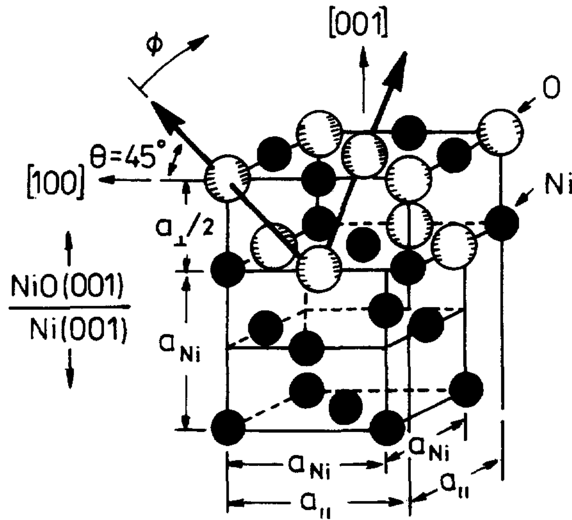

Fig. 27. Schematic representation of the 2 ML nickel oxide overlayer on a nickel (001) monocrystal substrate indicating the 16.7% expansion of the NiO lattice with respect to that of Ni and strain involved (after [306]).

In addition to signal Auger electron diffraction, one should mention effects associated with diffraction of a primary electron beam incident on a crystalline sample in a direction correlated with crystallographic axes, *i.e.*, at the angle close to the Bragg angle Θ_B . Coherent scattering of primary electrons results in appearance of waves propagating in the directions which differ from that of the incident beam by a combination of reciprocal vectors so that the intensities of different Bloch waves oscillate with depth [212]. The contrast of a Kikuchi pattern of backscattered electrons varies with orientation of the electron momentum with respect to close-packed atomic planes, in the vicinity of Bragg directions [210]. Since an Auger transition rate is proportional to the flux of primaries the number of Auger electrons generated in the near surface region becomes also dependent on the angle of incidence of bombarding particles. Mroz [18] points out that the two-wave approximation does not provide an adequate explanation of the observed

experimental results on Auger signal contrast. Therefore, usually, a multiple-wave approach is needed to describe quantitatively the redistribution of Auger electron intensity due to diffraction of the primary beam. More discussion on this point as well as analysis of relevant experimental data can be found elsewhere [18].

4. Backscattering of Primary Electrons

A. Total reflection coefficient

Primary electrons in the energy range from several hundred eV up to ten keV are widely used to excite core-shell Auger electrons. In this energy range, the probability of ionization of atoms with medium and large Z-numbers reaches its maximum values. Unlike x-rays, medium energy electrons are scattered intensively in a solid and a considerable amount of them may be reflected from a target. Therefore, a primary electron may cross the near surface region from which the majority of signal Auger electrons escape more than once. As a result, the number of ionization events increases and so does the amount of signal Auger-electrons leaving the sample. Moreover, if the energy of primaries exceeds the core-shell ionization threshold by a factor of 4–5 then the ionization cross section decreases with increasing energy and backscattered electrons excite a given Auger electron line more effectively due to their kinetic energy being smaller than that of bombarding particles. The influence of scattering of primary electrons on the intensity of the Auger electron line is described by the backscattering factor B. Prior to discussing how to evaluate the backscattering factor from first principles, it is advisable to briefly review available experimental data and to consider the physics of backscattering in more detail.

The probability for a fast electron to be reflected from a sample is characterized by the differential backscattering coefficient that is equal to the number of particles reflected from a unit area of the surface per unit time with certain momentum and energy, related to the number of electrons hitting a target. Integration of the differential backscattering coefficient yields the total reflection coefficient r which had been a subject of intensive experimental studies since early early days of AES [307–329]. If the energy loss of a backscattered electron exceeds a typical characteristic energy loss then this electron is usually referred to as being *reflected inelastically*. Inelastically backscattered primaries, as a rule, dominate the flux of emerging electrons. Therefore, the following discussion concentrates mainly on particles undergoing noticeable energy losses. From experimental studies, we know that the reflection probability at energies $E > Z^{4/3}e^2/a_0$ rises

monotonically with increasing the atomic number Z. Physically, the condition $E > Z^{4/3}e^2/a_0$ means that the velocity of the projectile is larger than the mean velocity of bound atomic electrons. In this energy range, starting on average from several keV, the quantity r is a slowly varying function of E. In particular, beginning from 10 keV the reflection coefficient r reaches a broad *plateau* for the majority of elements of periodic table and begins to decrease with E only in the relativistic region (*cf.* Fig. 28). The energy spectrum of inelastically backscattered electrons represents a dome-shape curve with a broad maximum. The position of the maximum is shifting closer to the initial energy of primaries while the peak becomes sharper as the Z-number increases. The contribution of elastically scattered electrons to the total yield does not exceed a few percent. The angular distribution of electrons backscattered from heavy materials at normal incidence follows, as a rule, a cosine law. At grazing incidence the angular distribution is stretched out significantly in the mirror direction with respect to the propagation direction of an incident beam.

The energy range $e^2/a_0 \ll E < Z^{4/3}e^2/a_0$, pertaining to energies from a hundred eV up to about several keV, is characterized by a general decrease in the reflection probability. The coefficient r is no longer a monotonic function of the serial number Z but may be considerably lower for heavy targets than that for light-element samples. The shape of the energy spectrum changes significantly: there is a sharp maximum at the kinetic energy almost equal to the initial one. This is a clear indication to a more pronounced role of elastically and quasielastically scattered primaries. The relative number of fast electrons that have suffered large energy losses decreases. Simultaneously, the lower energy *tail* of the total energy spectrum becomes more *populated* with true secondaries. These features are due to increasing the probabilities of large-angle scattering and inelastic energy losses. Note that the inelastic mean free path reaches its minimum value at energies about 50–100 eV (*cf.* Section 2E).

In earlier theories of electron backscattering, two main approaches dominated. Everhart [330] applied a single deflection model assuming that the flux of backscattered particles consists primarily of those suffered one elastic collision at small impact parameter. The attempts to incorporate small-angle scattering effect into the Evehart theory was later made by Dashen [331] and Kalashnikov and Mashinin [332,333]. The results found in ref. [330–333] have a common drawback: they predict an infinite increase in the reflection probability as the atomic number Z tends to infinity. Nonetheless, the single deflection model proved to be effective in the case of low-Z targets, where its basic assumptions are satisfied.

Another model was developed by Archard [334] and Tomplin [335]. They proposed a diffusion-

like picture according to which an electron moves in a solid along a straight line. When the traveled pathlength reaches the value of the so-called diffusion length all the particles are supposed to diffuse in all directions, *i.e.* scattered multiply at arbitrary angles. In the diffusion model the total reflection coefficient at normal incidence can never exceed the value of 0.5, which is a direct corollary of the unsatisfactory simplifying assumptions and contradicts the physics of the reflection process. The theory of Archard and Tomlin did relatively well, in the case of heavy targets, but failed to provide reasonable results for light elements.

Most consistently the problem of backscattering can be treated on the basis of kinetic equation with appropriate boundary conditions. Tilinin [336,337] applied the Boltzmann type kinetic equation in the transport approximation to the case of normal incidence and found that the reflection coefficient is a universal function of the ratio

$$\sigma = R_0/\lambda_{tr}, \tag{4.1}$$

where R_0 and λ_0 are the linear range and the transport mean free path. The quantity R_0 represents the total pathlength traveled by an electron before being slowed down and is given by

$$R_0 = \int dE/ < dE/ds >, \tag{4.2}$$

$< dE/ds >$ being the stopping power of the target. The lower and the upper limits of integration in (4.2) are set equal to $E_{min} \sim 50$ eV, in accordance with conventional separation of fast and slow electrons [209], and to $E_{max} = E_0$, where E_0 is the initial energy, respectively. If the velocity of primary electrons is large compared to the average velocity of atomic electrons, the stopping power $< dE/ds >$ is mainly due to ionization energy losses and is determined by [338]

$$< dE/ds >= (2\pi MZr_e^2)[(E+1)^2/E(E+2)]L_i(E,Z), \tag{4.3}$$

where the function $L_i(E,Z)$ varies slowly with energy and reads

$$L_i(E,Z) = \ln[E^2(E+2)/2J] + (E+1)^{-1} + [E/(E+1)]^2/8 - [(2E+1)/(E+1)^2]\ln 2. \tag{4.4}$$

In (4.3) and (4.4), $r_e = e^2/mc^2$ is the classical electron radius, the energy E is in units mc^2 and J is the average ionization potential, $J(Z) \sim 10Z$ eV. In the nonrelativistic limiting case, we obtain from Eq.(4.3) the renowned *Bethe-Bloch* formula

$$< dE/ds >= (2\pi MZe^2/E)L_i(E,Z), \qquad v \ll c \tag{4.5}$$

where the energy E is in usual units and

$$L_i(E,Z) = \ln(1.16E/J). \tag{4.6}$$

Substituting (4.3) into (4.2) and neglecting for simplicity the weak dependence of the function L_i on energy yields the approximate expression for the linear range $R_0 \sim E^2/[4\pi Ze^2 L_i(E,Z)]$. By making use for explicit expressions for the momentum transfer cross sections found in ref. [126] we arrive at the formula for the scattering parameter

$$\sigma = [(Z+1)/4]f(E,Z), \tag{4.7}$$

where

$$f(E,Z) = [l_i(E,Z)]^{-1} \begin{cases} \ln[1.08(v/Z^{2/3}v_0)^2] & \text{for} \quad Z^{2/3} < v/v_0 < Z \\ \ln[1.08(v/Z^{2/3}v_0)\,] & \text{for} \quad v/v_0 > Z. \end{cases} \tag{4.8}$$

Note that the prefactor Z in the right-hand side of (4.7) is replaced by $Z+1$ to account for angular deflections in inelastic collisions of electron with atoms [339]. The function $f(E,Z)$ is equal to the ratio of two logarithmic functions and, thereby, its dependence on the energy and atomic number is pronounced very weakly. Thus, we conclude that at relatively low energies the parameter σ is linear proportional to $Z+1$ and the reflection coefficient depend only on the serial number Z of the target.

The quantity $f(E,Z)$ in (4.7) is of the order of unity. As a result, the parameter $\sigma \sim (Z+1)/4$ and exceeds unity for the majority of elements of the periodic table. Since the linear range and the transport mean free path represent the energy and the momentum relaxation lengths, respectively, the parameter σs can be interpreted as the number of large angle scattering events an electron suffers before completely loosing its kinetic energy. From the physical point of view the parameter σ characterizes the behaviour of electron trajectories in a solid. Small values of $\sigma \ll 1$ correspond to motion along a straight line as the probability of large-angle scattering is negligible. In the limiting case of large $\sigma \gg 1$ electron trajectories deviate significantly from straight lines and the traveled pathlength can exceed noticeably the penetration depth. In Table 3, the values of the parameter σ for Al, Cu, Ag and Au are presented for energies ranging from 500 eV up to 10 000 eV. The transport mean free path is calculated from the quasiclassical expression by Tilinin [126] and the linear range is obtained by numerical integration of the right-hand side of (4.2) by making use the stopping-power data found in ref. [340] on he basis of the dielectric function theory. From the Table 3 it follows that, typically, $\sigma \geq 2-8$. Consequently, a primary electron may experience several large-angle scatterings before escaping from or being stopped in a solid. Under the assumption that the contribution of fast true secondaries to the backscattering probability is neglected [208,221]

$$r = [(\sigma+1)^{1/2} - 1]/[(\sigma+1)^{1/2} + h], \qquad h = 1.908. \tag{4.9}$$

The results of calculations of refs. [336,337] are shown in Fig. 28 by the solid curves. It is seen that the analytical solution in the transport approximation is in good agreement with the experimental

TABLE 3. Energy Dependence of the Linear Range R_0 , Transport Mean Free Path $\lambda_{tr}(10^{-6}$ cm) and Scattering
Parameter $\sigma = R_0/l_{tr}$ of Fast Electrons in Different Materials.

Energy	Al			Cu			Ag			Au		
(eV)	R_0	λ_{tr}	σ	R_0	λ_{tr}	σ	R_0	λ_{tr}	σ	R_0	λ_{tr}	σ
500	1.06	0.48	2.2	0.65	0.19	3.4	0.67	0.19	3.6	0.56		
600	1.38	0.62	2.2	0.81	0.23	3.6	0.82	0.22	3.8	0.73		
800	2.10	0.90	2.3	1.16	0.30	3.9	1.18	0.28	4.2	1.05	0.21	5.1
1000	3.14	1.42	2.2	1.54	0.38	4.1	1.58	0.33	4.8	1.39	0.25	5.6
1500	5.80	2.70	2.2	2.59	0.62	4.2	2.79	0.54	5.2	2.39	0.36	6.6
2000	8.81	4.13	2.1	3.82	0.91	4.2	4.01	0.75	5.3	3.41	0.48	7.1
3000	16.9	7.70	2.1	7.31	1.70	4.3	7.52	1.24	6.1	5.93	0.75	7.9
4000	27.5	12.9	2.1	11.6	2.65	4.4	12.1	1.87	6.5	8.67	1.08	8.0
5000	40.0	19.0	2.1	17.3	3.82	4.5	17.4	2.60	6.7	12.2	1.46	9.0
6000	56.4	26.9	2.1	23.1	4.98	4.6	23.1	3.40	6.8	16.0	1.88	9.0
8000	90.1	43.1	2.1	37.4	7.86	4.8	37.4	5.40	6.9	27.1	2.75	9.9
10000	131	62.6	2.1	53.0	11.3	5.0	53.1	7.40	7.2	40.9	3.44	12

data. The criterion of validity of this approximation as applied to the case of electron inelastic backscattering is the condition $\sigma > 1$, which means that the flux of electrons suffered large energy losses is noticeably isotropized, so that its angular dependence becomes weakly pronounced. Note, that the contribution of fast true secondary electrons r_s may influence noticeably the electron yield in the keV-energy region [337]. Figure 29 displays the energy dependence of the ratio r_s/r for copper and gold. It is seen that the quantity r_s reaches its maximum value at the energy $\sim$ 0.5 keV for a Cu and 1.0 keV for Au target.

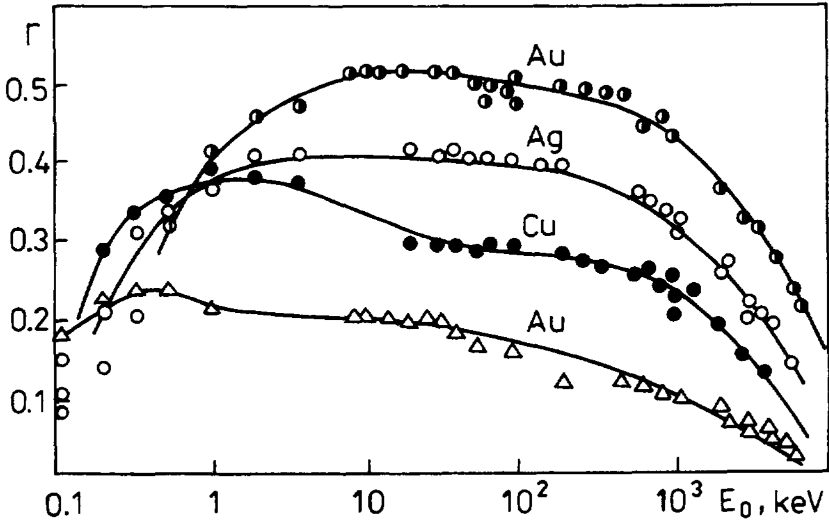

Fig. 28. The energy dependence of the inelastic backscattering coefficient of fast electrons normally incident on different targets. Experimental data [209,307–329]: open triangles – Al, black circles – Cu, open circles – Ag, half filled circles – Au. Solid curves – theory (after ref. [208])

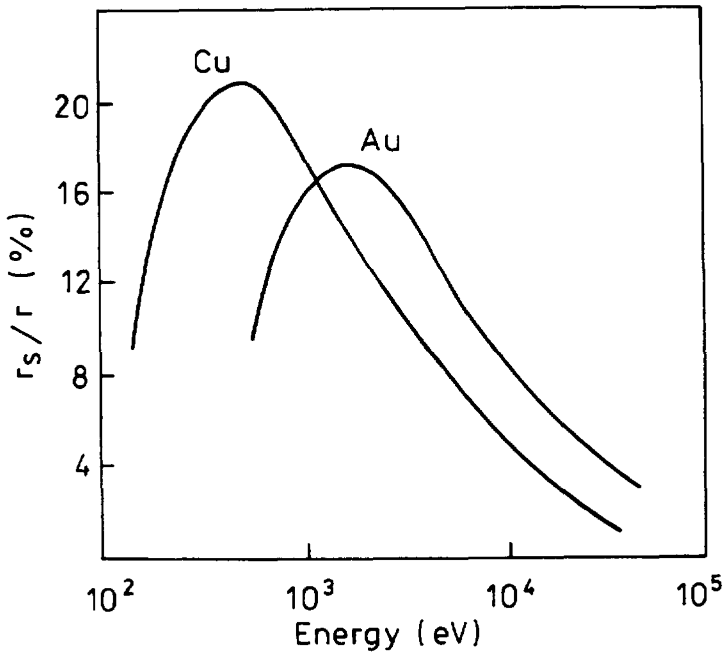

Fig. 29. Relative contribution of fast true secondary electrons to the total backscattering coefficient versus the energy of bombarding electrons (after ref. [221]).

In the more general case of oblique incidence, the backscattering probability is determined by the so-called *reflection parameter* [341,342]

$$\sigma^* = \sigma(1 - \sin\vartheta_0)^{-1}, \tag{4.10}$$

where ϑ_0 is the incidence angle of the primary beam of particles, counted from the surface normal. By its physical meaning the quantity σ^* represents an average number of scattering events accompanied by deflection at the angle necessary to escape from a target, an electron may experience at the pathlength R_0 . The larger the reflection parameter is the higher the reflection probability. For $\sigma^* \gg 1$, reflection is always a multiple scattering process and a simple single-deflection model is inadequate to describe electron backscattering. In the opposite case of small values of $\sigma^* \ll 1$, the probability to be backscattered is negligible and is due primarily to rare collisions leading to deflection at a large angle. The parameter σ^* plays an important role in the reflection phenomenon. It determines not only the total number of reflected particles, but also the shape of the angular and energy distributions. In particular, at large σ^*-values the peak height of the energy spectrum of inelastically scattered electrons is proportional to σ^*, while the most probable energy loss of backscattered particles is inverse proportional to σ^* [341,342].

The total reflection coefficient as a function of the angle of incidence is described by [341,346,347]

$$r = r_s + (1 - r_s)r_d, \tag{4.11}$$

where r_s and r_d are the relative amounts of electrons traveled in the sample the pathlengths $s < \lambda_{tr}$ and $s > \lambda_{tr}$ and reflected from the target, due to small-angle and diffuse scattering, respectively. It is assumed that electrons traveled a pathlength $s < \lambda_{tr}$ in a sample are scattered mainly at small angles while those traveled a pathlength $s > \lambda_{tr}$ have suffered diffuse scattering. The quantity r_s can be found in the small-angle diffusion approximation [343,348] and reads [347]

$$r_s = \begin{cases} w[(1 - \sin\vartheta_0)], & \text{for } \sigma > 1, \\ w(\sigma^*), & \text{for } \sigma > 1, \end{cases} \tag{4.12}$$

where

$$w(x) = \begin{cases} (1/2)\mathrm{erfc}[(3/x)^{1/2}], & \text{for } x \leq 12, \\ 1 - 1.5x^{-1/4} + 1.2x^{-5/4}, & \text{for } x \geq 12. \end{cases} \tag{4.13}$$

The quantity r_d is obtained by generalization of result (4.9) for the case of oblique incidence [343,347]

$$r_d = [(\sigma + 1)^{1/2} - 1]/[(\sigma + 1)^{1/2} + h\cos\vartheta_0]. \tag{4.14}$$

Figure 30 shows the total reflection coefficient r of 25 keV electrons as a function of the incidence angle, the symbols representing the experimental data of ref. [374]. Predictions of (4.11) are displayed by dashed curves. Solid lines are the results of numerical solution of the kinetic equation by a super matrix algorithm [218]. Formula (4.11) describes quite well the behaviour of experimental points even in the case of a beryllium target, and is in agreement with the results obtained by both MC simulations and the numerical solution of the Boltzmann equation.

B. Electron backscattering from targets of complex chemical composition

The reflection theory developed for one-element samples can be generalized for the case of a target consisting of N different species of atoms with relative concentrations c_k ($k = 1, 2, ..., N$) [221,348]. To show this, we note that inelastic energy losses and elastic scattering of sufficiently fast electrons ($E > Z^{4/3}e^2/a_0$) are dominated by close collisions with the impact parameter $b \leq a_0$, which allows the stopping power $< dE/ds >$ and the transport mean free path λ_{tr} to be expressed in terms of concentrations c_k, the stopping powers and transport mean free paths of pure elements. We denote the latter quantities by $< dE/ds >_k$ and $\lambda_{tr,k}$, respectively. The wave length of fast electrons is small compared to the average interatomic distance d, so that $kd \gg 1$, where k is the electron momentum in units of the Planck constant. From this, it follows that interference of secondary waves emitted by neighbouring atoms can be neglected, when calculating the differential elastic and inelastic scattering cross sections. Consequently, the transport mean free path and the stopping power of a multiple-component target read

$$\lambda_{tr} = (M \sum_{k=1}^{N} c_k / M_k \lambda_{tr,k})^{-1}, \tag{4.15}$$

$$< dE/ds >= M \sum_{k=1}^{N} c_k M_k^{-1} < dE/ds >_k, \tag{4.16}$$

M_k being the bulk density of a pure element k. Expression (4.16) represents the well-known *Bragg rule* for the energy losses of a swift charge in a polyatomic medium [349,350]. In the nonrelativistic case, the scattering parameter pertaining to the N-element sample is given by the relationship (*cf.* (4.7))

$$\sigma = (1/4) \sum_{k=1}^{N} c_k Z_k (Z_k + 1) f(E, Z_k) L_i(E, Z_k) \left[\sum_{k=1}^{N} c_k Z_k L_i(E, Z_k) \right]^{-1}, \tag{4.17}$$

where the functions $f(E, Z)$ and $L_i(E, Z)$ are defined by (4.8) and (4.6), respectively. Neglecting the weak dependence of the functions f and L_i on atomic number, we present the scattering

parameter σ in the form

$$\sigma = [(Z_{eff} + 1)/4] f(E, Z_{eff}), \tag{4.18}$$

where Z_{eff} is the effective atomic number of the target, *i.e.*,

$$Z_{eff} = \sum_{k=1}^{N} c_k Z_{eff}^2 \left(\sum_{k=1}^{N} c_k Z_{eff} \right)^{-1} . \tag{4.19}$$

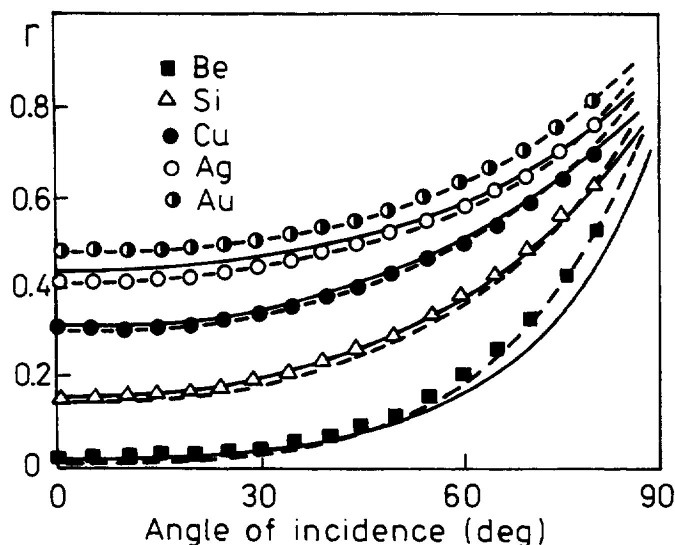

Fig. 30. Dependence of the total reflection coefficient r on the incidence angle of bombarding electrons. Symbols are the experimental data of ref. [347], Solid curves – numerical solution of the Boltzmann kinetic equation by a supermatrix algorithm [218]. Dashed lines – calculations from formula (4.11).

It is worth noting that a number of different formulas for the effective Z-number have been proposed in the literature [351–353]. Expression (4.19) coincides with the empirical formula of Sadlick and Allen [351] and provides the best quantitative interpretation of experimental data [354]. One should keep in mind, however, that the effective Z-number is, generally, a function of not only relative concentrations and atomic numbers of pure elements but also energy. Therefore, the backscattering probability is described more consistently in terms of the parameter σ rather than Z_{eff}.

In Fig. 31, the experimental data of ref. [355] for the reflection coefficient r of 20 keV electrons normally incident on targets of complex chemical composition are shown by triangles. Also presented for comparison is the theoretical curve obtained from (4.14) for the scattering parameter defined by (4.17).

4.3 Backscattering factor in AES

The backscattering factor B is defined as a ratio of an actual number of core-shell ionization events induced by a primary beam to the number of those events which would occur if both elastic scattering and slowing down of bombarding electrons were neglected. The quantity B can be either larger or smaller than unity. In this connection, the term *scattering factor* would be more appropriate. However, we shall use below the term *backscattering factor* as it has been established in literature since early applications of AES. A number of empirical expressions has been proposed to calculate the factor B [356–358]. This quantity can be also obtained by Monte Carlo technique [353,359]. For instance Shimizu [357] proposed the following formula for the backscattering factor

$$B = 1 + (2.34 - 2.10Z^{0.14})(E_{nl}/E_p)^{0.35} + 2.58Z^{0.14} - 2.98, \quad (4.20)$$

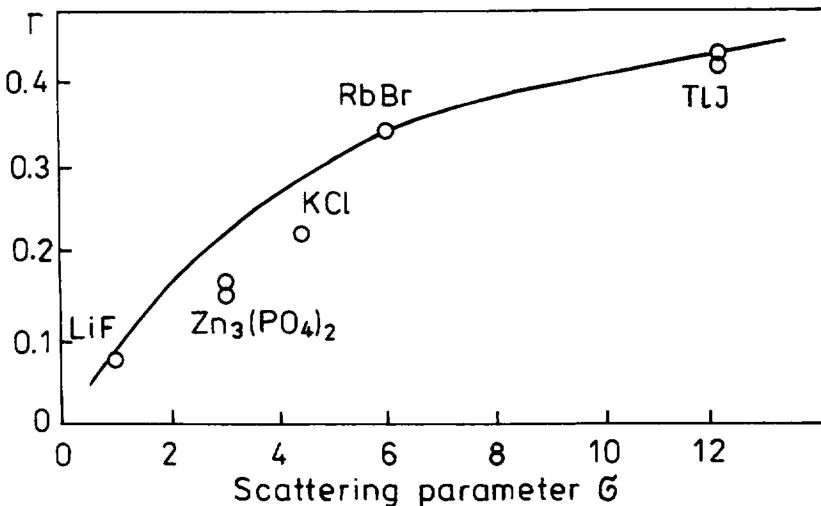

Fig. 31. Dependence of the reflection coefficient r of 20-keV electrons on the scattering parameter σ for targets of complex chemical composition. Normal incidence. Open triangles – experimental data of ref. [355]. Solid curve – calculations from formulas (4.14) and (4.17).

where E_p and E_{nl} are the kinetic energy of primary electrons and the ionization energy, respectively. Empirical relationships may be useful for rapid assessments of the quantity B, but they provide little insight, if at all, into the physics of electron-solid interaction. It is seen, particularly, from (4.20), that the backscattering factor increases infinitely as the serial number Z tends to ∞. Clearly, such a behaviour of the quantity B is not expected on physical grounds.

The mean escape depth of signal Auger electrons is small compared to the transport mean free

path of primaries. Consequently, elastic scattering of bombarding electrons in the near surface region, where the majority of signal electrons is generated, may be ignored. Suppose also that the kinetic energy of primaries E_p satisfies the condition

$$E_p - E_{nl} \gg < dE_p/ds > \lambda_i, \tag{4.21}$$

where λ_i is the inelastic mean free path of signal Auger electrons. Inequality (4.1) means that the energy losses of primary electrons in the near surface layer of the thickness λ_i are negligible. Under these assumptions, the backscattering factor reads [360,361]

$$B = 1 + \mu_0 \int_{E_{nl}}^{E_p} q(E)dE \int_0^1 R(\mu, E)d\mu/\mu, \tag{4.22}$$

where $R(\mu, E)$ is the differential backscattering coefficient describing the probability for an incident electron to be reflected at the polar angle $\vartheta = \arccos\mu$ measured from the surface normal with the energy $E, \mu_0 = \cos\vartheta_0$ is the cosine of the angle of incidence and $q(E)$ is the reduced ionization cross section of the nl-orbital, namely,

$$q(E) = \sigma_{nl}(E)/\sigma_{nl}(E_p). \tag{4.23}$$

Calculations of the integrals entering the right-hand side of (4.22) requires knowledge of the energy dependence of the ionization cross section and the differential backscattering coefficient as a function of emission angle and energy. In the case of K-shells, variation of the ionization cross section with energy may be approximated with an accuracy of 15% by the expression [362]

$$\sigma_K(E) = \text{const } \ln(E/E_K)/(E/E_K), \tag{4.24}$$

which is quite consistent with corresponding quantum-mechanical calculations (*cf.* Section 2A) [363]. A similar dependence is expected for L-shells. Since, the backscattering factor is determined by the ratio of $\sigma_{nl}(E)/\sigma_{nl}(E_p)$, one may suggest that the error introduced into calculation of the quantity B by making use of (4.5) is rather small. The distribution $R(\mu, E)$ can be either measured experimentally [356,357] or obtained theoretically [336]. In particular, for electrons normally incident on a target an analytical expression for $R(\mu, E)$ has been found in ref. [337] in the transport approximation

$$\begin{aligned} R(\mu, E) &= (4\pi i R_0 < dE/ds >)^{-1}\mu(1+\mu)^{-1} \int_{c-i\infty}^{c+i\infty} \omega(p) H[1, \omega(p)] \cdot \\ &\cdot H[\mu, \omega(p)]\Phi_L(p)\rho(E)]^{-p}dp, \qquad c > 1 \end{aligned} \tag{4.25}$$

where $H(\mu, \omega)$ is the H-function of Chandrasekhar [268], $\omega(p)$ is the complex single scattering albedo

$$\omega(p) = \sigma/(\sigma + p), \tag{4.26}$$

$\sigma = R_0/l_{tr}$ is the ratio of the linear range to the transport mean free path of primaries (*cf.* Section 4A), $\rho(E) = R_0(E)/R_0(E_p)$ is the reduced residual range of primaries and the function $\Phi_L(p)$ is the Laplace transform of the energy-loss function of Landau [278] for electrons travelled in a medium a pathlength l_{tr}. In the limiting case of large values of the parameter $\sigma \gg 1$ and overvoltage $U_{nl} = E/E_{nl} \gg 1$ substitution of (4.25) into (4.22) yields a simple expression for the backscattering factor [361,364], *viz.*,

$$B = (1+h)/\{1+h\,[(\alpha-1)/[\alpha(\sigma+1)-1]]^{1/2}\}, \qquad U_{nl} \gg 1, \tag{4.27}$$

where h is defined by (4.9) and α is the parameter governing the energy dependence of the linear range $R_0 \sim E^{\alpha}$ ($\alpha = 1.5 - 1.7$ [209]). Formula (4.27) is in good agreement with data obtained by MC simulations [353] and semiempirical results [356–358]. For instance, for 2.0-keV electrons reflected from Cu, Ag and Au, the backscattering factor, according to (4.27), is equal to 1.92, 1.99 and 2.07, respectively. While a semiempirical expression of Shimizu [357] yields for the same targets the values 1.84, 2.05 and 2.35 at the overvoltage $U \sim 20$.

Analysis of (4.22) and (4.25) shows that the backscattering factor B increases with the scattering parameter σ and the overvoltage U_{nl}. The quantity B reaches its saturation value $B_m = 2.908$, as it follows from (4.27), in the limiting case $\sigma = \infty, U_{nl} = \infty$. This saturation value is close to that predicted by formula (4.20), $B_m = 2.936$, for $U_{nl} = \infty$ and $Z = 100$. For $U_{nl} \geq 4$, the energy dependence of the backscattering factor is weakly pronounced. In the near threshold region, $U_{nl} \leq 1.5$ the contribution of reflected electrons to excitation of a given Auger electron line reduces drastically. Owing to a rapid decrease in the number of backscattered primaries capable of ionizing the nl-orbital. At the energies just above the threshold, $U_{nl} - 1 \ll (\alpha\sigma)^{-1}$, the flux of outgoing electrons retaining a sufficient amount of kinetic energy is mainly due to rare violent collisions and, thereby, the transport approximation becomes inadequate to describe the reflection process. It should be stressed, however, that in the vicinity of the threshold, (4.22) is formally invalid, since it does not take into account slowing down of primaries in the near surface region, which provides the major contribution to the Auger electron line intensity. Another point that should be kept in mind is that (4.25) does not include the contribution of fast true secondaries.

In Fig. 32, the backscattering factor B is shown versus the overvoltage U for the case of electrons normally incident on Si and Au targets and K-shell excitation. The solid curves are the results of calculation in the transport approximation ((4.22) and (4.25)) [361]. Open circles and

triangles are the experimental values from ref. [365].

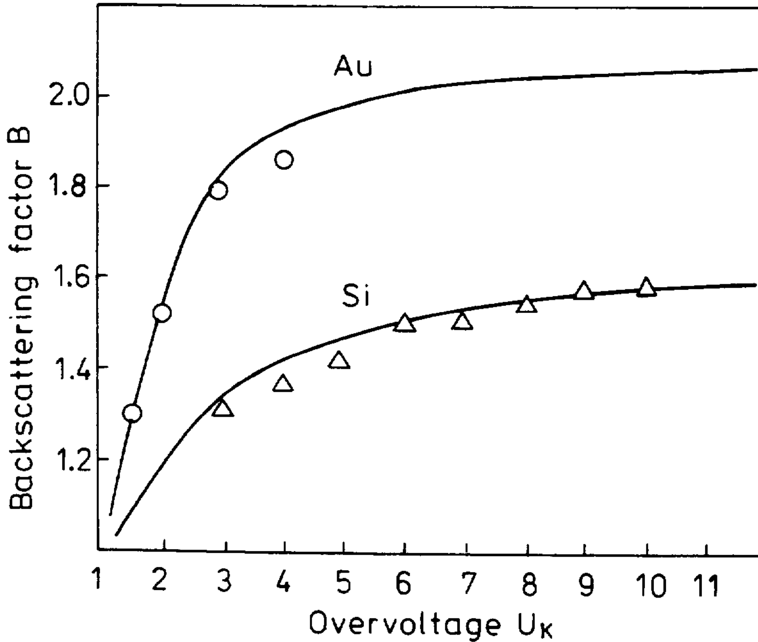

Fig. 32. The dependence of the backscattering factor B on the overvoltage for K-shell excitation of Si and Au. The primary electrons are normally incident on the sample. Solid curves – calculations in the transport approximation [361]. Open triangles and circles are the experimental data of ref. [365] for Si and Au, respectively.

TABLE 4. The Dependence of the Ratio of the Backscattering Factors B_{Me}/B_{Si} on the Energy of Bombarding Electrons [361].

		B_{Me}/B_{Si}	
E_p, keV	Metal	experiment [366]	theory [361]
3	Ta	1.27	1.20
5	Ge	1.17	1.17
	Mo	1.20	1.19
	Ta	1.30	1.30
10	Ge	1.18	1.19
	Mo	1.20	1.21
	Ta	1.34	1.31

Meda and Queirollo [366] measured the ratio of backscattering factors of Ge, Mo and Ta targets covered by a thin Si overlayer to the backscattering factor of a pure Si sample. The K-shell of Si atoms was excited for all overlayer substrate combinations. Their results are compared with those found in the TA [361] (*cf.* Table 4). The experimental data are seen to be in perfect agreement with the theory. The maximum discrepancy of about 6% is observed for 3 keV electrons and the Ta-substrate.

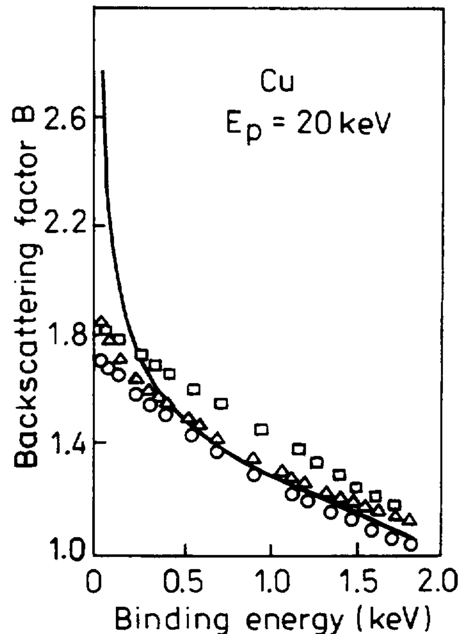

Fig. 33. The backscattering factor of a Cu target as a function of the binding energy. Primary electrons of the energy 2000 eV are normally incident on the target. Solid curve – experimental results of ref. [367], open circles, triangles and squares are the data obtained from empirical expressions of Love [356], Shimizu [357] and Reuter [358] (after ref. [367]).

An interesting effect was observed in experiments by Palczynski et al. [367]. They studied the ionization-energy dependence of the backscattering factor for Cu, Ag, Au targets and Cu-Ag-Au alloys in the primary-energy range from 1000 to 2000 eV. These authors measured the energy spectrum of reflected particles and under the assumption of a cosinusoidal angular distribution performed numerical integration in the right-hand side of (4.22) by making use of the Gryzinski formula [24] for ionization cross section. They found the backscattering factor at ionization energies of about 100 eV and less to be much larger than that reported in literature for similar values of the overvoltage. Their results for a copper target are displayed in Fig. 33 as a solid curve. Also presented here are the backscattering factors calculated from semiempirical expressions of

refs. [356–358]. It is seen that the experimental values of Palczinski et al. compare well with the predictions of ref. [356–358] at relatively low overvoltage $U_{nl} \leq 6$. On the other hand, the factor B obtained in ref. [367] increases rapidly as the ionization energy becomes smaller than 200 eV. A similar, and even more pronounced increase in the backscattering factor was measured for Ag and Au targets as well as for alloys. Palczynski et al. ascribe such a behaviour of the backscattering factor to the approximations made when processing experimental data. Particularly, the angular and energy distributions of reflected particles was assumed to split into a product of two functions depending separately on angular and energy variables. The angular distribution was believed to be cosinusoidal and the *Gryzinski formula* [24] was used to describe the ionization probability. However, the expression of Gryzinski for the ionization cross section is expected to provide reasonable results at such overvoltages and cannot lead to 50–100% increase in the factor B as observed in ref. [367] for Cu, Ag and Au samples. The assumption of the cosine-shape of the angular distribution is well substantiated by numerous experimental data and theoretical studies (*cf.* (4.25)) although this distribution may deviate slightly from the cosine law. Thus, the reason for large values of the quantity B is definitely different from those discussed in ref. [367]. Most probably the high values of B at low ionization energies are explained by the influence of fast true secondary electrons on the Auger electron current intensity. In ref. [337], it has been shown that contribution of fast true secondaries can amount to 30% at energies of about 1–2 keV in the case of elements $Z \geq 30$. The average energy of fast true secondaries is about one quarter of the initial energy of primaries and, in the situation considered, falls into the energy region where the ionization cross section reaches maximum values, which means the true secondaries excite low-binding-energy shells very effectively. Assessments based on the results of ref. [337] show that, under these specific conditions, true secondaries may be responsible for 30-50% of all signal Auger electrons.

5. Applications of AES/XPS to Surface Analysis

A. Methods of inelastic background removal

Each characteristic peak in the energy distribution of Auger or photoelectrons is accompanied by a broad background. A true spectrum may be presented as a difference between the measured energy distribution and the background. Therefore, any operator has to decide how to determine the peak area pertaining to electrons that escape from a sample without energy losses and, thereby,

carrying direct quantitative information about chemical composition of the near surface region. The background is caused by electrons that have undergone multiple inelastic scattering. Those electrons also experience elastic collisions on the way out of the target. Consequently, the low-energy tail of the peak, generally, is a function of elastic and inelastic properties of the sample. In addition, the shape of the spectrum depends on the initial angular distribution of signal electrons as elastic interaction tends to redistribute the particles over the emission directions.

In the past, the problem of inelastic background subtraction was addressed by a number of authors [368–373]. Shirley [368] seemed to be the first to notice that the background intensity was proportional to the integrated peak intensity at higher energy. This assumption is physically quite clear, as the recorded spectrum may be always presented as consisting of two parts. One of them corresponds to particles escaping without losing any amount of their kinetic energy (phonon scattering is neglected in view of a relatively large resolution of analysers) and, thereby is proportional to the intrinsic spectrum. The other corresponds to electrons that have scattered inelastically several times before leaving a solid. Thus, the deconvolution formula of Shirley represents an integral equation with an unknown prefactor and the measured intensity as an integrand in the integral term. The prefactor is determined, in such a way, that at a certain minimal energy (to be chosen by an operator) the found intrinsic spectrum becomes zero.

If the background varies slowly in the vicinity of the peak and no plasmon peaks are visible, even, more simplified procedure is often applied, which is called a *straight-line method* [15]. In the latter case, the background is approximated by a straight line beginning from a certain E_{min} in the low-energy party of the spectrum and ending at E_{max}. The energy E_{max} is usually chosen a few eV above the initial energy of signal electrons. Hence, this method differs from that of Shirley in that no assumption is made about the proportionality of the background to the peak intensity.

Tougaard and Sigmund [372] found a deconvolution equation in the straight line approximation and showed that the inelastic background intensity is determined by a convolution of the measured spectrum and the differential, inverse inelastic mean free path. Later, Tougaard [373] proposed a deconvolution formula, where elastic scattering was accounted for in the P_1-approximation, and the universal differential inverse inelastic mean free path [277] was recommended for practical calculations. This formula contains a fitting parameter to be varied to fulfill the criterion that the intrinsic spectrum vanishes beginning from a certain energy in the low-energy part of the spectrum. A number of authors have applied this formula in the peak-shape analysis [374–378]. The Tougaard method was tested and compared with the results obtained by the approach of

Shirley and the straight line method for three sets of polycrystalline alloys [379]. It was found that for peaks from the same solid the root mean squared deviation of experimentally determined peak intensity ratios from those calculated theoretically was about 35% in the case of the both Shirley and straight line methods and only 11% for Tougaard's method [379]. The Shirley and straight line methods were found to be much more accurate when reference spectra were used yet the corresponding results deviate by about 10environment-induced changes in shake-up/off processes may result in systematic errors with the Shirley and straight line methods while the deconvolution algorithm of Tougaard is much more stable to those changes. In general, the method of Tougaard seems to be superior. However, there are several weak points in the Tougaard approach. First, a fitting procedure is to be performed to obtain the intrinsic spectrum and this may introduce some uncertainty into the final results. Secondly, the influence of elastic collisions is accounted for approximately and the angular distribution of the emerging flux of electrons is supposed to be cosinusoidal. Thirdly, the correlation between anisotropy of photoemission (in the case of XPS spectra) and multiple scattering of electrons is ignored. Finally, surface excitations are not accounted for at all. The latter effect may be quite significant as shown recently by Chen [197].

Making use of the analytic solution to the secondary emission problem in the transport approximation Tilinin and Werner [241] derived the deconvolution formula

$$F(E) = y(\mu, E) - \lambda_i k(\mu) \int_E^\infty dE' w(E_0 \mid E' - E) y(\mu, E'), \tag{5.1}$$

where $F(E)$ is the initial energy distribution and $y(\mu, E)$ is the measured spectrum. Equation (5.1) differs from the result obtained by Sigmund and Tougaard [372] by an additional prefactor $k(\mu)$ before the integral term. On the other hand, Eq. (5.1) reduces to a modified deconvolution formula of Tougaard [277] if one replaces the function $k(\mu)$ by the constant $\lambda_i/(\lambda_i + L)$, where L is the so-called *characteristic length* of the order of $2\lambda_{tr}$ [272]. Result (5.1) is obtained from the exact solution to the boundary value problem for initially isotropic emission (the asymmetry parameter $\beta = 0$) and is expected to account more accurately for the elastic scattering effect. In this connection, it is interesting to compare the results of the background subtraction procedures based on (1.1) and the Tougaard approach. Such a comparison was performed in ref. [241] and is illustrated in Fig. 34. The model Auger electron spectra were calculated for 1000 eV electrons in silver for the normal ($\alpha = 0°$) emission by applying the universal energy-loss function of Tougaard [277]. The intrinsic energy spectrum was assumed to be the same as in Fig. 20. One can see that the Tougaard method slightly underestimates the inelastic background, whereas deconvolution formula (5.1) consistently removes the contribution of inelastically scattered electrons and yields

practically the initial energy spectrum over a wide energy range.

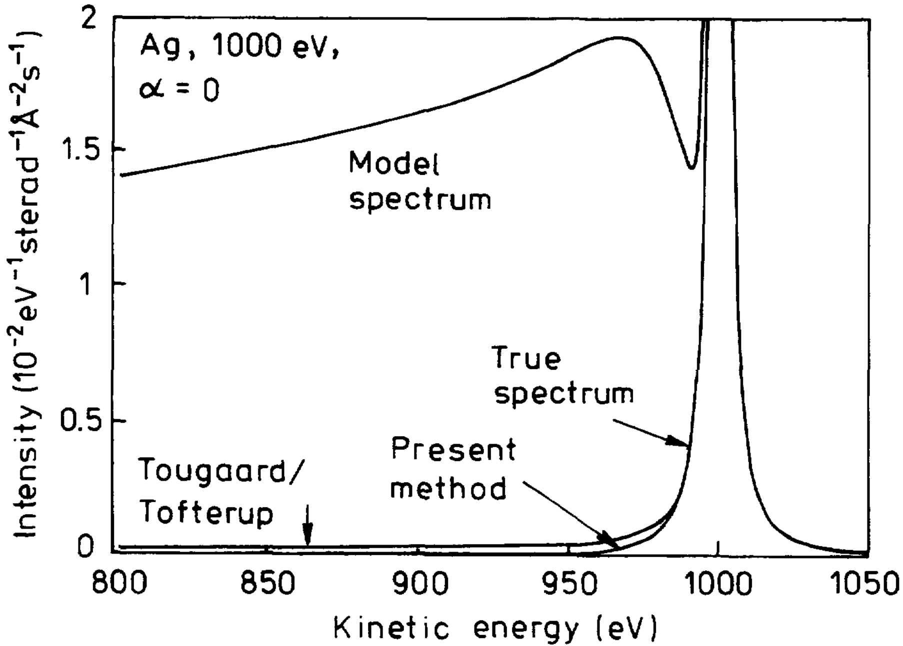

Fig. 34. Verification of the background subtraction technique proposed in ref. [241] and comparison with the method of Tougaard (Eq. (41) of ref. [277]). The model energy spectra in the vicinity of the characteristic peak of 1000 eV Auger electrons in silver are calculated for normal emission. Note, that Eq. (5.1) yields the exact true spectrum, while the Tougaard method under- or overestimates the background depending on the emission angle α (after ref. [241]).

Upon integration of both sides of (5.1) with respect to energy one obtains the integral equation relating the excitation rate of signal electrons, the measured spectrum and the differential inelastic scattering cross section. The function $w(E_0 \mid \varepsilon)$ appears in the integrand of a double integral on energy. From this it follows that the resulting excitation rate is not too sensitive to the actual shape of the differential inverse inelastic mean free path. This explains the results of Jansson et al. [380] who found that for metals the REELS and universal differential inelastic scattering cross sections give peak intensity ratios that were equally close to the theoretically expected values.

Recently, Werner [381] developed an algorithm to subtract the inelastic background in the case of anisotropic photoemission. His method is based on a solution of the transport problem and involves a recursive deconvolution scheme. For the asymmetry parameter $\beta = 0$, his results reduce to those of Tilinin and Werner [241]. Werner found that the Tougaard method worked reasonably well only in the case of the magic angle geometry. For other geometries, neglect of photoemission anisotropy in Tougaaard's approach leads to quite severe discrepancies in the angular and energy

distribution [381].

A different approach to deal with the problem of background removal was proposed by Jo [382]. He noted that the integral term in the right-hand side of (5.1) is proportional to the response of inelastically scattered electrons. This response is well known in the energy loss region, where the peak contribution clearly disappears. Thus, a task of finding the energy-loss function and, thereby, the intrinsic spectrum, reduces to a kind of inverse problem similar to the restoration of a degraded image. Jo introduced physically reasonable optimization conditions and applied a minimization procedure [383,384] to solve the integral equation relating the response and the differential inelastic scattering cross section. By making use of experimental data for Al and Au from the spectrum data bank in the Common Data Processing System compiled and distributed by VAMAS–SCA Japan [385] Jo demonstrated the efficiency of his technique in obtaining the normalized energy-loss function and the initial true spectrum. It should be stressed, however, that in ref. [382] the simplest version of the Tougaard method [386] was used. In this version elastic scattering is neglected and the characteristic length L is assumed to be large compared with the inelastic mean free path. The latter assumption corresponds to setting $k(\mu) = 1$ in (5.1). The algorithm developed in ref. [382] can be seemingly applied to a deconvolution formula accounting for a specific geometry and elastic scattering. Appropriate studies in this direction would be highly desirable.

B. Elemental composition determination

The problem of elemental composition determination from AES/XPS intensities was, probably, the major factor which greatly stimulated development of the quantitative analysis. Let us consider for simplicity a homogeneous sample consisting of N different elements with unknown concentrations c_k ($k = 1, 2, \ldots, N$). It is also assumed that coherent effects are negligible and the signal electron yield for a specific Auger or photoelectron line can be described by (1.2) except for the bulk density M is replaced by the product $c_k M$ and the quantities affected by matrix effects, such as the effective escape depth and the backscattering factor (in the case of AES) become concentration dependent. Jablonski and Powell [387] showed recently that for CMA geometry, commonly used in AES, or for the magic angle geometry in XPS, elastic collisions of electrons only slightly affected the signal intensity. Based on this finding, they recommended to use the IMFP instead of λ in (1.2) when determining surface composition of a homogeneous sample. Thus, from (1.1) and (1.2) we have for the integrated peak intensity I_k associated with the kth element the

expression

$$I_k \sim Y_k = Y_k^0(M/M^0)(B_k/B_k^0)(\lambda_i^k/\lambda_i^{k0})c_k, \tag{5.2}$$

where Y_k is the yield of signal electrons leaving the target without being scattered inelastically, B_k and λ_i^k are the backscattering factor ($B_k = 1$ in the case of XPS) and the IMFP signal electrons. Superscript "0" refers to quantities for a pure element target comprising only atoms of the kth type. The instrumental factors are omitted in (5.2) for sake of brevity. From (5.2) it follows that all matrix effects are contained in the bulk density M, the backscattering factor B_k and the effective escape depth λ_k. These quantities are supposed to depend on concentrations of all elements present.

Note that influence of surface roughness has been ignored so far and the target surface is supposed to be ideally flat. Physically, it means that a typical dimension b of surface roughness features is small compared with the effective escape depth $\lambda, b \ll \lambda$. Since the escape depth $\lambda \sim \lambda_i$ and the inelastic mean free path is of order of few nm, the latter requirement is satisfied for surfaces which are almost atomically flat. This assumption is not always fulfilled. On the contrary, surface roughness may, in some cases, reduce a total signal intensity and affect the angular distribution of electrons leaving a solid [1–10].

Bearing in mind the obvious condition

$$\sum_{k=1}^{N} c_k = 1, \tag{5.3}$$

determination of all concentrations implies measuring, at least, $N - 1$ different signal peaks and subsequent solving a system of equations with respect to unknown concentrations. Below, various procedures used in practical analysis to obtain actual values of concentrations c_k are briefly considered.

(i) **Relative sensitivity factor approach.** This is the simplest method based on the assumption that matrix effects can be ignored and the measured intensity I_k is linearly proportional to the concentration c_k. Hence, instead of (5.2) one obtains

$$I_k = F_k c_k, \tag{5.4}$$

where the proportionality coefficient, F_k , is called the *sensitivity factor*. The concentration of the kth element is calculated from the formula

$$c_k = (I_k/F_k)\left[\sum_{i=1}^{N} I_i/F_i\right]^{-1}. \tag{5.5}$$

The concentration c_k determined in this way depends on the ratio F_k/F_i rather than on the absolute value of F_k , which explains the name of the method. To avoid misunderstanding, we would like to emphasize that slightly different definitions of sensitivity factors are adopted in AES and XPS. Thus, the elemental sensitivity factor in XPS represents an intensity of a peak relative to a standard, usually, C 1s. In AES they use relative Auger sensitivity factors equal to "the ratio of the Auger signal strength of a specified Auger transition from a single element to that from a selected element ..." [19]. Eventually, in both cases, division of the integrated peak intensity by an appropriate sensitivity factor provides the relative number of atoms detected.

There are tabulations of sensitivity factors [397]. Furthermore, manufacturers of XPS instruments usually recommend a set of sensitivity factors for a given type of spectrometer. As a rule, these factors are measured for elemental solids or selected compounds which, in principle, have electron scattering properties different from those of a sample studied.

The main advantage of this method is its universality, since no assumptions about a surface structure is needed to perform analysis, as soon as empirical quantities F_k are introduced. This is especially important for samples with rough surfaces or, in the form of a powder, which practically excludes the use of standards (*cf.* Section 5B(ii)). Moreover, a surface may be covered with contamination which cannot be removed by the usual methods (sputtering, heat treatment, oxygen adsorption, etc.) without uncontrolled changes in the near surface region. Examples of such samples are polymers, high T_c superconductors and so on. In those cases, the sentivity factor approach seems to be the only means of quantitative analysis.

There are, however, several objections regarding application of this technique. Since the matrix effects are neglected it is difficult to assess in advance the accuracy of quantitative analysis based on sensitivity factors. In addition, the relative sensitivity factors provided by a manufacturer correspond to a ceratin type of instruments so that their use in processing data collected by a particular spectrometer may lead to considerable errors. Attempts to calculate relative sensitivities semi-empirically [398] or from first principles [399] lead to agreement between experimental [400] and calculated values within a factor of 2 and 3 for most elements across the periodic table.

(ii) **Method of standards.** In this approach, no assumption is made about linear proportionality between the concentration and the measured peak intensity. Instead of relative sensitivities, they employ data (standards) on peak intensities from samples with known composition and properties, obtained by means of the same instrument. Method of standards allows to eliminate the influence

of instrumental factors associated with a specific set-up. Suppose, a pure element target is used as a standard, then from (5.2) we find

$$c_k = (I_k/I_k^0)(M^0/M)(B_k^0/B_k)(\lambda_i^{k0}/\lambda_i^k). \tag{5.6}$$

Thus, the concentration of the kth element in the near surface region can be calculated from relative peak intensities, I_k/I_i^0, after evaluating properly the ratios of the bulk densities, backscattering factors and the effective escape depths [401]. To obtain the total composition $N-1$ measurements and standards corresponding to the elements present in the sample are to be used. This, together the normalization condition (5.3), provides a system of N equations with respect to c_k, which can be solved by an iterative procedure.

A standard sample may not be necessarily monoatomic but a complex solid with known surface composition which is reasonably close to that of the target under investigation. Such a surface may be obtained by fracturing a given compound or alloy in vacuum, or by scrapping several top monolayers, to ensure the composition of a newly created surface to be almost identical to that of the bulk. However, applicability of such standards is limited to samples consisting of the same elements.

Finally, we would like to mention an *improved version* of the relative sensitivity factor approach. Replacing the ratio (I_k/I_k^0) in (5.6) by the relative sensitivity factor F_k, we obtain formally an expression for the concentration c_k with matrix corrections in the framework of the relative sensitivity factor formalism. One should keep in mind, however, that these corrections can be meaningful only within a certain physical model which unavoidably poses restrictions on surface conditions and thereby deprives the method of its universality.

(iii) Matrix effect corrections. Presently, it is believed that the most reliable quantitative information can be obtained by making use of standards. The method of standards, in turn, stipulates that matrix effect corrections be properly made when processing peak intensity data. The problem of matrix corrections has been considered by several researchers [402–405]. However, unfortunately, it is far from being solved. There are three types of corrections, as follows from (5.6), which involve knowledge about concentration dependence of the atomic bulk density M, the backscattering factor B and the inelastic mean free path λ_i. The term *matrix effect corrections* is used here for historical reasons. In effect, all the quantities entering the basic equation of quantitative analysis (*cf.* (1.1)) are to be evaluated from first principles to process rigorously experimental data. Such a procedure, however is not always possible.

There is no simple way to predict the value of the bulk density for a given combination of

atomic fractions since the density is, generally, a phase dependent quantity and may be a complicated function of the sample composition [406]. In routine AES/XPS analysis, two assumptions are used to assess the bulk density of a complex target. The first of them implies that the volume of an atom in an alloy or compound is the same as in a pure element target. Then the bulk density is presented in the form

$$M = \left[\sum_{j=1}^{N}(c_j/M_j)\right]^{-1}, \tag{5.7}$$

where M_j denotes the bulk density of a pure jth element target. An alternative way is to assume that the number of atoms of element j in a unit volume of a sample is equal to the product of the concentration c_j and the bulk density in a pure state. This results in the expression

$$M = \sum_{j=1}^{N} c_j M_j. \tag{5.8}$$

Formulas (5.7) and (5.8) can be used for alloys and compounds consisting of elements which, being in a pure state, form approximately the same phase as the studied sample. Thus, for instance, (5.7) and (5.8) can be hardly applied to oxides.

The backscattering factor dependence on concentration can be evaluated by formulas proposed in refs. [337,356,357,407]. Results of Zagorenko and Zaporozhchenko [408], who calculated correction factors for 1953 binary systems, indicate that the ratio (B_k/B_k^0) is almost independent of the choice of the formula for the quantity B [18]. Taking into account that a solution of a kinetic equation in the transport approximation (*cf.* Section 4C) provides the values of the backscattering factor from first principles one can state that this issue is solved at least under the assumptions discussed in Section 4C, *i.e.*, for the overvoltage exceeding the threshold energy by several ten percent.

The most important matrix correction is the inelastic mean free path λ_i. The IMFP is a macroscopic quantity and, therefore, it cannot, generally, be presented as a linear combination of concentrations in contrast to the transport mean free path (*cf.* (4.15). Nonetheless, in view of absence of any other expressions relating concentrations and the inelastic mean free path a number of authors used to evaluate the IMFP value for a target of a complex composition via the relationship [405,409]

$$\lambda_i = \left(\sum_{j=1}^{N} c_j/\lambda_i^j\right)^{-1}, \tag{5.9}$$

λ_i^j being the IMFP of signal electrons in a pure jth element. Physically, (5.9) means that the macroscopic inelastic scattering cross section is equal to the corresponding cross sections for pure

elements weighted with the relative atomic fractions. Again, it should be stressed that (5.9) is not universal and cannot be applied to elements which in pure state form a gaseous phase.

Based on the results of recent studies of the influence of elastic scattering effect we would recommend that, in the case of arbitrary XPS geometry, the quantity $\lambda_i\lambda_{tr}/\lambda_i + \lambda_{tr})$ be used as a measure of effective escape depth rather than the inelastic mean free path with an appropriate correction for the anisotropy of photoemission [146].

(iv) Multiline analysis. It is well known that statistical accuracy of experimental results may be considerably improved by increasing a number of measurements, or a number of quantities measured which are used in determination of a certain physical parameter characterizing a system. Usually, each elemental component of a sample may emit several Auger or photoelectron lines. If we select one signal electron line for one element different combinations of peaks are possible. Each combination of selected peaks, when being used in quantitative analysis, may provide somewhat different surface composition of the target. A question arises whether it is possible to develop a procedure which uses simultaneously all the peaks visible in spectra to increase the accuracy of analysis. This problem was addressed by Hanke et al. [410], who proposed the so-called *multiline approach* to process XPS data. Earlier, a similar method was applied by Jablonski et al. [411] to Auger electron line intensities.

The main idea of multiline analysis is to determine an actual concentration value by minimizing a certain function of experimentally obtained peak intensities. Suppose that atoms of the kth element emit photoelectrons from m different shells (subshells) so that an experimentalist measures m signal lines with intensities labelled I_k^j $(j = 1, 2, \ldots, m)$. Ideally, all these intensity values after substitution into (5.2) would provide the same concentration of element k. However, due to experimental uncertainties (5.2) is expected to be satisfied for each I_k^j only approximately. By introducing the respective deviations, δ_k^j, we rewrite the basic equation of quantitative analysis in the form

$$\delta_k^j = I_k^j - x_k^j, \tag{5.10}$$

where the coefficient $x_k^j = D_k^j y_k$, so that the quantity D_k^j contains the instrumental factors

$$D_k^j = \mu TDA(d\sigma_{ph}/d\Omega), \tag{5.11}$$

while y_k is concentration dependent, *i.e.*,

$$y_k = FM\lambda_i c_k. \tag{5.12}$$

It is assumed here, for simplicity, that photoelectron energies corresponding to signal lines $j = 1, 2, \ldots, m$ do not differ too much from each other and attenuation of electrons may be described by the same IMFP value.

The intensities of photoelectron lines may, however, differ noticeably in strength and, thereby, are burdened with different statistical errors. The most reliable information is expected to be derived from the most pronounced lines. To account for the accuracy of various photoelectron lines Hanke et al. [410] proposed to use the weight factors $G_k^j = I_k^j$. Minimizing the function

$$\Delta_k = \sum_{j=1}^{m} (G_k^j \delta_k^j)^2, \qquad (5.13)$$

with respect to the coefficient y_k one arrives at the expression

$$y_k = \sum_{j=1}^{m} (I_k^j)^2 D_k^j / \sum_{j=1}^{m} I_k^j (D_k^j)^2, \qquad (5.14)$$

which can be used for evaluating the concentration c_k from a set of experimental data (I_k^j, $j = 1, 2, \ldots, m$). Hanke et al. [410] applied the multiline analysis to the sputtered Ag-Au-Cu ternary alloy and were able to determine the surface composition with accuracy of about 1%.

The method can be generalized for overlayer/substrate structures as well as for essentially different photoelectron energies to increase the number of peaks used for analysis.

(v) Reliability of quantitative analysis. In 1991, reliability of different procedures of quantitative XPS was estimated by performing a round robin analysis of the same set of samples in 19 laboratories [412]. Three samples of AuCu alloy with the bulk composition of 25, 50 and 75% of gold were tested. Prior to the analysis, the sample surfaces had been cleaned by 2 keV Ar ion bombardment until contamination signals disappeared. The photoelectron spectra excited by Al Kα radiation were recorded in the vicinity of Cu $2p_{3/2}$ and Au $4f_{7/2}$ peaks. The experimental data were processed by the relative sensitivity factor approach and by the method of standards. In the latter case three standards (two elemental and alloy) were used. It was found that the alloy standard provided the most reliable information: the surface concentration of Au(Cu) was determined with uncertainty of about 1.5% depending on the alloy composition. The uncertainty of the surface composition evaluated with elemental standards was higher (1.7–2.4%) yet much lower than that obtained by the relative sensitivity factor approach (9–10%).

Accuracy of the relative sensitivity factor method improved by introducing matrix effect corrections and accounting for a spectrometer function. Ebel [409] applied this modified approach to a series of binary and ternary alloys of Cu, Ag and Au and found that the average deviations

of the surface compositions obtained from XPS data and by chemical analysis were within 2%. This result is close to the accuracy typical for the method of standards.

Extensive studies of reliability of multiline analysis were performed by Jablonski et al. [413]. The method was tested in four laboratories equipped with different spectrometers. The studied samples were AuCu alloys whose surface composition was expected to be close to that of the bulk. Such an assumption is supported by the AES data recorded by Yoshihara et al. [414] and Zhe and Tian-Sheng [415]. It was found that the average deviation between the bulk and the surface concentrations were equal to 3.2%.

The multiline approach has been recently employed in quantitative analysis of high T_c superconducting surfaces [416], polyaniline samples doped with platinum and palladium [417] and CoPd alloys [418].

C. Depth profiling

(i) Layer-by-layer analysis by sputtering. Combination of the sputtering technique (ion etching) with AES/XPS is a commonly used method for studying variation of a sample chemical composition with depth [12]. This method is destructive, since ion bombardment sputters the target material away. The underlying structure revealed, in this way, is analysed either by AES or XPS with respect to the elemental composition. Alternative cycles of sputtering and AES/XPS scans are expected to provide a depth profile [12].

There are several important features of sputter depth profiling to be mentioned. Energetic ions employed to remove upper layers penetrate the target causing displacements of host atoms from their positions and generating cascades of recoils. Some of the displaced atoms can reach a surface and escape from deeper depths than those knocked out directly from a first monolayer. During ion bombardment a considerable number of defects are created in the sample. Those defects not only migrate in the substrate but also may activate atomic diffusion processes in the sample under investigation [419]. In addition to this, the slowing down ions may produce local fields characterized by a composition-dependent chemical potential, thermal and electrostatic gradients [419,420]. All these phenomena unavoidably affect and modify the depth profile to be determined. The surface roughness and ion mixing which develop during erosion of the top monolayers may influence both the depth resolution [421–423] and the intensities of Auger and photoelectron lines [390–392]. In the case of crystalline solids, orientation of the incident beam with respect to crystallographic directions is one of the important factors to be taken into account

when interpreting experimental data.

The depth range in sputter depth profiling extends from few nm to several hundred nm with the lower limit determined eventually by the depth resolution Δz and with the upper limit put by ion-bombardment-induced effects which accumulate with time. The depth resolution Δz has been subject of intensive studies [424–430] during the last decade. If the elemental composition is analysed by means of AES/XPS then the depth resolution is ab initio limited by the attenuation length of signal electrons. This limitation is imposed by the fact that a collected electron current characterizes the average chemical composition of a top layer whose thickness is about λ_i rather than that of the interface. Thus, we conclude that the best depth resolution is about $\Delta z \sim \lambda_i$. However, in practice this resolution is rarely achieved and some additional efforts are to be applied to reach a Δz-value of the order 3–5 nm. In particular, roughening of the etched surface and broadening of the interface are noticeably reduced by applying the Zalar rotation of the sample [421,427]. An effective means to reduce ion mixing is to choose the incident ion energy and glancing angle as low as possible [431–434].

Recently Menyhard et.al. [433] have demonstrated that diminishing the energy of bombarding ions (Ar^+) from 1.0 to 0.2 keV increases noticeably the quality of a recovered depth profile. To study the influence of the ion energy the authors of ref. [433] used amorphous Ge–Si multilayer structures of 2 and 3 nm layer thicknesses and the AES. Their results corresponding to a typical measurement for the specimen 8 × [10 nm Si–15 × (2 nm Ge – 2 nm Si)] are presented in Fig. 35. Here the peak-to-peak ratio of the Auger peaks of Si (92 eV) are shown versus depth of the sample. The amplitude of Si oscillations is seen to decrease with increasing ion energy. On the other hand, this amplitude was found to remain unchanged with prolonged sputtering at a constant ion energy [435–437]. On these grounds, the ion bombardment induced damage was suggested to be predominantly ion mixing [433].

Systematic studies of depth profiling by sputtering technique are carried out primarily on model multilayer systems whose preparation implies thin film thickness measurements [420,426,438–441]. A thickness of a several ten nanometer layer can usually be measured with a certain tolerance, typically of about 5% [420]. This introduces an additional uncertainty into the obtained depth profile and thereby affects the depth resolution of a method employing standards. Whereas in the past model systems were, as a rule, metallic multilayers or single oxide overlayer on metal substrates, recently Zalar et al. [420] reported on the preparation and development of new structures consisting of metal/oxide, oxide/oxide and metal/semiconductor multilayers. Figure 36 displays the depth profile of an electrically conductive Ni/Cr/Si multilayer system, obtained by

rotational AES depth profiling, using 3 keV Ar ion beam at an angle of incidence 45°. The depth resolution Δz drastically increases at the interfaces metal/semiconductor (Ni/Si and Cr/Si). For comparison, the depth resolution obtained for $Ni/Cr/NiO/Cr_2O_3$ and NiO/Cr_2O_3 model samples

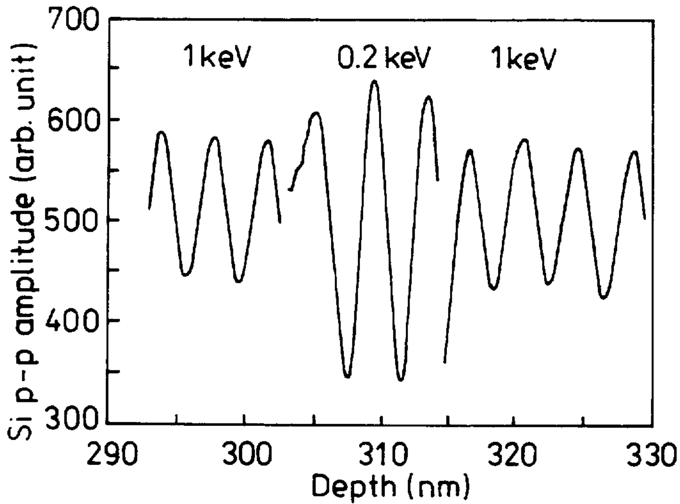

Fig. 35. The Si peak-to-peak amplitude as a function of depth for the specimen: 8·[10 nm Si – 15·(2) Ge – 2 nm Si] (part of the measured depth profile). The angle of incidence of Ar ions is 83° (after ref. [433]).

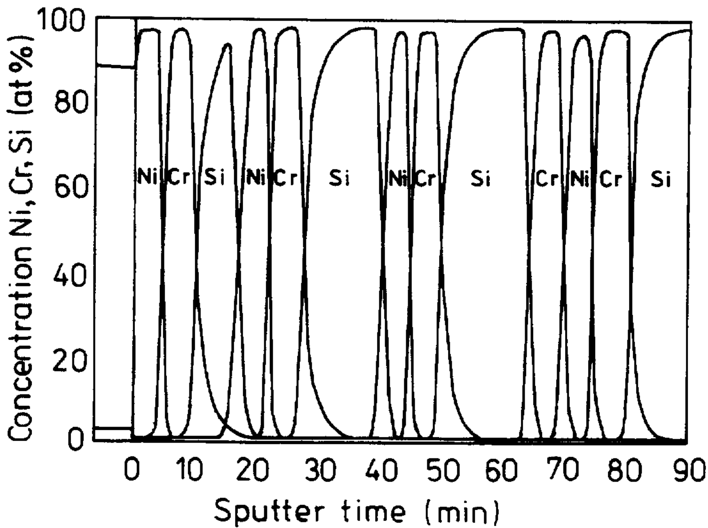

Fig. 36. The depth profile of the Ni/Cr/Si multilayer obtained by AES and sputtering by 3 keV Ar ions incident at the angle 45° (after ref. [420]).

at grazing incidence angles is also shown in Fig. 37. It is seen that the depth resolution for metal/metal interfaces is about 5.5 nm and by a factor of 2 less than that for metal/silicon interface. Among possible explanations of this phenomenon the authors of ref. [420] mention different natural widths of the interfaces originating from the deposition process, secondary topography and formation of silicides during ion bombardment.

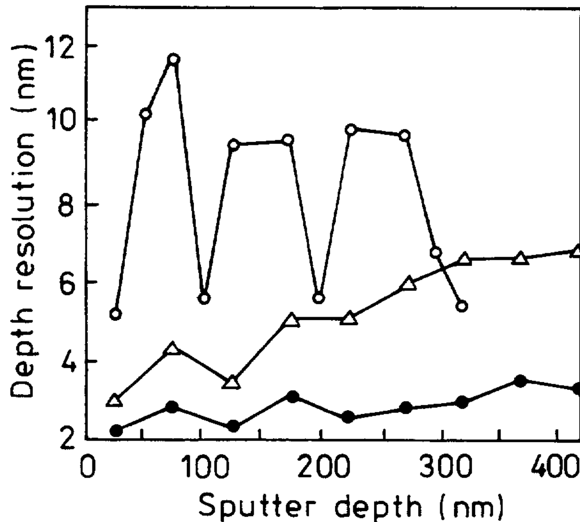

Fig. 37. The depth resolution as a function of sputter depth for three model multilayer structures (Ar ion energy E and angle of incidence θ are indicated in parentheses): filled circles - NiO/Chromium oxide, (1 keV, 81°); open triangles - Ni/Cr/NiO/Chromium oxide, (1 keV, 61°); open circles - Ni/Cr/Si (3 keV, 45°) (after ref. [420])

One of the prospective reference materials for depth profiling is AlAs/GaAs superlattice [434]. This superlattice is characterized by atomically flat and abrupt interfaces. Kajiwara and Shimizu [434] reported on a round-robin test of depth profiling an AlAs/GaAs sample by means of AES, XPS and SIMS techniques.The recovered depth profiles are shown in Fig. 38. The depth resolution obtained by AES and SIMS is almost independent of depth. In contrast to this, in most XPS depth profiles, the depth resolution deteriorates with sputter time, except for experiments employing a sample rotation. As pointed out by the authors of ref. [434] the reason may be the relatively large ratio of the XPS probe diameter to the ion raster scanned width (0.15). The corresponding quantity in the case of AES is rather small (0.003) since the probe diameter of AES ($\sim 3\mu$m) is almost two orders of magnitude less that that of XPS (300 μm). Therefore, crater edges may lead to worsening an XPS resolution considerably [434]. The depth resolution in AES was found

to become better when using grazing ion incidence angles and to be slightly correlated with the ion kinetic energy.

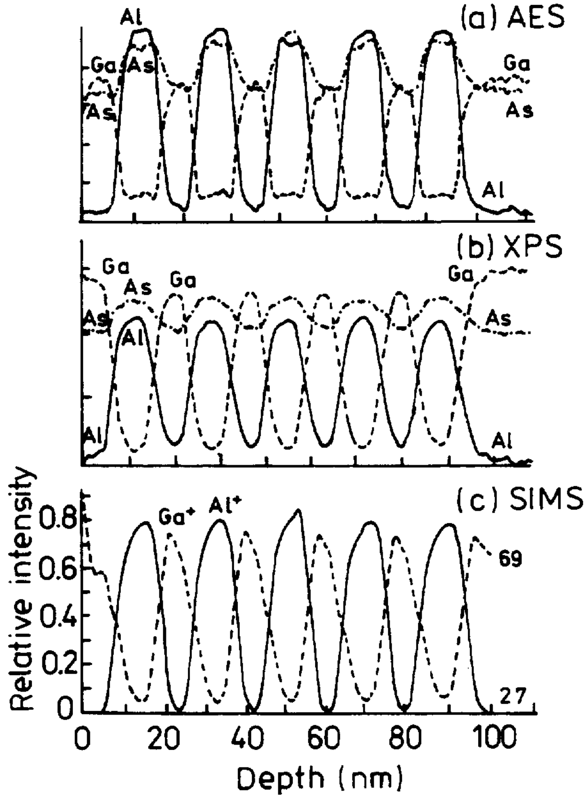

Fig. 38. Depth profiles of an AlAs/GaAs superlattice obtained with the highest depth resolution by (a) AES, (b) XPS and (c) SIMS (after ref. [434]).

(ii) Nondestructive depth profile reconstruction. The idea of making use AES/XPS data for nondestructive depth profiling has been attracting attention from researchers for a long time [442–468]. Rapid energy attenuation of signal Auger and photoelectrons presumes a posibility of studying composition variation with depth in layers of thicknesses of a few nm. The sputtering technique that produces good results for depths ranging from 5 to 500 nm in the case top monolayers turns out to be ineffective for very shallow structures due to damages introduced by ion bombardment. Until now in the majority of papers devoted to nondestructive reconstraction of a composition depth profile, the angle-resolved modes of AES/XPS (ARAES and ARXPS) have been employed [469]. In angle-resolved experiments, signal electrons of a specific energy are collected at different emission angles. The angular dependence of a recorded intensity is then

analyzed to extract quantitative information about the unknown depth profile. In this approach, a part of the energy spectrum accompanying the characteristic peak is not used and therein contained information eventually is lost for analysis. Meanwhile, as was first pointed out by Tougaard [277] the inelastic background depends on the depth profile and thereby represents an additional means for investigation of the sample composition [277,381]. Below we start with the general formulation of the reconstruction problem and then consider methods of obtaining solution profiles from experimental data, by presenting some examples.

In the case of an inhomogeneous sample with an arbitrary depth profile, the differential photoelectron yield is given by the expression

$$Y(\Omega, E) = \int_0^\infty dz\, c(z) \int_0^\infty dE_0 \int_{4\pi} d\Omega_0\, S(E_0, \Omega_0)\Phi(z, \Omega, E \mid \Omega_0, E_0), \tag{5.15}$$

$c(z)$ being the concentration depth profile, $S(\Omega, E)$ is the initial angular and energy distribution of signal photoelectrons released in a unit volume of the sample per unit time and $\Phi(z, \Omega, E \mid \Omega_0, E_0)$ is a usual depth distribution function describing the probability for an electron generated at the depth z with the energy E_0 and moving initially in the direction Ω_0 to escape from the target in the direction Ω with the kinetic energy E. In the adopted normalization of the DDF, the differential yield Y is proportional to a certain number of electrons escaping from a unit area of the surface. Introducing the probability $P(z, \Omega, E)$ for an electron created at the depth z to escape from a solid with a specific energy and momentum, one can rewrite (5.15) in the form of a single integral, namely,

$$Y(\Omega, E) = \int_0^\infty dz\, c(z) P(z, \Omega, E), \tag{5.16}$$

where the function $P(z, \Omega, E)$ is equal to a double convolution with respect to the initial energy and direction of motion. Since values of the quantity Y are readily available from experimental measurements the basic question to be addressed is how it is possible to deconvolute expression (5.16) in order to find the depth profile $c(z)$. To answer this question it is necessary to specify the properties of the escape probability $P(z, \Omega, E)$. The choice of the function P eventually depends on a model used to describe electron-solid interaction.

From the previous section, we have seen that the escape probability is affected by both elastic and inelastic scattering of electrons on their way out of the target. Beside that the anisotropy of photoemission may influence noticeably the electron escape process. Although it was realized long ago that all these effects were to be taken into account when solving numerically equation of type (5.16), a rather simplistic version of the function $P(z, \Omega, E)$ has been used in practical depth profiling until recently [469]. In particular, elastic scattering was completely ignored and

the anisotropy of photoemission was believed to be of no importance. The escape probability of electrons contributed to the characteristic peak was assumed to obey an exponential law with the decay rate determined by the product of the inelastic mean free path and the cosine of the emission polar angle. Under this condition no azimuthal angle dependence of the recorded signal was expected. Without losing generality, we write, within this model, $P(z, \Omega, E) \sim S\exp(-z/\lambda\cos\alpha)$, where S is the total number of characteristic electrons emitted in all directions in a unit volume per unit time. Then (5.16) effectively reduces to a Laplace transform equation type [446]:

$$Y(p) = (S/4\pi)\int_0^\infty dz\, c(z)\exp(-pz), \qquad p = 1/\lambda_i\cos\alpha. \tag{5.17}$$

If the function $Y(p)$ were known analytically in a continuous interval of p-values, finding the depth profile would not represent any difficulty [470]. However, in an experimental situation, the best one can hope for is a finite set of values of the function $Y(p)$ measured for some take-off angles. Topologically, such a set of values in the complex p-plane contains too little information to obtain a unique solution to (5.17). In addition, one may expect the Y-values found in this way to deviate from the true ones due to uncertainties intrinsic to any experiment. For example, the integrand in (5.17) depends on a specific value of α, while experimentally measured intensity is unavoidably averaged over a small, yet finite, half-cone acceptance angle. Therefore, the quantity Y is actually a certain mean value in the vicinity of α. As a result, a broad class of numerical solutions formally satisfies (5.17) [471–473] and a researcher faces a difficult, and at first sight hopeless, problem of choosing an appropriate depth profile.

One of the ways to overcome these difficulties is to increase a number of different take-off angles N and a signal-to-noise ratio q. However, for $N > 10$ the precision of peak intensity measurements is expected to be limited by systematic errors rather than counting statistics [469]. In addition, the maximum achievable signal-to-noise ratio in commercially available AES/XPS set ups does not exceed, as a rule, $2 \cdot 10^2$ [469]. In this connection, the question arises how large the relative error $\delta_c = \Delta c/c$ in determination of the concentration value may be and what the depth resolution Δz of the method is. Intuitively it is clear that both of these quantities are interrelated: the larger the relative depth resolution $\delta_z = \Delta z/z$ is the more precisely the concentration depth profile can be measured and vice versa [474]. Studying this problem on the basis of eigenvalues of the Laplace transform operator Cumpson [469] has come to conclusion that for $\delta_c = 0.5$ (this seems to be the highest signal-to-noise ratio of the recovered depth profile, which is still acceptable from a practical point of view) the relative depth resolution is about unity, $\delta_z \sim 1$, as the quantity q ranges from 20 to 200. In the limiting case of high signal-to-noise

ratio, $q \gg 1$, his result (formula (14) of ref. [469]) may be simplified to the compact expression

$$\delta_z = \pi^2[\ln(2\pi q^2)]^{-1}, \; q \gg 1 \tag{5.18}$$

from which it follows that the depth resolution increases very slowly with augmenting the signal-to-noise ratio q. Thus, even for $q = 10^4$ the quantity $\delta_z \sim 0.5$. It is interesting that estimate (5.18) is in good quantitative agreement with results of Yih and Ratner [448] (*cf.* Fig. 39), obtained for three emission angles.

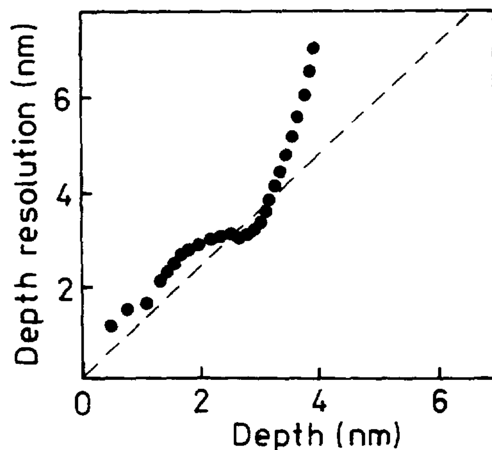

Fig. 39. Comparison of the angle-resolved XPS limit on the depth resolution predicted by Eq. (14) of ref. [469] (dashed line) with the results found by Yih and Ratner's "method B" [448] (filled circles). The data for three emission angles are used (the largest number for which the "method B" is still stable) (after ref. [469]).

The gloomy prediction of (5.18) does not mean that a successful restoration of the composition depth profile is not possible. On the contrary, a number of recent papers report on quite satisfactory solutions of the inverse problem. This is achieved, however, at the expense of making use of *a priori* assumptions about the shape of the depth profile. At present there are two major methods employed in literature: *discretization* and *regularization* [469]. In the discretization scheme the profile is approximated either by piecewise linear curve or by a finite number of step depletions/accretions [445,446,448]. A further strategy is to minimize the difference between the experimental data set and the calculated yields for different emission angles α_j ($j = 1, 2, \ldots$). Usually, a suitable solution is possible if the transform is performed in the forward direction rather than in the reverse one [446,460]. Bussing and Holloway [446] demonstrated that layer-wise solution was capable of matching a simulated intensity to an agreement greater than 99.5%

in a relatively short running time, recovering nonmonotonic profiles without presupposition of such a behaviour. Tyler, Castner and Ratner [450], who performed a relative comparison of the discretization and regularization methods, found that the discretization scheme became unstable with increasing the number of data points. A more general regularization approach involves the method of Tikhonov [471,472] or the *Maximum Entropy technique* [475,476]. In both cases, a solution is obtained by minimizing the quantity

$$C = \chi^2 + \alpha^* U, \tag{5.19}$$

where χ is a statistical misfit between the measured experimental and calculated theoretical data, being equal to the sum of the squared residuals weighted by their variances [469]

$$\chi^2 = \sum_k (Y_k^{exp} - Y_k^{th})^2/\sigma_k. \tag{5.20}$$

In (5.19), α^* is the regularization parameter and U represents the measure of unsmoothness. The values of the parameter α^* can be determined either empirically for certain classes of the depth profile [468] or obtained from a *Bayesian statistical analysis* of the data [477]. From the Bayesian analysis it follows, in particular, that the data themselves determine a certain probability distribution of α-values. Moreover, these distributions are characterized by a sharply peaked maxima. The most probable value of the parameter α can be then used to solve (5.20) [459]. The existence of an optimum α-value is prompted by the fact that, generally, larger values of the regularization parameter tend to stabilize a solution, while smaller ones are necessary not to smooth out real features of the depth profile [9,467].

In the method of Tikhonov, the usual choice is $U = \int [c(z)]^2 dz$, while within the Maximum Entropy approach the quantity U is proportional to the entropy, so that the unsmoothness might be $U = \int c(z) \ln[c(z)] dz$. In the latter case, minimizing (5.19) is sometimes interpreted as reasonably fitting the measured data and using the minimum information to do so, or, in other words, the maximum information which yields artifact-free reconstructions [466]. Another point of view is that Maximum Entropy is "...neither more nor less than one usefully nonlinear version of the general regularization scheme..." [240,469]. To illustrate applications of the regularization method we present few examples published recently.

Tyler et al. [450] restored successfully the depth profile of a polyurethane film deposited on a gold substrate. The obtained depth profile is shown in Fig. 40 and indicates that the film thickness is about 60 Å. The composition of the sample varies little in the near surface region, at depths less than 10 Å. In particular, the authors of ref. [9] found that for z = 10 Å the film

composition was: 76.5% C, 14.5% O and 9.0% N. These data are in agreement with the expected relative concentrations of carbon, (75%), oxygen (16.5%) and nitrogen (8.5%), resulting from the stochiometry of polyurethane.

In Fig. 41, the depth profiles of oxygen, carbon and iridium atoms in CO/Ir(111) system recovered by Cherkashinin [467] are shown as functions of depth in units of IMFP. He used the *Tikhonov regularization method* and experimental data for intensity ratios I_{C1s}/I_{Ir4f} and I_{O1s}/I_{Ir4f} measured in ref. [40] at 8 different emission angles ranging from 20 to 82.5 degrees. Note that in the scheme of Cherkashinin the variation of the IMFP with depth is accounted for by the semiempirical formula of Sekine et al. [407] and simple exponentially decaying escape probability is used. The IMFPs for pure carbon and iridium were taken from ref. [171], while that for oxygen was calculated by the empirical formula of Seah and Dench [206]. Obviously, the inelastic scattering description in the model of Cherkashinin leaves much to be criticized.

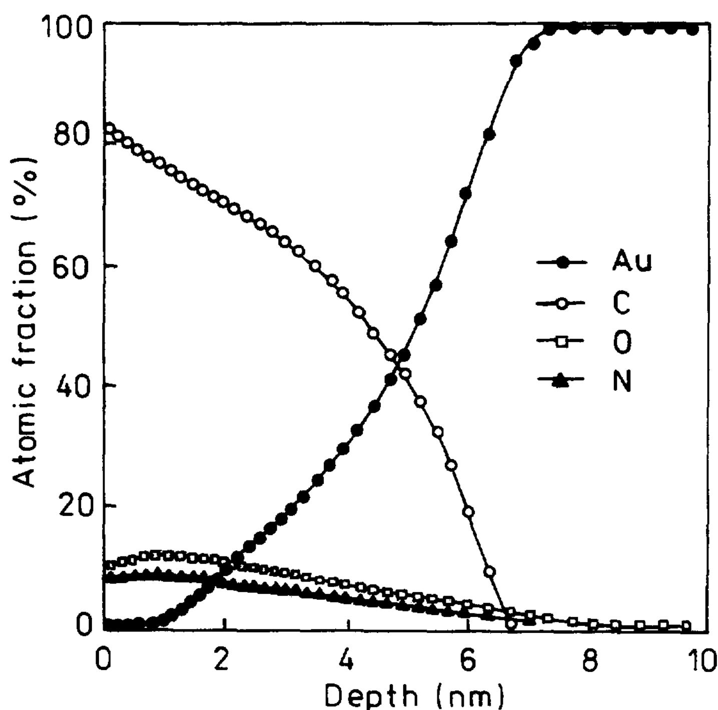

Fig. 40. The depth profile of a polyurethane foil on a gold substrate recovered by the regularization method: filled circles – Au, open circles – C, open squares – O, open triangles – N [450].

For example, a system consisting of a substrate and a monolayer of adsorbed molecules is to be characterized by a macroscopic inelastic cross section calculated on the basis of a specific near surface electronic structure rather than by making use of IMFPs for pure elements. However, due to weak variation of the IMFP with concentration and atomic serial numbers the numerical values of λ_i used in ref. [467] represent a reasonable assessment. From Fig. 41 and values of IMFPs, it follows that oxygen atoms are located at the surface while carbon atoms form a layer in between

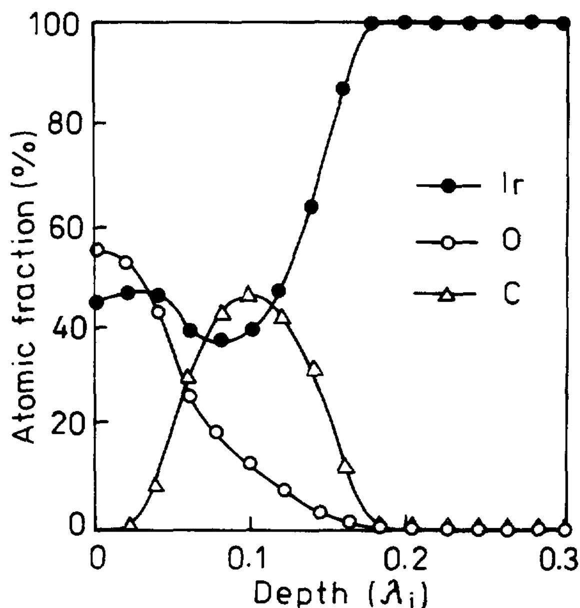

Fig. 41. The depth profile recovered by the regularization method for CO/Ir(111) system: filled circles - Ir, open circles - O, open triangles - C [26].

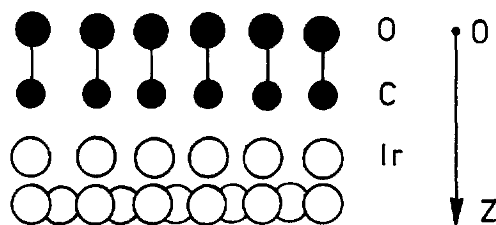

Fig. 42. Schematic representation of CO molecules adsorbed on a surface of Yr substrate.

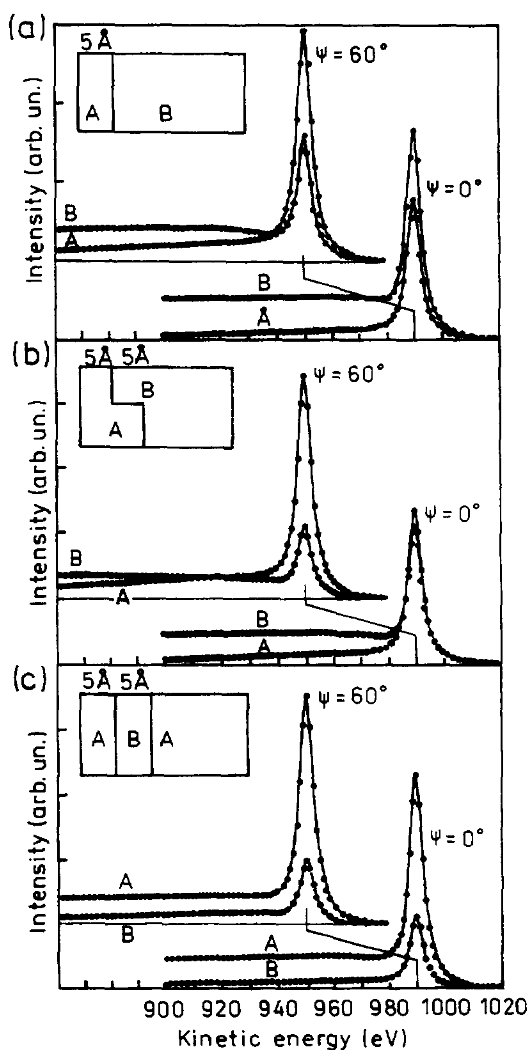

Fig. 43. Energy spectra for the three model multilayer systems at different polar emission angles, calculated analytically within the transport approximation (after ref. [466]).

the substrate (Ir) and the the first monolayer dominated by oxygen. This is in satisfactory agreement with the model of carbon-oxide absorption (*cf.* Fig. 42). The saturation coefficient of CO molecules (0.50 - 0.55) and the thickness of the CO layer (2.67 Å) were found to agree well with data published previously [479] and the sum of the covalent radii of O and C.

The first attempt to use a more realistic model for the function $P(z, \Omega, E)$ and the energy-resolved AES/XPS in nodestructive depth profiling was made in ref. [466]. Instead of assuming

an exponentially decaying escape probability the quantity P was calculated analytically from solution of the kinetic equation and a part of a model energy spectrum in the near-peak region with about 90 data points was used in the Maximum Entropy reconstruction procedure. In the first series of calculations, the energy spectrum was evaluated analytically for two element samples and three model depth profiles shown in Fig. 43. The scattering properties of the samples were assumed to be independent of depth and correspond to 1 keV electrons in a gold target.

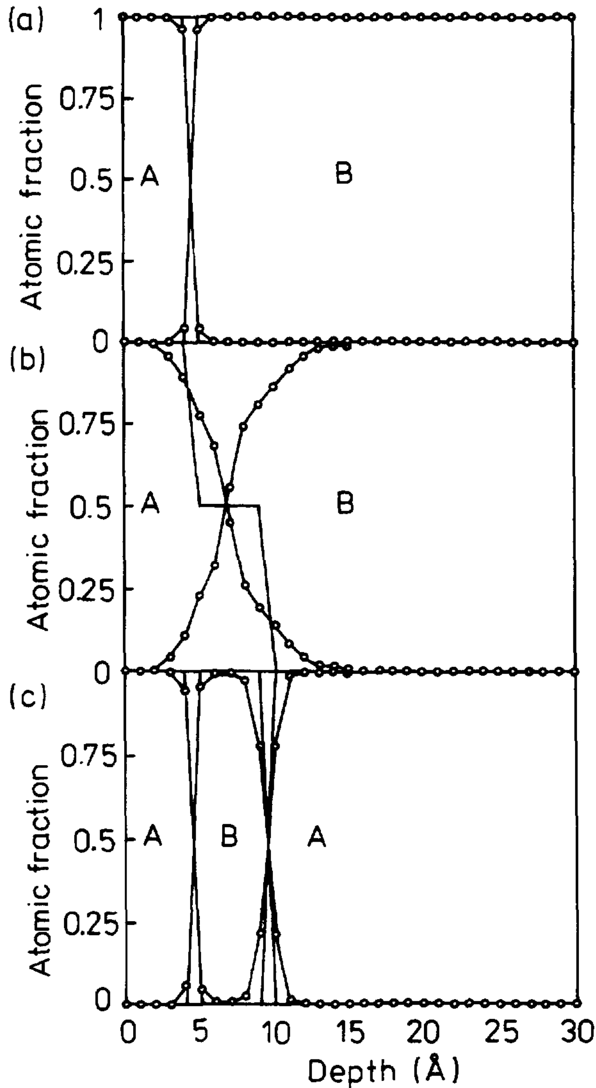

Fig. 44. Depth profiles reconstructed by the Maximum Entropy regularization procedure based on the data shown in Fig. 43 (after ref. [466]).

The elastic scattering was accounted for in the transport approximation. The transport mean free path was calculated from Tilinin's formula [479], while the total IMFP and the differential inverse IMPF were evaluated by expressions of Tanuma and coworkers [171] and of Tougaard [277], respectively. To obtain a unique solution to (5.16) without resorting to sensitivity factor values energy spectra were calculated for two emission angles. Note that in this procedure the depth profile and the intrinsic energy spectrum were recovered simultaneously. Making use of the prior knowledge about the substrate composition allows to perform satisfactory reconstruction for all considered cases. The results are shown in Fig. 44. The worst case represents the sample with an intermediate layer of 50% of element A and 50% of element B. However even in this situation the recovered profile provides all essential features.

In the second run of calculations, the spectra were simulated by the MC code employing a realistic differential elastic scattering cross section evaluated by the partial wave expansion method and the differential inverse IMFP derived from linear response theory. The MC results containing ab initio a certain amount of noise due to their statistical nature were used as data of "a numerical experiment" and then were processed by the Maximum Entropy technique with the escape probability derived analytically. The recovered depth profiles showed the interfaces between overlayers and substrates smoother as compared to those obtained by processing the analytically simulated response. The reason for this may be a certain amount of noise contained in MC data. Nonetheless, the major characteristics of sample compositions are quite well reproduced [466].

It is worth noting that Seelmann–Eggelbert and Keller [480] tried to account for elastic scattering effect by a simple rescaling of the attenuation length and the depth profile, assuming the validity of the modified Beer–Lambert law. These authors admitted, however, that no rigid proof of such a statement exists. Meanwhile, it can be shown directly by solving the boundary value problem that escape probability as a function of depth of origin is much more complicated and may be even nonmonotonic for s- photoelectrons [207]. Therefore, in general, no rescaling of this type to describe the influence cf elastic collisions is possible.

In conclusion, we emphasize that regularization methods allow usually to reconstruct composition depth profiles of an arbitrary shape for the signal-to-noise ratio larger than 5–10 [469]. They do not impose any restrictions on the number of components in a sample and may be especially effective when employing not only the angular but also the energy dependence of the Auger or photoelectron line intensity.

D. Synchrotron radiation in XPS analysis.

Rapid development of synchrotron radiation facilities opens new areas for XPS applications. For instance, during 1993, three sources of soft x-rays (ALS - Berkeley, ELETTRA - Trieste and SRRC - Taiwan) have been put in operation [481]. There are a number of properties of synchrotron radiation which makes it more and more attractive in surface analysis. Those include: (1) high spectral brilliance, *i.e.*, amount of photons per unit solid angle and source area; (2) continuous energy spectrum; (3) high degrees of polarization of photons in the electron orbit plane; (4) possibilities for a photon beam to be collimated in the vertical direction or focused into a small spot [482]. As a result, synchrotron-radiation based XPS, in addition to traditional advantages such as multi-elemental detection capability and non-destructiveness, is characterized by much shorter analysis times and better spatial resolution. In this section, we consider two relatively new XPS techniques involving synchrotron radiation: x-ray photoemission spectromicroscopy and x-ray- standing-wave induced photoemission.

(i) **X-ray photoemission spectromicroscopy** has become possible due to a huge gain in brightness of the third generation of light sources (with respect to the second generation sources the brightness increased by four orders of magnitude [483]). Ade et al. [484] reported on the development of the scanning photoelectron microscope (X1-SPEM) at beam line X1A at the National Synchrotron Light Source (Brookhaven National Laboratory). The imaging characteristic of X1-SPEM is determined by the size and profile of the zone-plate-produced microprobe. The probe beam scans a sample mechanically. Simultaneously, a sample current and an intensity into a selected electron kinetic energy window are recorded. In addition the energy window of the cylindrical mirror analyser is canned to acquire a photoelectron energy spectrum [484,485]. Elimination of astigmatism introduced by the beam line transport optics allowed to achieve a lateral resolution approaching 0.1 mm. In usual XPS techniques, a recorded intensity represents a signal averaged over sample areas of the order of 1 mm^2. Hence, the lateral resolution of X1-SPEM is almost by four orders of magnitude higher than that of traditional XPS. By means of X1-SPEM, they acquire typically two images: a total electron yield recorded via the sample current and an image with the CMA tuned to a particular kinetic energy of signal electrons (these are Auger electrons or photoelectrons excited by incident photons) [484]. The energy resolution of this microscope is better than 1 eV.

The upgraded version of the scanning photoemission microscope MAXIMUM (multiple-application x-ray imaging undulator microscope) possesses the same lateral resolution (0.1 μm) as

X1-SPEM and a little bit better energy resolution which is about 0.4 eV [486]. In MAXIMUM, radiation emitted by the Stanford-Berkeley undulator is filtered with a monochromator and then focused onto a sample. A number of different spectroscopic techniques may be performed on a small area: absorption, reflection and desorption. A target can be scanned when measuring a photoemission signal at a fixed photon energy, corresponding to photoelectrons emitted from a specific core level [486]. Maximum was successfully employed in the materials and life sciences. In particular it was used to detect elements in a neuron cell membrane [486].

The major limitation in further improvement of lateral resolution of existing scanning photoemeission microscopes is brightness of syncrotron radiation sources. It is expected that the brightness will be increased additionally by 2–3 orders of magnitude. Thus the prospective lateral resolution will be about 0.1–1.0 nm which is the ultimate (diffraction) limit of this quantity.

(ii) X-ray standing wave induced photoemission. Although the birth of the x-ray standing wave (XSW) technique dates back to 1964 [487,488] the method has emerged only recently as a powerful tool for determination of chemical composition and structure of surfaces. Two major developments contributed to this: application of synchrotron radiation which made measuring times reasonably short and ultra-high-vacuum set-ups allowing to perform studies with XSW in-situ [488]. The basic idea of the method is to shift the standing wave field with respect to reflecting planes of the near surface region by scanning in angle or energy through the interval where reflectivity reaches its maximum associated with the Bragg condition. This field induces photoionization which manifests itself through Auger electron and photoelectron emission as well as fluorescence yield. Recording the photoionization rate as a function of the standing wave position makes possible to identify atoms relative to the diffracting plane [489]. Diffracting planes can be not only atomic monolayers but also layered synthetic microstructures with periods ranging from 2 to 20 nm [490]. The latter represent depth-periodic systems consisting of alternating layers of low and high electron density materials (for instance, Si/W or C/Pt) [490,491]. It should be emphasized that in crystalline targets the period of a standing wave is about the interatomic distance whereas in layered microstructures this quantity is determined by the period of a system of layers.

The standing wave generated in a sample extends well above its surface. Therefore, the technique can be used to locate adsorbates on crystalline surfaces. Correspondingly, a thin overlayer deposited on a layered synthetic microstructure can be studied by a standing wave with a period

exceeding greatly interatomic spacing.

An x-ray standing wave can be generated by interference of two coherent travelling waves. In practice, they employ either diffraction from a periodic structure, or a total reflection phenomenon. The intensity in the standing wave is described by the expression [488]

$$I = 1 + R + 2\sqrt{R}\cos(v - \mathbf{q}\cdot\mathbf{r}), \tag{5.21}$$

where R is the reflectivity (or the ratio of the amplitudes squared of the incident and reflected waves), v is the phase shift between the two waves and $\mathbf{q} = \mathbf{k}_0 - \mathbf{k}_r$ represents the difference of the wave vectors of the incident and reflected waves. The reflectivity R is a function of the complex, lattice periodic susceptibility χ, the reflection and the Bragg angles, Θ and Θ_B. The most important feature of the reflectivity is that R differs essentially from zero only in narrow intervals of the reflection angle and incident photon energy variation in the vicinity of the Bragg condition. Typically, the FWHM of a symmetrical Bragg reflection is about [492–494]

$$w \sim r_0\lambda^2/d^3. \tag{5.22}$$

where $r_0 = e^2/mc^2$ is the classical electron radius, λ is the x-ray wave length and d is the interatomic spacing. From (5.22), it follows that for x-rays in the keV energy range the reflectivity is about unity in a narrow cone with the half-cone angle $\Delta\Theta = \mid \Theta - \Theta_B \mid$ being about several ten μrad. The respective energy variation is of the order of a fraction of eV.

As is seen from (5.21), the intensity is spatially modulated. As a result, there are minima and maxima of intensity or nodes and antinodes lying on the planes so that the vector $\mathbf{q}$ is normal to the wavefield planes [488]. Since the photoelectron absorption probability is directly proportional to the intensity I, the photoelectron yield Y is also modulated. However, to find the quantity Y one should sum over all yields of particular atoms and average the result obtained over thermal displacements of nuclei from their equilibrium positions. After doing this, one arrives at the expression [488]

$$Y/Y_0 = 1 + R + 2\sqrt{R}f\cos(v - 2\pi P), \tag{5.23}$$

Where Y_0 is the emission yield away from the Bragg reflection, f is the so-called *coherent fraction* and P is the *coherent position.* The origin of these terms can be easily understood from comparison of (5.21) and (5.22). Physically, the coherent position is a measure of the atom layer average position modulo the interatomic spacing (or, the period of a layered microstructure), while the coherent fraction represents a measure of the width of the atom layer [490].

Recently, Shi et al. [495] and Heskett et al.[496] performed investigations of absorption sites of Rb atoms on the Cu(111) surface and Rb coverage dependence of structure and degree of ordering of Rb/Cu(111) system XSW technique. A beam of x-rays was incident normal to the surface in the (111) refeclection case and at the angle 70.53° with respect to the normal for $(11\bar{1})$ reflection. The amplitude variation and the phase shift of the standing wave were monitored by Cu LMM Auger electron yield and Rb $2p_{3/2}$ photoemission peak at 920 eV and at 1170 eV kinetic energies,

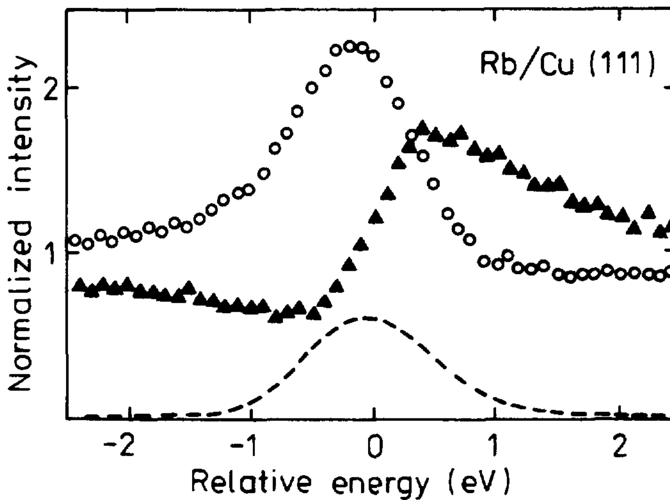

Fig. 45. Photon energy dependence of the reflectivity (open circles), Rb 2p photoelectron line intensity (filled circles) and Cu LMM Auger electron yield (filled triangles) for the (111) reflection plane of the Rb/Cu(111) target [496].

respectively. Typical energy distributions in the near Bragg reflection region are presented in Fig. 45. The maximum of reflectivity (open circles) is placed exactly at the zero relative energy which corresponds to the 2.9745 kev peak of the reflectivity rocking curve. Meanwhile, the photoelectron yield (filled circles) reaches its maximum at the relative energy of −0.2 eV. The Auger electron yield (filled triangles), on the contrary, has a maximum at +0.5 eV relative to the zero point. These results can be understood qualitatively by noting that a measurement of Cu LMM Auger electrons with the IMFP of about 1 nm is expected to provide information about copper bulk lattice positions (the interatomic spacing in the case considered is $d = 0.21$ nm). The high energy side of the Bragg peak in Fig. 45 corresponds to the standing wave field maximum intensity being on the diffracting planes. Comparison with calculations of the Cu LMM intensity profile shows that the coherent fraction and coherent position of the copper atoms are 0.93 and

0.02, respectively. That is consistent with the well ordered Cu(111) system. Note, that a zero coherent fraction ($f = 0$) would correspond to atoms randomly distributed with respect to the diffraction plane. The Auger electron (or the photoelectron) yield, in this case, would repeat the energy dependence of the reflectivity since the last term in (5.23) vanishes. If the photon energy is set on the low energy side of the Bragg peak the maxima of the standing wave intensity are shifted towards the positions in midway between the diffracting planes. The copper atoms are, thus, in *a shadow* and the Auger electron signal from Cu atoms is decreased. The maximum in the Rb $2p_{3/2}$ photoelectron intensity in the low energy side indicates that Rb atoms are (1) well ordered in the [111] direction and (2) shifted away from the plane (111). Estimates show that Rb atoms are indeed positioned at 0.08 nm above the Cu(111) lattice plane (the coherent position is 0.39) yet are rather well ordered in the direction perpendicular to the plane (111) (the coherent fraction is 0.71) [496].

A low coherent fraction of Rb atoms obtained in the (111) geometry [16] may be interpreted as a loss of ordering in the direction parallel to the Cu(111) plane. Such a loss of ordering was also observed by other researchers for several alkali/metal structures, who employed SEXAFS [497] and LEED [498] methods. On the other hand, Fasel et al. [499] analysing x-ray photoelectron diffraction patterns from the room temperature Na/Al(111) samples came to conclusion that apart from the $(\sqrt{3}\times\sqrt{3})R30°$–Na/Al(111) structure with the Na atoms adsorbed well above the Al(111) plane there exists also a strongly intermixed system - p(2×2)–Na/Al(111). In the latter case, the Na coverage is 0.5 ML so that a unit cell contains two Na atoms. Every fourth surface Al atom is replaced by a Na atom. Such a substitution results in a p(2×2) superstructure. The remaining Na and Al atoms are to be placed in the fcc and hcp adsorption sites of the fcc(111) surface, respectively, to fit the experimentally observed focusing peak intensities at polar angles 68.5° and 79.5° [449].

E. Auger photoelectron coincidence spectroscopy

Both Auger and photoelectron energy distributions in the vicinity of characteristic peaks exhibit a complicated structure owing to contributions of shake-up/shake-off effects and extrinsic plasmon energy losses. Especially difficult to analyze are the spectra with well overlapped lines such as, for instance, Auger peaks of transitional elements (Fe, Hi, Co, Cu and others). Changes in the chemical composition and structure of a sample can further alter the shape of recorded spectra [500–502]. One of the effective means to simplify signal electron spectra is to apply a

coincidence technique which provides additional information about a scattering event. Generally, coincidence spectroscopy implies detection of two or more particles which have been emitted within a sufficiently short period of time, so that these particles are expected to arise from the same event [503]. Auger photoelectron coincidence spectroscopy (APECS) [504–506] represents a successful example of the coincidence method as applied to surface analysis. The basic idea of APECS is to measure x-ray excited Auger electron spectrum in coincidence with the ejected photoelectron. The method was developed more than a decade ago by Haak et al. [504,505]. In this technique, two energy analyzers are focused on a sample irradiated by x-rays so that one detector is set on a maximum of a photoelectron peak, while the other scans the respective Auger electron spectrum. By applying the coincidence method to NiCu alloy Haak et al. [507] effectively separated the Cu component in the Auger peak of the sample.

There are two opportunities to excite Auger electrons by x-rays. The usual way is to use the standard x-ray sources in commercially available XPS set ups as it was done originally by Haak et al. [504,505] and later by Thurgate et al. [502,507–510]. The other option is to employ synchrotron radiation which permits easy variation of photon energy and offers a clear advantage in terms of intensity [503,511–515]. However, in the latter case, the photon energy is, as a rule, less or about several hundred eV. Due to a small probability for the Auger and photoelectrons originating from the same core-shell excitation to enter detector windows simultaneously, acquiring statistically significant results needs considerable collection times (several weeks for standard x-ray sources and several days, in the case, of synchrotron radiation [503,513]). As a result, special requirements are put on the experimental equipment in terms of long stability [503]. This is probably the major disadvantage of APECS and the reason why this technique has not been so widely used up till now. On the other hand, APECS offers a unique opportunity to investigate different processes affecting an Auger electron line shape since only those parts of the Auger electron spectrum are displayed, which result from a particular ionization event [510].

To distinguish the distributions obtained in coincidence experiments from those found by summing all points in the time-to-amplitude spectra, irrespective to the time interval between the counts of Auger and photoelectron channels, they use terms coincidence and singles spectra, correspondingly [503,516]. When an Auger electron is collected in coincidence with a photoelectron the intensity of a coincidence spectrum is determined by a product of respective escape probabilities of signal electrons. This results in reducing the effective escape depth of the Auger electron whose effective mean free path becomes equal to [502]

$$\lambda_{eff} = \lambda_i^A \lambda_i^{ph} / (\lambda_i^A + \lambda_i^{ph}), \tag{5.24}$$

where λ_i^A and λ_i^{ph} are the inelastic mean free paths of the Auger and photoelectrons, correspondingly. If the energies of the signal electrons do not differ too much from each other then their mean free paths are of the same order of magnitude, $\lambda_i^A \sim \lambda_i^{ph}$. Since the surface sensitivity is inverse proportional to the IMFP, the surface sensitivity of APECS is typically a factor of 2 higher than that of conventional AES. In this respect the situation is similar to that in Auger electron appearance potential spectroscopy [517] where the effective escape depth is determined by the inelastic mean free paths of the both Auger and primary electrons. To illustrate the influence of the enhanced surface sensitivity on the signal spectra and to analyse other features of APECS in more detail, we consider a recent example of application of the coincidence technique to studies of the Ga $L_{23}M_{45}M_{45}$ Auger line of Ga As [516].

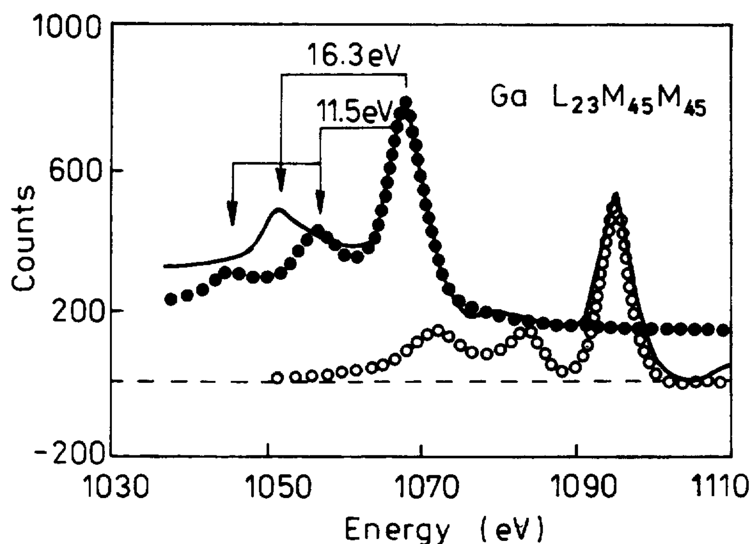

Fig. 46. The $L_{23}M_{45}M_{45}$ Auger line of Ga (GaAs) in coincidence with the $2p_{3/2}$ (filled circles) and $2p_{1/2}$ (open circles) photoelectrons. The solid line represents the singles spectrum from the $2p_{3/2}$ data. The expected positions of bulk (16.3 eV) and surface (11.5 eV) plasmons below the main $L_3M_{45}M_{45}$ and $L_2M_{45}M_{45}$ peaks are shown by arrows [516].

Figure 46 shows the singles and the coincidence spectra of the Ga $L_{23}M_{45}M_{45}$ Auger line recorded by Thurgate et al. [516]. The spectra obtained in coincidence with $2p_{3/2}$ (filled circles) and $2p_{1/2}$ (open circles) photoelectrons are scaled to the same height as the singles spectrum. The displayed coincidence spectra represent the three Gaussian fits to the experimental data-points. The singles spectrum (solid curve) has a large satellite at the energy loss of about 16.3 eV, which is presumably associated with bulk plasmon excitation [518–520]. Contrary to this, the coincidence spectra do not exhibit any noticeable peaks at 16.3–eV energy losses. On the other hand, the

coincidence Auger spectra show at least two smaller satellites at multiples of 11.5 eV below the main peak [516]. Analysing the positions of the atomic terms in the Ga DOS [521] and comparing the behaviour of the singles and coincidence spectra in the region of the main peaks Thurgate et al. [516] came to the conclusion that multiple hole DOS processes do not contribute to the low energy part of the spectra. They found that the satellites in the $L_3M_{45}M_{45}$ (filled circles) spectrum were not due to any transitions associated with a Coster–Kronig process. Clear evidence that the 16.3–eV satellite in the $2p_{3/2}$ photoelectron spectrum is not due to a shake-up/off effect is provided by absence of any coincidence when fixing the photoelectron analyser at 16.3 eV below the main peak in the $2p_{3/2}$ photoelectron spectrum (not shown) and scanning the $L_3M_{45}M_{45}$ Auger line. Additional scanning of the $2p_{3/2}$ phoelectron energy spectrum in coincidence with the satellite (16.3 eV) on the lower energy side of the Ga $L_3M_{45}M_{45}$ Auger peak showed that this Auger satellite had no preferable origin in the photoelectron spectrum [516]. Thus, the smaller peak at the 16.3 eV energy loss in the singles spectrum can be attributed to extrinsic processes *i.e.*, excitation of the bulk plasmon. The frequency of the surface plasmon is $\omega_s = \omega/\sqrt{2}$, where $\hbar\omega$ is the bulk plasmon energy. In the case considered, the surface plasmon energy is about 11.5 eV. Therefore, the satellites in the coincidence spectra are most probably associated with surface excitations. Comparing the singles and the coincidence energy distributions from Fig. 46 one can easily see that bulk plasmon excitation is much more weakly pronounced in the coincidence spectra. Such a result is in full agreement with the enhanced surface sensitivity of APECS. The ability of APECS to suppress bulk excitations was also demonstrated by Jensen et al. [515] for the Al(111) 2p photoelectron spectrum, taken at 200 eV photon energy in coincidence with the $L_{23}VV$ Auger line (fixed analyser at 69 eV). On the basis of qualitative assessments, the authors of ref. [515] found that the bulk-plasmon-loss region in the coincidence spectrum is suppressed by about 40% with respect to the singles one. However, a more accurate quantitative analysis is needed to describe relative contributions of intrinsic and extrinsic processes to the coincidence energy distributions in the near peak region. In effect, taking into account the results of multiple scattering theory (*cf.* Section 3) one can state that the bulk plasmon excitation can be either suppressed or enhanced in APECS spectra, depending on the XPS geometry.

In contrast to a GaAs sample the structure of the $L_{23}VV$ Auger peaks of Ni, Co and Cu is strongly influenced by Coster–Kronig transitions [507–509]. For example, the peak-to-peak ratio for the L_3VV and L_2VV Auger lines in Co is 7.4 and, therefore, is in seeming disagreement with the relative multiplicity of $2p_{3/2}$ and $2p_{1/2}$ states [503,509]. Decomposing the L_3VV peak into the sum of the L_3VV ($2p_{3/2}$) and the L_2L_3V-L_3VV ($2p_{1/2}$) lines (the latter process involves the

Coster–Kronig transition between the L_2 and L_3 subshells with a intermediate vacancy in the L_3 subshell, decaying later on through the L_3VV Auger emission) provides an explanation. Indeed, the ratio of intensities of the L_3VV ($2p_{3/2}$) line to the overall intensity of the L_2L_3V-L_3VV ($2p_{1//2}$) and L_2VV ($2p_{1/2}$) peaks is 2:1 as expected [503].

The APECS measurements of N_7VV Auger spectra from the outermost surface layer of Ta(100) and from the bulk Ta(100) lead to a discovery of the existence of a surface-to-bulk interatomic Auger decay mechanism [513]. In this new channel of Auger decay the 4f hole of the surface Ta atom hops to an adjacent bulk site. The newly created vacancy is then neutralized through a usual N_7VV Auger process as there is no core-level with lower binding energy, in the vicinity of the bulk atom, into which the hole may drop. The opposite process (in the direction from bulk to surface) may occur if the vacancy in a core-level of a bulk atom lies lower on the energy scale than that in a neighbouring surface atom. This suggestion is fully supported by experiments with a TaC(111) sample for which a surface Ta $4f_{7/2}$ level is shifted 0.56 eV to lower binding energy than the bulk line [513].

In APECS, a vacancy in a core-shell is produced by incident x-rays. Another option would be to use a beam of primary electrons for the same purpose. Then, recording an Auger electron spectrum in coincidence with a scattered core-loss electron can, in principle, provide an additional means for surface analysis. Among the clear advantages of this method, there are (1) a relatively cheap electron-beam production and (2) a possibility of continuous variation of the energy of a scattered electron [24]. Assessments show, however, that an electron-excited experiment is more difficult than the photoexcited one as the signal-to-background ratio is at least by the order of magnitude lower than in the case of APECS [522]. These assessments have been made so far for normal incidence of an electron beam on a Si target within the first-order approximation with respect to elastic scattering of a primary electron, followed or preceded a core-shell ionization event. The signal-to-noise ratio may be essentially different for grazing incidence and heavier targets when backscattering process is dominated by multiple elastic collisions. Thus, the question of practical importance of Auger-electron core-loss electron coincidence spectroscopy still remains open.

6. Conclusion

The information obtained from AES/XPS experiments can be divided into two classes: chemical composition determination based on peak-shape and core-level energy shift analysis and structure characterization. Although the elemental composition analysis of the near surface region is and will be an important part of a routine work of a spectroscopist more and more attention is paid now to extracting data about the structure of top monolayers. Those include atomic site locations, bond lengths and orientation, degree of ordering in different directions and so on. Structural information together with knowledge of chemical composition is expected to provide us with a deeper understanding of surfaces, which is a necessary step further to the ultimate goal of predicting the surface properties from first principles [488]. In recent years, quantitative AES/XPS analysis has been emerging as a multiple- discipline area of scientific research. Its physical foundation embraces many fields of atomic physics, theories of electron diffraction and linear transport. Electron excitation processes and subsequent interaction of signal electrons with a sample constitutes a great deal of both chemistry and physics. That is probably the reason for strong coupling of surface analysis with fundamental studies [9]. Progress made in analytical description of multiple incoherent scattering of signal electrons opens new possibilities for accurate interpretation of experimental data in the case of amorphous and polycrystalline solids. However, a formalism that would enable us to explain in a consistent way all features of electron diffraction and incoherent scattering in crystalline targets still remains to be developed. Thus, the gap between the quantum-mechanical and the classical approaches has to be bridged in the years to come.

Acknowledgements

Two of the authors (I.S.T. and A.J.) would like to acknowledge the support by Research Project KBN 2P03B 009 10.

References

1. C.S.Fadley, Surf.Sci.Repts., **19**, 231 (1993).
2. A.Szoke, in: *Short Wavelength Coherent Radiation: Generation and Applications*, R.Z.Bachrach (Ed.), Plenum Press, New York (1992).
3. J.J.Barton, Phys.Rev.Lett., **61**, 1356 (1988).
4. J.J.Barton, J.Electron Spectrosc.Relat.Phenom., **51**, 37 (1990).
5. C.S.Fadley, J.Electron Spectrosc.Relat.Phenom., (1996) in press.
6. H.W.Haak, G.A.Sawattzki, L. Ungier, J.K.Gimzewski and T.D.Thomas, Rev. Sci.Instrum., **55**, 696 (1984).
7. E.Jensen, R.A.Bartynski, M.Weinert, S.L.Hulbert, E.D.Johnson and R.F.Garret, Phys.Rev., **B 41**, 468 (1990).
8. T.A.Carlson, *Photoelectron and Auger Spectroscopy*, Plenum Press, New York (1975).
9. A.D.Baker and C.R.Brundle in *Electron Spectroscopy: Theory, Techniques and Applications*, C.R.Brundle and A.D.Baker, (Eds.), Academic Press, New York (1977) v.1, p.2.
10. W.L.Jolly in *Electron Spectroscopy: Theory, Techniques and Applications*, C.R.Brundle and A.D.Baker, (Eds.), Academic Press, New York, (1977) v.1, p.119.
11. C.S.Fadley, in *Electron Spectroscopy: Theory, Techniques and Applications*, C.R.Brundle and A.D.Baker, (Eds.), Academic Press, New York (1978) v.2, p.2.
12. D.Briggs in *Electron Spectroscopy: Theory, Techniques and Applications*, C.R.Brundle and A.D.Baker, (Eds.), Academic Press, New York, (1979) v.3, p.306.
13. A.Dilks in *Electron Spectroscopy: Theory, Techniques and Applications*, C.R.Brundle and A.D.Baker, (Eds.), Academic Press, New York (1981) v.4, p.277.
14. G.E.McGuire and P.H.Holloway in *Electron Spectroscopy: Theory, Techniques and Applications*, C.R.Brundle and A.D.Baker, (Eds.), Academic Press, New York (1981) v.4, p.2.
15. D.Briggs and M.P.Seah, *Practical Surface Analysis by Auger and X-ray Photoelectron Spectroscopy*, D.Briggs and M.P.Seah (Eds.) Wiley, New York (1990).
16. C.J.Powell and M.P.Seah, J.Vac.Sci.Technol., **A 8**, 735 (1989).
17. C.S.Fadley, in *Synchrotron Radiation Research: Advances in Surface and Interface Science, Volume 1: Techniques*, R.Z.Bachrach (Ed.), Plenum Press, New York, 1992, p.421.
18. S.Mroz, Prog.Surf.Sci., **461**, 377 (1994).
19. ASTM Standard E 673-93, *Standard Terminology Relating to Surface Analysis, Annual Book of Standards*, ASTM, Philadelphia (1994) v.3.06, p.739.
20. C.J.Powell, Rev.Mod.Phys., **48**, 33 (1976).
21. C.J.Powell, in *Electron Impact Ionization*, T.D.Mark and G.H.Dunn (Eds.), Springer-Verlag, New York, Wien (1985) p.198.
22. C.J.Powell, in *Microbeam Analysis*, J.R.Michael and P.Ingram (Eds.), San Francisco Press, San Francisco, (1990) p.13.
23. H.Bethe, Ann.Physik, **5**, 325 (1930).
24. M.Gryzinski, Phys.Rev., **138**, A336 (1965).
25. M.R.H.Rudge and S.B.Schwartz, Proc.Phys.Soc., **88**, 563 (1966).
26. E.J.McGuire, Phys.Rev., **A 16**, 73 (1977).
27. K.Omidvar, J.Phys., **B 10**, L55 (1977).
28. E.J.McGuire, Phys.Rev., **A 20**, 445 (1979).
29. R.F.Egerton, Ultramicroscopy, **4**, 169 (1979).
30. R.D.Leapman, P.Rez and D.F.Mayers, J.Chem.Phys., **72**, 1232 (1980).
31. D.L.Moores, L.B.Golden and D.H.Sampson, J.Phys., **B 13**, 385 (1980).
32. P.Rez, X-ray Spectrometry, **13**, 55 (1984).
33. J.Botero and J.H.Macek, Phys.Rev., **A 45**, 154 (1992).

34. C.T.Whelan, R.J.Allan, H.R.Walters and X.Zhang, in *(e,2e) and Related Processes*, C.T.Whelan, H.R.J.Walters, A.Lahmann-Bennami and H.Ehrhardt (Eds.), Kluwer, Dordrecht, (1993), p.1.
35. S.Keller, C.T.Whelan, H.Ast, H.R.Walters and R.M.Dreizler, Phys.Rev., **A 50**, 3865 (1994).
36. L.D.Landau and I.M.Lifshitz, *Quantum Mechanics: Non-Relativistic Theory*, 3rd Edition, Pergamon Press, Oxford, New York, (1977).
37. T.P.Schreiber and A.M.Wims, Ultramicroscopy **6**, 323 (1981).
38. P.Schwaab, Scanning, **9**, 1 (1987).
39. H.Hoeft and P.Schwaab, X-ray Spectroscopy, **17**, 201 (1988).
40. S.F.Schnatterly, in *Solid State Physics*, H.Ehrenreich, F.Seitz and F.Turbull (Eds.), Academic Press, New York, (1979) v.34, p.275.
41. H.Raether, *Springer Tracts in Modern Physics*, Springer, Berlin, (1980), v.88, p.1.
42. C.J.Powell, in *Electron Beam Interactions with Solids for Microscopy, Microanalysis and Microlithography*, D.F.Kyser, D.F.Newbury, H.Niedrig and R.Shimizu (Eds.), Scanning Electron Microscopy, Chicago (1984), p.19.
43. X.Zhang, C.T.Whelan, H.R.J.Walters, R.J.Allan, P.Bickert, W.Hink and W.Schonberger, J.Phys., **B 25**, 4325 (1992).
44. A.Lahmam-Bennami, H.F.Wellenstein, A.Duguet and A.Daoud, Phys.Rev., **A 30**, 1511 (1984).
45. G.Stefani, L.Avaldi, A.Lahmam-Bennami and A.Duguet, J.Phys., **B 19**, 3787 (1986).
46. L.Avaldi, R.Camilloni and G.Stefani, Phys.Rev., **A 41**, 134 (1990).
47. G.H.Wannier, Phys.Rev., **90**, 817 (1953).
48. U.Fano, Rep.Prog.Phys., **46**, 97 (1983).
49. J.Jessenberger and W.Hink, Z.Physik, **A 275**, 331 (1975).
50. C.-N.Chang, Phys.Rev., **A 19**, 1930 (1979).
51. K.Shima, Phys.Letters, **77 A**, 237 (1980).
52. K.Shima, T.Nakagawa, K.Umetani and K.Mikumo, Phys.Rev., **A 24**, 72 (1981)
53. R.Hippler, I.McGregor, M.Aydinol and H.Kleinpoppen, Phys.Rev., **A 23**, 1730 (1981).
54. C.Quarles and M.Semaan, Phys.Rev., **A 26**, 3147 (1982).
55. W.Hink, I.Kees., H.-P.Schmidt and A.Wolf, in *Inner-Shell and X-ray Physics of Atoms and Solids*, I.Fabian, D.I.Kleinpoppen and L.M.Watson (Eds.), Plenum Press, New York (1981) p.327.
56. R.Peterkop, J.Phys., **B 4**, 513 (1971).
57. H.-W.Drawin, Z.Physik, **164**, 513 (1961).
58. M.Green and V.I.Cosslett, Proc.Phys.Soc., **78**, 1206 (1961).
59. G.Glupe and W.Mehlhorn, J.Phys., **C 4**, 40 (1971).
60. P.Auger, Comp.Rend.Acad.Sci., **180**, 1939 (1925).
61. P.Auger, J.Phys.Rad., **6**, 205 (1925).
62. D.Coster and R.de L.Kronig, Physica, **2**, 13 (1935).
63. E.S.Parilis, *Ozher Effekt (The Auger Effect)*, FAN, (Academy of Sciences, UzSSR), Tashkent, (1969) (in Russian).
64. W.Bambinek, B.Crasermann, R.W.Fink, H.U. Freund, N.Mark, C.D.Swift, R.E.Price and P.V.Rao, Rev.Mod.Phys., **44**, 716 (1972).
65. E.H.S.Burhop, *The Auger Effect and Other Radiationless Transitions*, Cambridge U.P., Cambridge, (1952).
66. J.L.Powell and B.Crasemann, *Quantum Mechanics*, Addison-Wesley, Reading Mass. (1961).
67. E.J.McGuire, Phys.Rev., **A 3**, 587 (1971).
68. H.S.W.Massey and E.H.S.Burhop, Proc.Roy.Soc., (London) **A 153**, 661 (1936).
69. W.N.Asaad and E.H.S.Burhop, Proc.Phys.Soc., (London) **71**, 369 (1958).

70. E.J.Callan, Phys.Rev., **124**, 793 (1961).
71. D.Chattarji and B.Talukdar, Phys.Rev., **174**, 44 (1968).
72. V.O.Kostroun, M.N.Chen and B.Crasemann, Phys.Rev., **A 3**, 533 (1971).
73. D.Chattarji, *The Theory of Auger Transitions*, Academic Press, New York (1976).
74. W.Mehlhorn, Z.Phys., **208**, 1 (1968).
75. E.J.McGuire, Phys.Rev., **185**, 1 (1969).
76. E.J.McGuire, Phys.Rev., **A 2**, 273 (1970).
77. C.P.Bahlla and D.J.Ramsdale, Z.Physik, **239**, 95 (1970).
78. D.L.Walters and C.P.Bahlla, Phys.Rev., **A 3**, 519 (1971).
79. J.W.Byrne and N.Howarth, J.Phys., **B 3**, 280 (1970).
80. E.H.S.Burhop and W.H.Asaad, Adv.Atom.Mol.Phys., **8**, 164 (1972).
81. J.C.Fuggle, in *Electron Spectroscopy: Theory, Techniques and Applications*, C.R.Brundle and A.D.Baker (Eds.), Academic Press, New York, (1981) v.4, p.85.
82. G.K.Wertheim, in *Electron Spectroscopy: Theory, Techniques and Applications*, C.R.Brundle and A.D.Baker (Eds.) Academic Press, New York, (1978) v.2, p.259.
83. J.Reader, Phys.Rev., **A 7**, 1431 (1973).
84. Y.Yafet andd R.E.Watson, Int.J.Quant.Chem.Symp. **7**, 93 (1973).
85. J.T.J.Huang and J.W.Rablais, in *Electron Spectroscopy: Theory, Techniques and Applications*, C.R.Brundle and A.D.Baker, (Eds.), Academic Press, New York, (1978) v.2, p.225.
86. S.T.Manson and D.Dill, in *Electron Spectroscopy: Theory, Techniques and Applications*, C.R.Brundle and A.D.Baker (Eds.) Academic Press, New York, (1978) v.2, p.1.
87. L.I.Schiff, *Quantum Mechanics*, McGraw-Hill, New York (1968).
88. F.Wuilleumier and M.O.Krause, Phys.Rev., **A 10**, 242 (1974).
89. I.M.Band, Yu.I.Kharitonov and M.B.Trzhaskovskaya, At. Data Nucl. Data Tables, **23**, 443 (1979).
90. D.S.Kennedy and S.T.Manson, Phys.Rev., **A 5**, 227 (1972).
91. M.Tinkham, *Group Theory and Quantum Mechanics*, McGraw-Hill, New York, (1964).
92. J.Callaway, *Quantum Theory of the Solid State*, Academic Press, New York, London, (1974).
93. U.Fano, Phys.Rev., **124**, 1866 (1961).
94. F.Mies, Phys.Rev., **175**, 164 (1968).
95. P.G.Burke, Adv.Atom.Molec.Phys., **4**, 173 (1968).
96. P.G.Burke and M.J.Seaton, Methods Comp.Phys., **10**, 2 (1971).
97. K.Smith, *The Calculation of Atomic Collision Processes*, Wiley–Interscience, New York, (1971).
98. P.G.Burke and W.D.Robb, J.Phys., **B 5**, 44 (1972).
99. P.G.Burke and W.D.Robb, Adv.Atom.Molec.Phys., **11**, 144 (1975).
100. K.A.Brueckner, Phys.Rev., **97**, 1353 (1955).
101. K.A.Brueckner, *The Many-body Problem*, Wiley, New York, (1959).
102. J.Goldstone, Proc.Roy.Soc., **A 239**, 267 (1957).
103. M.Ya.Amusia, N.A.Cherepkov and L.V.Chernysheva, Sov.Phys.-JETP, **33**, 90 (1971).
104. P.L.Atlick and A.E.Glassgold, Phys.Rev., **133** A632 (1964).
105. M.Ya.Amusia, in *Atomic Physics*, G.K.Woodgate and P.G.H.Sandars, (Eds.), Plenum, London and New York, (1971) v.2, p.249.
106. M.Ya.Amusia and N.S.Cherepkov, Case Stud.Atom.Phys., **5**, 47 (1975).
107. G.Wendin, in *Photoionization and Other Probes of Many-electron Interaction*, F.Wuilleumier (Ed.) Plenum Press, New York (1976) p.61.
108. V.Radojevic and W.R.Johnson, J.Phys., **B 16**, 177 (1983).
109. N.Shanthi and P.C.Deshmukh, J.Phys., **B 23**, 61 (1990).
110. M.Kutzner, D.Winn and S.Mattingly, Phys.Rev., **A 48**, 404 (1993).

111. M.Kutzner and V.Radojevic, Phys.Rev., **A 49**, 2574 (1994).
112. M.Kutzner and S.E.Vance, Phys.Rev., **A 50**, 4836 (1994).
113. W.Kohn, Phys.Rev., **74**, 1963 (1948).
114. J.H.Scofield, Report No. UCRL-51326, Lawrence Livermore Laboratory (1973).
115. Keh-Ning Huang, Phys.Rev., **A 22**, 223 (1980).
116. M.O.Krause, Phys.Rev., **177**, 151 (1969).
117. J.C.Riviere, in *Practical Surface Analysis by Auger and X-ray Photoelectron Spectroscopy*, D.Briggs and M.P.Seah (Eds.), Wiley, New York, (1983) p.17.
118. M.V.Berry and K.E.Mount, Rep.Prog.Phys. **35**, 315 (1972).
119. M.V.Berry, Proc.Phys.Soc., **89**, 285 (1966).
120. W.C.Fon and K.A.Berrington, J.Phys. **B 14**, 323 (1981).
121. A.Temkin, Phys.Rev., **107**, 1004 (1957).
122. D.G.Thomson, J.Phys., **B 4**, 468 (1971).
123. F.W.Byron Jr. and C.J.Joachain, Phys.Rev., **A 15**, 128 (1977).
124. I.E.McCarthy, C.J.Noble, B.A.Philips, A.D.Turnbull, Phys.Rev., **A 15**, 2173 (1977).
125. J.K.O'Connell and U.F.Lane, Phys.Rev., **A 27**, 1893 (1983).
126. I.S.Tilinin, Zh.Eksp.Teor.Fiz., **94**, 96 (1988) [Sov.Phys.JETP, 67, 1570 (1988)].
127. N.F.Mott and H.S.W.Massey, *The Theory of Atomic Collisions*, Clarendon Press, Oxford (1965).
128. J.Heading, *An Introduction to Phase-integral Methods*, Methuen, London (1962).
129. J.Burgdorfer, C.O.Reinhold, J.Sternberg and J.Wang, Phys.Rev., **A 51**, 1248 (1995).
130. S.-R.Lin, N.Scherman and J.K.Percus, Nucl.Phys., **45**, 492 (1963).
131. P.J.Bunyan and J.K.Schonfelder, Proc.Phys.Soc., **85**, 455 (1965).
132. D.Walker, Adv.Phys., **20**, 257 (1971).
133. K.Hasenburg, D.H.Madison, K.Bartschaft and K.Blum, J.Phys., **B 19**, 1803 (1986).
134. A.Jablonski, Phys.Rev., **B 43**, 7546 (1991).
135. R.A.Bonham and T.G.Strand, J.Chem.Phys., **39**, 2200 (1963).
136. R.Garvey, C.Jackman and A.E.S.Green, Phys.Rev., **A 12**, 1144 (1975).
137. J.F.Williams and A.Crowe, J.Phys., **B 8**, 2233 (1975).
138. R.H.Jansen and F.J. de Heer, J.Phys., **B 9**, 213 (1976).
139. I.S.Tilinin, Phys.Rev., **A 51**, 3058 (1995).
140. S.K.Skrivastava, A.Shutjan, S.Trajmar, J.Chem.Phys., **64**, 1340 (1976).
141. I.Iga, Lee Mu-Tao, J.C.Nogueira and R.S.Barbieri, J.Phys., **B 20**, 105 (1987).
142. D.F.Register and S.Trajmar, Phys.Rev., **A 29**, 1785 (1984).
143. M.R.Riley, C.J.McCallum and F.Biggs, Atom.Data and Nucl.Data Tables, **15**, 443 (1975).
144. M.Hayashi, J.Phys., **D.16**, 581 (1983).
145. I.S.Tilinin and W.S.M.Werner, Phys.Rev., **B 46**, 13739 (1992).
146. A.Jablonski and I.S.Tilinin, J.Electron Spectrosc.Relat.Phenom., **74**, 207 (1995).
147. M.I.Ryazanov and I.S.Tilinin, *Issledovaniye Poverkhnosti po Obratnomu Rasseyaniyu Chastitz (Surface Analysis by Particle Backscattering)*, Energoatomizdat, Moscow, (1985) (in Russian).
148. R.H.Ritchie, Phys.Rev., **106**, 874 (1957).
149. J.Lindhard, Kgl.Danske Videnskab.Selskab, Mat.-fys. Medd., **28** No.8 (1954).
150. C.J.Tung, Y.F.Chen, C.M.Kwei and T.L.Chou, Phys.Rev., **B 49**, 16684 (1994).
151. D.Pines, Phys.Rev., **92**, 626 (1953).
152. D.Bohm and D.Pines, Phys.Rev., **92**, 609 (1953).
153. D.Bohm and D.Pines, Phys.Rev., **82**, 625 (1951).
154. D.Pines and D.Bohm, Phys.Rev., **85**, 338 (1952).
155. J.J.Quinn and R.A.Ferrell, Phys.Rev., **112**, 812 (1958).

156. R.H.Ritchie, Phys.Rev., **114**, 644 (1959).
157. J.J.Quinn, Phys.Rev., **126**, 1453 (1962).
158. L.Kleinman, Phys.Rev., **B 3**, 2982 (1971).
159. A.P.Pathak and M.Yussouff, Phys.Status Solidi, **B 49**, 431 (1972).
160. J.C.Shelton, Surf.Sci., **44**, 305 (1974).
161. D.R.Penn, Phys.Rev., **B 13**, 5248 (1976).
162. C.J.Tung and R.H.Ritchie, Phys.Rev., **B 16**, 4302 (1977).
163. J.C.Ashley, C.J.Tung and R.H.Ritchie, Surf.Sci., **81**, 409 (1979).
164. C.J.Tung, J.C.Ashley and R.H.Ritchie, Surf.Sci., **81**, 427 (1979).
165. D.R.Penn, Phys.Rev., **B 35**, 482 (1987).
166. C.M.Kwei, Y.F.Chen, C.J.Tung and J.P.Wang, Surf.Sci., **293**, 202 (1992).
167. F.Yubero and S.Tougaard, Phys.Rev., **B 46**, 2486 (1992).
168. C.J.Tung, Y.F.Chen, C.M.Kwei and T.L.Chou, Phys.Rev., **B 49**, 16684 (1994).
169. V.U.Nazarov, Phys.Rev., **B 49**, 10663 (1994).
170. V.U Nazarov, Phys.Rev., **B 49**, 17342 (1994).
171. S.Tanuma, C.J.Powell and D.R.Penn, Surf.Interface Anal., **11**, 577 (1988).
172. J.C.Ashley, J.Electron Spectrosc.Relat.Phenom., **46**, 199 (1988).
173. D.Pines and P.Nozieres, *Quantum Liquids*, W.A.Benjamin, New York, (1966) v.1, p.308.
174. D.Y.Smith, in *Handbook of Optical Constants of Solids*, E.D.Palik (Ed.), Academic Press, New York, (1985).
175. G.D.Mahan, Many Particle Physics, Plenum, New York, (1981) p.460.
176. S.Tanuma, C.J.Powell and D.R.Penn, Surf.Interface Anal., **17**, 911 (1991).
177. S.Tanuma, C.J.Powell and D.R.Penn, Surf.Interface Anal., **17**, 927 (1991).
178. S.Tanuma, C.J.Powell and D.R.Penn, Surf.Interface Anal., **21**, 165 (1993).
179. Z.-J.Ding and R.Shimizu, Surf.Sci., **222**, 313 (1989).
180. C.D.Wagner, L.E.Davis and W.M.Riggs, Surf.Interface Anal., **2**, 53 (1980).
181. J.C.Ashley and C.J.Tung, Surf.Interface Anal., **4**, 52 (1982).
182. J.C.Ashley, J.Electron Spectrosc.Relat.Phenom., **28**, 177 (1982).
183. J.Szajman, J.Liesengang, J.G.Jenkins and R.C.G.Leckey, J.Electron Spectrosc.Relat. Phenom., **23**, 97 (1981).
184. T.Reich, V.G.Varzhemski and V.T.Nefedov, J. Electron Spectrosc. Relat. Phenom., **46**, 255 (1988).
185. M.Inokuti, Rev.Mod.Phys., **43**, 297 (1971).
186. C.J.Powell, J.Electron Spectrosc.Relat.Phenom., **47**, 197 (1988).
187. R.Schmidt, PhD Thesis, Universitaet Tubingen (1982).
188. A.Jablonski, P.Mrozek, G.Gergely, M.Menyhard and A.Sulyok, Surf. Interface Anal., **6**, 291 (1984).
189. A.Jablonski, Surf.Sci., **151**, 166 (1985).
190. W.Dolinski, H.Nowicki and S.Mroz, Surf.Interface Anal., **11**, 229 (1988).
191. W.Dolinski, S.Mroz and M.Zagorski, Surf.Sci., **200**, 361 (1988).
192. B.Lesiak, A.Jablonski, Z.Prussak and P.Mrozek, Surf.Sci., **223**, 213 (1989).
193. A.Jablonski, B.Lesiak, G.Gergely, Phys.Scripta, **39**, 363 (1989).
194. W.Dolinski, S.Mroz, J.Palczynski, B.Gruzza, P.Bondot and A.Porte, Acta Phys.Polon., **A 82**, 193 (1992).
195. H.Beilschmidt, I.S.Tilinin and W.S.M.Werner, Surf.Interface Anal., **22**, 120 (1994).
196. G.Gergely, M.Menyhard, K.Pentek, A.Sulyok, A.Jablonski and B.Lesiak, Vacuum **46**, 591 (1995).
197. Y.F.Chen, J.Vac.Sci.Technol. **A 13**, 2665 (1995).
198. A.Jablonski, J.Gryko, J.Kaaer and S.Tougaard, Phys.Rev., **B 39**, 61 (1989).

199. K.Jacobi and J.Holzl, Surf.Sci., **26**, 54 (1971).
200. R.G.Steinhard, J.Hudis and M.L.Perlman, Phys.Rev., **B 5**, 1016 (1972).
201. C.Martin, E.T.Arakawa, T.A.Callcott and J.C.Ashley, J.Electron Spectrosc. Relat. Phenom., **35**, 307 (1985).
202. W.S.M.Werner, I.S.Tilinin and M.Hayek, Phys.Rev., **B 50**, 4819 (1994)
203. S.Tougaard and J.Kraaer, Phys.Rev., **B 43**, 1651 (1991).
204. F.Yubero, S.Tougaard, E.Elizalde and J.M.Sanz, Surf. Interface Anal., **20**, 719 (1993).
205. A.Jablonski and H..Ebel, Surf.Interface Anal., **11**, 627 (1988).
206. M.P.Seah and W.A.Dench, Surf.Interface Anal., **1**, 2 (1979).
207. I.S.Tilinin, A.Jablonski, J.Zemek and S.Hucek, in Abstracts. 6th Europ. Conf. on Applications of Surf. and Interface Anal., H.J.Mathieu, (Ed.), Congr.Center, Montreux, Switzerland (1995) p.QA-13.
208. I.S.Tilinin and W.S.M.Werner, Mikrochim.Acta, **114/115**, 485 (1994).
209. I.M.Bronstein and B.S.Freiman, *Vtorichnaya Elektronnaya Emissiya (Secondary Electron Emission)*, Nauka, Moscow (1969) (in Russian).
210. S.L.Dudarev and M.I.Ryazanov, Zh.Eksp.Teor.Fiz., **88**, 631 (1985).
211. K.Blum, *Density Matrix; Theory and Applications*, Plenum Press, New York (1982).
212. S.L.Dudarev and M.I.Ryazanov, Zh.Eksp.Teor.Fiz. **85**, 1748 (1983).
213. S.L.Dudarev and M.I.Ryazanov, Acta Crystallogr. **A 44**, 51 (1988).
214. S.L.Dudarev, L.-M.Peng and M.J.Whelan, Phys.Lett., **A 170**, 111 (1992).
215. L.-M.Peng, S.L.Dudarev and Whelan, Phys.Lett., **A 175**, 461 (1993).
216. S.L.Dudarev,L.-M.Peng and M.J.Whelan, Phys.Rev., **48**, 13408 (1993).
217. S.L.Dudarev, D.D.Vvedenski and M.J.Whelan, Phys.Rev. **B 50**, 14525 (1994).
218. S.L.Dudarev, P.Rez, M.J.Whelan, Phys.Rev., **B 51**, 3397 (1995).
219. K.M.Case and P.Zweifel, *Linear Transport Theory*, Addison-Wesley, Reading, MA (1967).
220. N.N.Bogolubov, *Problemi Dinamicheskoi Teorii v Statisticheskoi Fizike (Problems of Dynamical Theory in Statistical Physics)*, Selected works in three volumes, v.2, Naukova Dumka, Kiev (1970) (in Russian).
221. I.S.Tilinin, Postdoctoral thesis, Moscow Engineering Physics Institute, Moscow (1993) (in Russian).
222. J.R.Mika, Nucl.Sci.Eng., **11**, 415 (1961).
223. N.J.McCormick and I.Kuscer, J.Math.Phys., **7**, 2036 (1966).
224. W.S.M.Werner and I.S.Tilinin, Appl.Surf.Sci., **70/71**, 29 (1993).
225. V.V.Sobolev, *Rasseyaniye sveta v atmospherah planet (Light Scattering in Planet Atmospheres)*, Nauka, Moscow (1972) (in Russian).
226. A.Jablonski and S.Tougaard, Surf.Interface Analysis, **22**, 129 (1994); *Standard Reference Data Program*, National Institute of Standards and Technology, Gaitherburg, MD 20899 (1995).
227. J.M.Hammersley and D.C.Handscomb, *Monte Carlo Methods*, Methuen, London (1967).
228. B.Adler, S.Fernback and M.Rotenberg, (Eds.) *Methods in Computational Physics*, Academic Press, New York, (1963) v.1, p.135.
229. H.Bishop, in *X-ray Optics and Microanalysis*, R.Castaing, P.DesChamps and J.Philibert (Eds.), Herman, Paris, (1965), p.112.
230. R.Shimizu, K.Murata and G.Shinoda in *X-ray Optics and Microanalysis*, R.Castaing, P.DesChamps and J.Philibert (Eds.), Herman, Paris, (1965), p.127.
231. L.Reimer, Optik, **27**, 86 (1968).
232. L.Reimer and D.Stelter, Scanning, **8**, 265 (1986).
233. H.A.Bethe, Ann.Phys., **5**, 325 (1930).
234. D.R.Penn, Phys.Rev., **B 35**, 482 (1985).

235. R.H.Ritchi, Phys.Rev., **106**, 874 (1957).
236. J.C.Ashley and R.H.Ritchi, Phys.Rev., **5**, 3485 (1972).
237. R.Shimizu and Ding Ze-jin, Rep.Prog.Phys., **55**, 487 (1992).
238. Z.-J.Ding and R.Shimizu, Surf.Sci., **222**, 313 (1989).
239. R.Shimizu, Jpn.J.Appl.Phys., **22**, 1631 (1983).
240. W.H.Press, B.P.Flannery, S.A.Teukolsky and W.T.Vetterling, *Numerical recipes. The art of Scientific Computing*, Cambridge University Press, Cambridge (1986).
241. I.S.Tilinin and W.S.M.Werner, Surf.Sci., **290**, 119 (1993).
242. I.S.Tilinin, A.Jablonski and S.Tougaard, Phys.Rev., **B 52**, 5935 (1995).
243. A.Jablonski and H.Ebel, Surf.Interface Anal., **6**, 21 (1984).
244. W.S.M.Werner, Surf.Sci., **251/252**, 336 (1991).
245. A.Jablonski, Surf.Interface Anal., **21**, 758 (1994).
246. W.H.Gries and W.S.M.Werner, Surf.Interface Anal., **16**, 149 (1990).
247. W.S.M.Werner, W.H.Gries and H.Stori, J.Vac.Sci.Technol., **A 9**, 21 (1991).
248. W.S.M.Werner, W.H.Gries and H.Stori, Surf.Interface Anal., **17**, 693 (1991).
249. P.Cumpson, Surf.Interface Anal., **20**, 727 (1993).
250. P.F.A.Alkemade, K.Werner, S.Radelaar and W.G.Sloof, Appl. Surf. Sci., **70/71**, 24 (1993).
251. P.F.A.Alkemade, Surf.Interface Anal., **23**, 251 (1995).
252. W.S.M.Werner, I.S.Tilinin and A.Jablonski, Surf.Interface Anal., **23**, 823 (1995).
253. A.Jablonski, Surf.Sci., **188**, 164 (1987).
254. W.S.M.Werner, Quantitation of Electron Spectroscopic Techniques (QUEST V0.7) a software packet, http://eaps1.tuwien.ac.at/werner/ (1996).
255. A.C.Yates, Comp.Phys.Comm., **2**, 175 (1971).
256. Ding Ze-jun and R.Shimizu, Surf.Sci., **179**, 539 (1988).
257. E.D.Palik (Ed.), *Handbook of optical constants of solids*, Academic Press, New York (1985).
258. E.D.Palik, (Ed.), *Handbook of optical constants of solids II*, Academic Press, New York (1991).
259. J.H.Scofield, J.Electron Spectrosc.Relat.Phenom., **1**, 129 (1976).
260. R.F.Reilman, A.Msezane and S.T.Manson, J.Electron Spectrosc.Relat.Phenom., **8**, 289 (1976).
261. J.F.Moulder and K.Bomben, *Handbook of x-Ray Photoelectron Spectroscopy*, Physical Electronics Industries Inc., Minnesota, (1992).
262. K.Goto, N.Sakakibara and Y.Sakai, Microbeam Anal., **2**, 123 (1993).
263. K.Goto, N.Sakakibara, Y.Takeichi, Y.Namata and Y.Sakai, Surf.Interface Anal., **22**, 57 (1994).
264. K.Goto, J.Surf.Anal., **1**, 162 (1995).
265. K.Goto, in Abstracts. 6th Europ.Conf. on Applications of Surf. and Interface Anal., H.J.Mathieu (Ed.), Congr. Center, Montreux (1995) p.TD-2.
266. I.S.Tilinin, A.Jablonski and B.Lesiak-Orlowska, Acta Phys. Polon., **A 86**, 853 (1994).
267. I.S.Tilinin, A.Jablonski and B.Lesiak-Orlowska, Vacuum, **46**, 613 (1995).
268. S.Chandrasekhar, *Radiative Transfer*, Clarendon Press, Oxford (1950).
269. D.W.Johnson and J.C.H.Spence, J.Phys., **D 7**, 62 (1974).
270. M.E.Twigg, Ultramicroscopy, **10**, 291 (1982).
271. A.Tofterup, Phys.Rev., **B 32**, 2808 (1985).
272. S.Tougaard and I.Chorkendorff, Phys.Rev., **B 35**, 6570 (1987).
273. H.Yoshikawa, R.Shimizu and Z.-J.Ding, Surf.Sci., **261**, 403 (1992).
274. H.Yoshikawa, Y.Irokawa and R.Shimizu, J.Vac.Sci.Technol. **A 13**, 1984 (1995).
275. S.Tougaard, Phys.Rev., **B 34**, 6779 (1986).
276. A.Tofterup, Surf.Sci., **227**, 157 (1990).
277. S.Tougaard, Surf.Interface Anal., **11** 453 (1988).

278. L.D.Landau, J.Phys., (Moscow) **8**, 201 (1944).
279. A.L.Tofterup, Surf.Sci., **167**, 70 (1986).
280. J.Zemek and A.Jablonski, in *Physics of Solid Surfaces, Studies in Surface Science and Catalysis*, J.Koukal (Ed.) Elsevier, Amsterdam (1988), v.36, p.357.
281. A.Jablonski and J.Zemek, Phys.Rev., **B 48**, 4799 (1993).
282. V.M.Dwyer and J.A.D.Mathew, Surf.Sci., **143**, 57 (1984).
283. V.M.Dwyer and J.M.Richards, Surf.Interface Anal., **18**, 555 (1992).
284. I.S.Tilinin, A.Jablonski and B.lesiak-Orlowska, Acta Phys. Polon., **A 86**, 845 (1994).
285. I.S.Tilinin, Phys.Rev., **B 53**, 547 (1996).
286. J.Zemek, S.Hucek, A.Jablonski and I.S.Tilinin, J.Electron Spectrosc.Relat.Phenom., **76** 443 (1995).
287. C.S.Fadley, Phys.Scr., **T 17**, 39 (1987).
288. J.Osterwalder, E.A.Stewart, D.Cyr and C.S.Fadley, Phys.Rev., **B 35**, 9859 (1987).
289. W.F.Egelhoff, Phys.Rev.Lett., **59**, 559 (1987).
290. S.A.Chambers, Adv. in Phys.., **40**, 357 (1990).
291. W.F.Egelhoff and W.F.Egelhoff,Jr. Crit, Rev.Solid State Mater.Sci., **16**, 213 (1990).
292. S.A.Chambers, Surf.Sci.Repts., **16**, 261 (1992).
293. D.Naumovic, A.Stuck, T.Greber, J.Osterwalder, and L.Schlapbach, Phys. Rev. **B 47**, 7462 (1993).
294. A.Fischer, R.Fasel, J.Osterwalder, A.Krozer and L.Schlapbach, Phys.Rev. Lett., **70**, 1493 (1993).
295. R.S.Saiki, A.P.Kaduwela, J.Osterwalder, D.J.Friedman, C.S.Fadley and C.R.Brundle, Surf.Sci., **281**, 270 (1993).
296. C.S.Fadley, M.A.Van Hove, Z.Hussain and A.P.Kaduwela, J. Electron Spectrosc.Relat.Phenom. (1996) in press.
297. L.McDonnell, D.P.Woodruff and B.W.Holland, Surf.Sci., **51**, 249 (1975).
298. D.K.Saldin, G.R.Harp and B.P.Tonner, Phys.Rev., **B 45**, 9629 (1992).
299. M.Sagurton, E.L.Bullock and C.S.Fadley, Phys.Rev., **B 30**, 7332 (1984).
300. P.A.Lee, Phys.Rev., **B 13**, 5261 (1976).
301. R.W.James, *The optical principles of diffraction of X-rays*, Bell, London (1962).
302. W.S.M.Werner and I.S.Tilinin, Surf.Sci. **268**, L319 (1992).
303. L.J.Terminello, X.S.Zhang, Z.Q.Huang, S.Kim, A.E.Schach von Wittenau, K.T.Leung and D.A.Shirley, Phys.Rev., **B 38**, 3879 (1988).
304. R.S.Saiki, A.P.Kaduwela, J.Osterwalder, M.Sagurton, C.S.Fadley and C.R.Brundle, J.Vac.Sci. Technol., **A 5**, 932 (1987).
305. S.D.Ruebush, R.X.Ynzunza, S.Thevuthasan, A.P.Kaduwela, M.A.Van Hove and C.S.Fadley, Surf.Sci., **328**, 302 (1995).
306. R.S.Saiki, A.P.Kaduwela, J.Osterwalder, C.S.Fadley and C.R.Brundle, Phys. Rev., **B 40**, 1587 (1989).
307. B.F.I.Schonland, Proc.Roy.Soc., **A 104**, 235 (1923).
308. J.O.Brand, Ann.Phys., **26**, 609 (1936).
309. P.C.P.Palluel, Comp.Rend.Acad.Sci., **224**, 1492 (1947).
310. J.G.Trump and R.J. van de Graaf, Phys.Rev., **75**, 44 (1949).
311. H.Kullenkampf and Ruettiger, Z.Phys. **137**, 416 (1954).
312. H.Kullemkampf and W.Spyra, Z.Phys., **137**, 426 (1954).
313. E.J.Sternglass, Phys. Rev., **93**, 345 (1954).
314. H.Kanter, Ann.Phys., **20**, 144 (1957).
315. H.E.Bishop, in *Optique des Rayons X et Microanalyse*, Proc. IV Congr. Intern., Paris, (1965) p.153.

316. K.A.Wright and J.G.Trump, J.Appl.Phys., **33**, 687 (1962).
317. D.Harder and H.Ferber, Phys.Lett. **9**, 233 (1964).
318. F.Weinryb and J.Philibert, Comp.Rend.Acad.Sci., **258**, 4535 (1964).
319. J.L.Bienlein and G.Schlosser, Z.Phys., **174**, 91 (1963).
320. P.Ya.Glasunov and V.G.Guglya, Dokl.Akad.Nauk SSSR, **159**, 632 (1964) (in Russian).
321. L.M.Boyarshinov, Atomnaya Energiya, **21**, 42 (1966) (in Russian).
322. T.Tabata, Phys.Rev., **162**, 336 (1967).
323. V.G.Guglya, P.Ya.Glasunov and V.V.Kosukhin, Zh.Tekh.Fiz. **38**, 897 (1968) [Sov.Phys. Tech.Phys. **13**, 675 (1968)].
324. P.Verdier and F.Arnal, Comp.Rend. **B 267**, 1443 (1968).
325. P.J.Ebert, A.P.Lauson and E.M.Lent, Phys.Rev., **183**, 422 (1969).
326. T.Tabata, R.Ito and S.Okabe, Nucl.Inst.Meth., **94**, 509 (1971).
327. H.Frank, Z.Naturforsch., **14a**, 247 (1959).
328. L.Reimer and H.Drescher, J.Phys., **D 10**, 805 (1977).
329. L.Kuechler and H.-J.Hunger, Exp.Tech.Phys., **30**, 335 (1982).
330. T.E.Everhart, J.Appl.Phys., **31**, 1438 (1960).
331. R.F.Dashen, Phys.Rev., **134A**, 1025 (1964).
332. N.P.Kalashnikov and V.A.Mashinin, Zh.Eksp.Teor.Fiz., **59**, 2025 (1970) [Sov.Phys. JETP **32**, 1098 (1971)].
333. N.P.Kalashnikov and V.A.Mashinin, Zh.Tekh.Fiz., **43**, 2229 (1973) [Sov.Phys.Tech.Phys., **18**, 1412 (1974)].
334. G.D.Archard, J.Appl.Phys., **32**, 1505 (1961).
335. S.G.Tomplin, Proc.Phys.Soc., **82**, 465 (1963).
336. I.S.Tilinin, Zh.Eksp.teor.Fiz., **82**, 1291 (1982) [Sov.Phys.JETP, **55**, 751 (1982)].
337. I.S.Tilinin, Poverkhnost, (No 10), 19 (1989) (in Russian).
338. F.Rohrlich and B.C.Calson, Phys.Rev., **93**, 38 (1954).
339. M.I.Ryazanov, V.S.Remizovich and N.P.Kalashnikov, *Stolknoveniya bystrykh zaryazhennykh chastits v tverdych telakh (Collisions of Fast Charged Particles in Solids)*, Atomizdat, Moscow (1980).
340. J.C.Ashley, C.J.Tung and R.H.Ritchie and V.E.Anderson, IEEE Trans. NS **23**, 1833 (1976).
341. I.S.Tilinin, Poverkhnost, (No 2), 31 (1984) (in Russian).
342. I.S.Tilinin, Phys.Chem.Mech.Surfaces, **2**, 640 (1984), 2, 999 (1984).
343. V.S.Remizovich, M.I.Ryazanov and I.S.Tilinin, Zh.Eksp.Teor.Fiz., **79**, 448 (1980) [Sov.Phys. JETP **52**, 225 (1980)].
344. I.S.Tilinin and V.V.Frolov, Poverkhnost, (No 1), 5 (1986) (in Russian).
345. I.S.Tilinin and G.Betz, Nucl.Inst.Meth., (1996) in press.
346. V.S.Remizovich, M.I.Ryazanov and I.S.Tilinin, Dokl.Akad.Nauk SSSR **254**, 616 (1980) [Sov. Phys.Dokl. **25**, 751 (1980)].
347. H.Drescher, L.Reimer and H.Siedel, Z.angew.Phys., **29**, 331 (1970).
348. I.S.Tilinin, A.Jablonski and B.Lesiak-Orlowska, Appl.Surf.Sci., (1996), in press.
349. W.H.Bragg and R.Kleeman, Phil.Mag. **10**, 318 (1905).
350. R.Golser and D. Semrad, Phys.Rev., **A 45**, R4222 (1992).
351. J.Sadlick and A.O.Allen, J.Chem.Phys., **22**, 438 (1954).
352. A.Jablonski, Surf.Sci., **74**, 621 (1978).
353. S.Ishimura and R.Shimizu, Surf.Sci., **112**, 386 (1981).
354. V.B.Luk'yanov and E.F.Simonov, *Izmereniye i Identifikatsiya Radio- aktivnykh Isotopov (Measurement and Identification of Radioactive Isotops)*, Energoatomizdat, Moscow (1982).
355. J.E.Holliday and E.J.Sternglass, J.Appl.Phys., **28**, 1189 (1957).
356. G.Love, M.G.C.Cox, and V.D.Scott, J.Phys., **D 11**, 23 (1978).

357. R.Shimizu, Jpn.J.Appl.Phys., **22**, 1631 (1983).
358. W.Reuter, in Proc. 6-th Intern.Conf. X-Ray Optics and Microanalysis, G.Shinoda, K.Kohra and T.Ichinokawa, (Eds.), University of Tokyo Press, Tokyo (1972) p.121.
359. R.Shimizu and S.Ishimura, *Quantitative Analysis by Auger Electron Spectroscopy*, Technical Reports Toyota Foundation No. 1-006, 76-0175, Toyota Foundation, Tokyo (1981).
360. H.E.Bishop and J.P.Riviere, J.Appl.Phys., **40**, 1740 (1969).
361. I.S.Tilinin, Poverkhnost, (No 2), 5 (1992) (in Russian).
362. C.A.Quarles, Phys.Rev., **A 13**, 1278 (1976).
363. M.R.H.Rudge, Rev.Mod.Phys., **40**, 564 (1968).
364. I.S.Tilinin, Poverkhnost, (No 7), 10 (1991) (in Russian).
365. D.M.Smith and T.E.Gallon, J.Phys., **D 7**, 151 (1974).
366. L.Meda and G.Queirollo, Surf.Sci., **147**, 576 (1984).
367. J.Palczynski, W.Dolinski and S.Mroz, Surf.Sci., **247**, 395 (1991).
368. D.A.Shirley, Phys.Rev., **B 5**, 4709 (1972).
369. E.N.Sickafus, Phys.Rev., **B 16**, 1436 (1977).
370. C.N.Berglund and W.E.Spicer, Phys.Rev., **136**, A1030 (1964).
371. H.H.Madden and J.E.Houston, J.Appl.Phys., **47**, 307 (1976).
372. S.Tougaard and P.Sigmund, Phys.Rev., **B 25**, 4452 (1982).
373. S.Tougaard, Surf.Sci., **216**, 343 (1989).
374. T.Ogama and T.Horikawa, J.Vac.Sci.Technol., **A 8**, 2204 (1990).
375. H.Bender, Surf.Interface Anal., **15**, 767 (1990).
376. M.Repoux, Surf.Interface Anal., **18**, 567 (1992).
377. C.Binns, H.S.Derbyshire, S.C.Bayliss and C.Norris, Phys.Rev., **B 45**, 460 (1992).
378. M.Sastry, D.V.Paranjape and P.Ganguly, J. Electron Spectrosc.Relat.Phenom., **59**, 243 (1992).
379. S.Tougaard and C.Jansson, Surf.Interface Anal., **20**, 1013 (1993).
380. C.Jansson, H.S.Hansen, F.Yubero and S.Tougaard, J. Electron Spectrosc.Relat.Phenom., **60**, 301 (1992).
381. W.S.M.Werner, Phys.Rev., **52**, 2964 (1995).
382. M.Jo, Surf.Sci., **320**, 191 (1994).
383. M.Fukushima, Math.Programming, **35**, 253 (1986).
384. R.Fletcher, *Practical Methods of Optimization, Volume 2, Constraint Optimization*, Wiley, Chichester (1981).
385. Common Data Processing System ver.2.4, c/o K.Yoshihara, National Research Institute for Metals, 1-2-1, Sengen, Tsukuba-shi 305, Japan
386. S.Tougaard, J.Electron Spectrosc.Relat.Phenom., **52**, 243 (1990).
387. A.Jablonski and C.J.Powell, Surf.Interface Anal., **20**, 771 (1993).
388. O.K.T.Wu and E.M.Butler, J.Vac.Sci.Technol., **30**(3), 453 (1982).
389. O.K.T.Wu, G.G.Peterson, W.J.Larocca and E.M.Butler, Appl.Surf.Sci., **11/12**, 118 (1982).
390. L.S.Bernadez, J.Ferron, E.C.Goldberg and R.H.Buitraga, Surf.Sci., **139**, 541 (1984).
391. Y.L.Yan, M.A.Helfand and C.R.Clayton, Appl.Surf.Sci., **37**, 395 (1989).
392. M.F.Ebel, G.Moser, H.Ebel, A.Jablonski and H.Oppolzer, J. Electron Spectrosc.Relat.Phenom., **42**, 61 (1987).
393. P.L.J.Gunter, A.M. de Jong, J.W.Niemantsverdriet and H.J.H.Reither, Surf.Interface Anal., **19**, 161 (1992).
394. G.Olive, Surf.Sci., **197**, 83 (1993).
395. P.L.J.Gunter and J.W.Niemantsverdriet, Appl.Surf.Sci., **89**, 69 (1995).
396. W.S.M.Werner, Surf.Interface Anal., **23**, 696 (1995).

397. C.D.Wagner, L.E.Davis, M.V.Zeller, J.A.Taylor, R.H.Raymond and L.H.Gale, Surf.Interface Anal., **3**, 211 (1981).
398. R.Payling, J.Electron Spectrosc.Relat.Phenom., **37**, 225 (1985).
399. R.Payling and J.Szajman, J.Electron Spectrosc.Relat.Phenom., **43**, 37 (1987).
400. L.E.Davis, N.C.MacDonald, P.W.Palmberg, G.E.Riach and R.E.Weber, *Handbook of Auger Electron Spectroscopy*, Perkin-Elmer, Eden Prairie, MN (1978).
401. G.Lorang, J.L.Xu and J.-P.Langeron, Surf.Interface Anal., **19**, 60 (1992)
402. P.H.Holloway, Surf.Sci., **66**, 479 (1977).
403. P.M.Hall and J.M.Morabito, Surf.Sci., **62**, 1 (1977).
404. F.Pons, J.Le Hericy and J.-P.Langeron, Surf.Sci., **69**, 147 (1977).
405. T.Sekine, K.Hirata and A.Mogami, Surf.Sci., **125**, 565 (1983).
406. R.Hultgren, R.L.Orr, P.D.Anderson and K.K.Kelly, *Selected Values of Thermodynamic Properties of Metals and Alloys*, Wiley & Sons, Inc., New York (1963).
407. P.Streubel and H.Berndt, Surf.Interface Anal., **6**, 48 (1984).
408. A.J.Zagorenko and V.J.Zaporozhchenko, Surf. Interface Anal., **14**, 438 (1989).
409. M.F.Ebel, Surf.Interface Anal., **1**, 165 (1979).
410. W.Hanke, H.Ebel, M.F.Ebel, A.Jablonski and K.Hirokawa, J. Electron Spectrosc.Relat. Phenom., **40**, 241 (1986).
411. A.Jablonski, S.H.Overbury and G.A.Somorjai, Surf.Sci., **65**, 578 (1977).
412. M.Yoshitake and other members of the VAMAS-SCA working group in Japan, Surf.Interface Anal., **17**, 711 (1991).
413. A.Jablonski, B.Lesiak, L.Zommer, M.F.Ebel, H.Ebel, Y.Fukuda, Y.Suzuki and S.Tougaard, Surf.Interface Anal., **21**, 724 (1994).
414. K.Yoshihara, R.Shimizu, T.Homma, H.Tokutaka, K.Goto, F.Fujita, A.Kurokawa, S.Ichimura, M.Kurahashi, M.Kudo, Y.Hashiguchi, T.Suzuki, T.Ohmura, F.Soeda, K.Tanaka, A.Tanaka, T.Sekine, Y.Shiokawa and T.Hayashi, Surf.Interface Anal., **16**, 140 (1990).
415. Q.Zhe and Tian-Sheng, Surf. Sci., **194**, L127 (1988).
416. A.Jablonski, N.Sanada, Y.Suzuki, Y.Fukuda and M.Nagoshi, J.Electron Spectrosc.Relat. Phenom., **63**, 131 (1993).
417. J.W.Sobczak, B.Lesiak, A.Jablonski, A.Kosinski and W.Palczewska, Polish J.Chem., **69**, 1732 (1995).
418. B.Lesiak, J.Zemek, P. de Haan and A.Jozwik, Surf.Sci., **346**, 79 (1996).
419. G.Carter and M.J.Nobes, Surf.Interface Anal., **19**, 39 (1992).
420. A.Zalar, P.Panjan and V.Krasevec and S.Hofmann, Surf.Interface Anal. **19**, 50 (1992).
421. A.Zalar, Surf.Interface Anal., **9**, 41 (1986).
422. D.F.Mitchell and G.I.Sproule, Surf.Sci., **177**, 238 (1986).
423. D.Marton and J.Fine, Thin Solid Films, **151**, 433 (1987).
424. J.W.Coburn, J.Vac.Sci.Technol., **13**, 1037 (1976).
425. S.Hofmann, Surf.Interface Anal., **2**, (1980).
426. M.P.Seah and C.P.Hunt, Surf.Interface Anal., **5**, (1983).
427. A.Zalar, Thin Solid Films, **124**, 223 (1985).
428. S.Hofmann, Surf.Interface Anal., **9**, 3 (1986).
429. K.Wittmaak, Surf.Interafce Analysis, **21**, 323 (1994).
430. M.Henneberg, D.J.Pocker and M.A.Parker, Surf. Interface Anal., **19**, 55 (1992).
431. K.Kajiwara and H.Kawai, Surf.Interface Anal., **15**, 433 (1990).
432. S.Hofmann, J.Vac.Sci.Technol., **B 10**, 316 (1992).
433. M.Menyhard, A.Barna, J.P.Biersack, K.Jarrendahl and J.-E.Sundgren, J.Vac. Sci.Technol., **A 13**, 1999 (1995).
434. K.Kajiwara and R.Shimizu, J.Vac.Sci.Technol., **A 13**, 1316 (1995).

435. A.Barna, A.Sulyok and M.Menyhard, Surf.Interface Anal., **19**, 77 (1992).
436. M.Menyhard, A.Barna and H.J.Biersack, J.Vac.Sci.Technol., **A 12**, 2368 (1994).
437. M.Menyhard, A.Barna, A.Sulyok, K.Jarrendahl, J.-E.Sundgren and J.H.Biersack, Nucl. Instrum.Methods **B 85**, 383 (1994).
438. S.Hofmann, J.Erlewein and A.Zalar, Thin Solid Films, **43**, 275 (1985).
439. J.Fine, B.Navinsek, F.Davarya and T.D.Andreadis, J.Vac. Sci.Technol., **20**, 449 (1982).
440. J.M.Sanz and S.Hofmann, Surf.Interface Anal., **5**, 210 (1983).
441. A.Zalar, S.Hofmann and A.Zabkar, Thin Solid Films **131**, 149 (1985).
442. J.M.Hill, D.G.Royce, C.S.Fadley, L.F.Wagner and F.J.Grunthaner, Chem.Phys.Lett., **44**, 225 (1976).
443. H.Iwasaki, R.Nishitani and S.Nakamura, Jpn.J.Appl.Phys., **17**, 1519 (1978).
444. M.Pijolat and G.Hollinger, Surf.Sci., **105**, 114 (1981).
445. R.W.Paynter, Surf.Interface Anal., **3**, 186 (1981).
446. T.D.Bussing and P.H.Holloway, J.Vac.Sci.Technol., **A3**, 1973 (1985).
447. L.B.Hazell, I.S.Brown and Freisinger, Surf.Interface Anal., **8**, 25 (1986).
448. R.S.Yih and B.D.Ratner, J.Electr.Spectrosc.Relat.Phenom., **43**, 61 (1987).
449. V.I.Nefedov and O.A.Baschenko, J.Electron Spectrosc.Relat.Phenom., **47**, 1 (1988).
450. B.J.Tyler, D.G.Castner and B.D.Ratner, Surf.Interface Anal., **14**, 443 (1989).
451. Yu.G.Abashkin, S.E.Borodyansky, L.A.Vasil'ev and A.P.Dement'ev, Poverkhnost, (No 8), 71 (1989) (in Russian).
452. B.J.Flinn and N.S.McIntyre, Surf.Interface Anal., **15**, 19 (1990).
453. S.Ahkter, K.C.Cannon and J.M.White, Appl.Surf.Sci., **44**, 37 (1990).
454. M.Seelmann-Eggebert and H.J.Richter, J.Electron Spectrosc.Relat.Phenom., **52**, 273 (1990).
455. W.A.M.Aarnik, A.Weishaupt and A.van Silfhout, Appl. Surf. Sci., **45**, 37 (1991).
456. G.Yu.Cherkashinin and V.V.Pasternak, Poverkhnost, (No 8), 157 (1991) (in Russian).
457. S.E.Borodyansky and Yu.G.Abashkin, Surf.Sci., **251/252**, 325 (1991).
458. O.A.Baschenko, Poverkhnost, (No 2), 93 (1992) (in Russian).
459. G.C.Smith and A.K.Livesey, Surf.Interface Anal. **19**, 175 (1992).
460. P.H.Holloway and T.D.Bussing, Surf.Interface Anal., **18**, 251 (1992).
461. G.N.Derry abd W.E.Vanderlinde, J.Vac.Sci.Technol., **A10**, 2826 (1993).
462. M.G.Grabherr, H.Ebel, M.F.Ebel, R.Svagera and G.Baron, J.Electron Spectrosc.Relat. Phenom., **63**, 43 (1993).
463. W.S.M.Werner, G.C.Smith and A.K.Livesey, Surf.Interface Anal., **21**, 38 (1993).
464. J.Zemek, O.A.Baschenko, M.A.Tyzykhov, Thin Solid Films, **224**, 141 (1993).
465. J.Zemek, O.A.Baschenko, M.A.Tyzykhov and P.Jiricek, Surf.Sci., **318**, 421 (1994).
466. W.S.M.Werner, I.S.Tilinin, H.Beilschmidt and M.Hayek, Surf.Interface Anal., **21**, 537 (1994).
467. G.Yu.Cherkashinin, J.Electron Spectrosc.Relat.Phenom., **74**, 67 (1995).
468. M.Seelmann-Eggerberg and R.C.Keller, Surf.Interface Anal., **23**, 589 (1995).
469. P.J.Cumpson, Surf.Interface Anal. **73**, 25 (1995).
470. P.M.Morse and H.Feshbach, *Methods of Mathematical Physics*, McGraw-Hill, New York, 1953.
471. A.N.Tikhonov, Sov.Math. **4**, 1035 (1963).
472. A.N.Tikhonov and V.Y.Arsenin, *Solutions of Ill-Posed Problems*, V.H.Winston, Washington, DC (1977).
473. J.P.Butler, J.A.Reeds and S.V.Dawson, SIAM J.Numer.Anal., **18**, 381 (1981).
474. M.Bertero, Adv.Electronics Electron Phys., **75**, 2 (1989).
475. S.F.Gull and J.G.Daniel, Nature, **272**, 686 (1978).
476. P.J.Hore, in *Maximum Entropy in Action*, B.Buck and V.A.Macaulay, (Eds.), OUP, Oxford (1991).

477. P.F.Fougere, (Ed.), *Maximum Entropy and Bayesian Methods*, Kluwer Academic, Dordrecht (1988).
478. A.I.Boronin, V.I.Bukhtiyarov, R.Kvon, V.V.Chesnokov and R.A.Buyanov, Surf.Sci., **258**, 289 (1991).
479. C.M.Comrie and W.H.Weinberg, J.Chem.Phys., **64**, 250 (1976).
480. M.Seelmann-Eggelbert and R.C.Keller, Surf.Interface Anal., **25**, 589 (1995).
481. G.Margaritondo, Acta Phys.Polon. **A 86**, 705 (1994).
482. W.M.Kwiatek, Acta Phys.Polon., **A 86**, 695 (1994).
483. F.J.Himpsel, Acta Phys.Polon., A 86, 771 (1994).
484. H.Ade, C.H.Ko, E.D.Johnson and E.Anderson, Surf.Interface Anal., **19**, 17 (1992).
485. H.Ade, E.Anderson and C.H.Ko, Appl.Phys.Lett., **60**, 1040 (1992).
486. C.Capasso, W.Ng, A.K.Ray-Chaudhuri, S.H.Liang, R.K.Cole, Z.Y.Guo, J.Wallace, F.Cerrina, J.Underwood, R.Perera, J.Kortright. G. De Stasio and G.Margaritondo, Surf.Sci., **287/288**, 1046 (1993).
487. B.M.Batterman, Phys.Rev., **133**, A759 (1964).
488. J.Zegenhagen, Surf.Sci.Repts., **18**, 199 (1993).
489. D.P.Woodruff, D.L.Seymour, C.F.McConville, C.E.Riley, M.D.Crapper, N.P.Prince and R.G.Jones, Surf.Sci., **195**, 237 (1988).
490. M.J.Bedzyk, D.H.Bilderback, G.M.Bommarito, M.Caffrey and J.S.Schildkraut, Science, **241**, 1788 (1988).
491. H.D.Aruna, G.M.Bommarito and D.Acevedo, Science, **250**, 69 (1990).
492. B.W.Batterman and H.Cole, Rev.Mod.Phys., **36**, 681 (1964).
493. A.Authier, Acta Cryst. **A 42**, 414 (1986).
494. Z.G.Pinsker, *Dynamical Scattering of X-Rays in Crystals*, Springer, Berlin, 1978.
495. X.Shi, C.Su, D.Heskett, L.Berman, C.-C.Kao and M.J.Bedzyk, Phys.Rev., **49**, 14638 (1994).
496. D.Heskett, P.Xu, L.Berman, C.-C.Kao and M.J.Bedzyk, Surf.Sci., **344**, 267 (1995).
497. D.L.Adler, I.R.Collins, X.LIang, S.J.Murray, G.S.Leatherman, K.D.Tsuei, E.E.Chaban, S.Chandravarkar, R.McGrath, R.D.Diehl and P.H.Citrin, Phys. Rev., **B 48**, 17445 (1993).
498. C.Stampfl, M.Scheffler, H.Over, J.Buchhardt, M.Nielsen, D.L.Adams and W.Moritz, Phys.Rev., **B 49**, 4959 (1994).
499. R.Fasel, P.Aebi, J.Osterwalder and L.Schlapbach, Surf.Sci., **331/333**, 80 (1995).
500. P.A.Bennett, J.C.Fuggle, F.U.Hillebrecht, A.Lenselink and G.A.Sawatzky, Phys.Rev., **B 27**, 2914 (1983).
501. M.Vos, D.van der Marel and G.A.Sawatzky, Phys.Rev., **B 29**, 3073 (1984).
502. S.M.Thurgate, C.P.Lund and A.B.Wedding, Phys.Rev., **B 50**, 4810 (1994).
503. J.L.Robins, Prog.Surf.Sci., **48**, 167 (1994).
504. H.W.Haak, G.A.Sawatzky and T.D.Thomas, Phys. Rev.Lett., **41**, 1825 (1978).
505. H.W.Haak, G.A.Sawatzky, L.Ungier, J.K.Gimzewski and T.D.Thomas, Rev.Sci. Instrum., **55**, 696 (1984).
506. G.A.Sawatzky, Treatise Mat.Sci.Technol. **30**, 167 (1988).
507. S.M.Thurgate, Aust.J.Phys., **43**, 443 (1990).
508. S.M.Thurgate, B.D.Todd, B.Lohmann and A.Stelbovics, Rev.Sci.Instrum., **61**, 3733 (1990).
509. S.M.Thurgate, in *The Structure of Surfaces 111*, S.Y.Tong, M.A.Van Hove, K.Takayami and X.D.Xie, (Eds.), Springer-Verlag, Berlin (1991) p.179.
510. S.M.Thurgate, C.P.Lund and A.B.Wedding, Nucl.Instrum.Methods, **B 87**, 259 (1994).
511. E.Jensen, R.A.Bartynski, S.L.Hulbert, E.D.Johnston and R.F.Garrett, Phys. Rev.Lett., **62**, 71 (1989).
512. E.Jensen, R.A.Bartynski, M.Weinert, S.L.Hulbert, E.D.Johnson and R.F.Garrett, Phys.Rev., **B 41**, 12468 (1990).

513. S.L.Hulbert, C.C.Kao, R.F.Garrett, R.A.Bartynski, S.Yang and M.Weinert, J.Vac.Sci. Technol., **A 9**, 1919 (1991).
514. R.A.Bartynski, E.Jensen, K.Garrison, S.L.Hulbert and M.Weinert, J.Vac. Sci.Technol., **A 9**, 1907 (1991).
515. E.Jensen, R.A.Bartynski, R.F.Garrett, S.L.Hulbert, E.D.Johnson and C.C.Kao, Phys.Rev., **B 45**, 13636 (1992).
516. C.P.Lund and S.M.Thurgate, Phys.Rev., **B 23**, 17166 (1994).
517. J.Kirschner, in *Electron Spectroscopy for Surface Analysis*, H.Ibach, (Ed.), Springer, Berlin, (1977) p.57.
518. J.van Laar, A.Huijser and T.L. van Rooy, J.Vac.Sci.Technol., **14**, 894 (1977).
519. R.Ludeke and A.Koma, J.Vac.Sci.Technol., **13**, 241 (1976).
520. N.J.Shevchik, J.Tejeda and M.Cardona, Phys.Rev., **B 9**, 2627 (1974).
521. E.Antonides, E.C.Janse and G.A.Sawatzky, Phys.Rev., **B 15**, 4596 (1977).
522. A.T.Stelbovics, B.D.Todd, S.M.Thurgate and B.Lohmann, Surf.Sci., **278**, 193 (1992).